

Photoionized Herbig-Haro objects in the Orion Nebula through deep high-spectral resolution spectroscopy I: HH 529 II and III

J. E. Méndez-Delgado^{1,2} [★], C. Esteban^{1,2}, J. García-Rojas^{1,2}, W. J. Henney³
A. Mesa-Delgado⁴ and K. Z. Arellano-Córdova¹

¹ Instituto de Astrofísica de Canarias (IAC), E-38205 La Laguna, Spain

² Departamento de Astrofísica, Universidad de La Laguna, E-38206 La Laguna, Spain

³ Instituto de Radioastronomía y Astrofísica, Universidad Nacional Autónoma de México, Apartado Postal 3-72, 58090 Morelia, Michoacán, México

⁴ Calle Camino Real 64, Icod el Alto, Los Realejos, 38414, Tenerife, Spain

Accepted XXX. Received YYY; in original form ZZZ

ABSTRACT

We present the analysis of physical conditions, chemical composition and kinematic properties of two bow shocks—HH 529 II and HH 529 III—of the fully photoionized Herbig-Haro object HH 529 in the Orion Nebula. The data were obtained with the Ultraviolet and Visual Echelle Spectrograph at the 8.2m Very Large Telescope and 20 years of *Hubble Space Telescope* imaging. We separate the emission of the high-velocity components of HH 529 II and III from the nebular one, determining n_e and T_e in all components through multiple diagnostics, including some based on recombination lines (RLs). We derive ionic abundances of several ions, based on collisionally excited lines (CELs) and RLs. We find a good agreement between the predictions of the temperature fluctuation paradigm (t^2) and the abundance discrepancy factor (ADF) in the main emission of the Orion Nebula. However, t^2 can not account for the higher ADF found in HH 529 II and III. We estimate a 6% of Fe in the gas-phase of the Orion Nebula, while this value increases to 14% in HH 529 II and between 10% and 25% in HH 529 III. We find that such increase is probably due to the destruction of dust grains in the bow shocks. We find an overabundance of C, O, Ne, S, Cl and Ar of about 0.1 dex in HH 529 II-III that might be related to the inclusion of H-deficient material from the source of the HH 529 flow. We determine the proper motions of HH 529 finding multiple discrete features. We estimate a flow angle with respect to the sky plane of $58 \pm 4^\circ$ for HH 529.

Key words: ISM:Abundances – ISM: Herbig–Haro objects – ISM: individual: Orion Nebula – ISM: individual: HH 529 III.

1 INTRODUCTION

Herbig-Haro (HH) objects are small emission nebulae associated with outflows from young stars interacting with the surrounding environment (Schwartz 1983). Since their discovery by George Herbig and Guillermo Haro (Herbig 1950, 1951, 1952; Haro 1952, 1953) a multitude of them have been discovered and studied. Through the *Hubble Space Telescope* (*HST*), multiple velocity features associated with HH objects have been observed in the Orion Nebula with unprecedented detail. There are several works dedicated to determine the nature and physical properties of many outflows from stars in the Orion Nebula (see Bally et al. 2000; Bally & Reipurth 2001; O’Dell & Henney 2008; O’Dell et al. 2015, and references therein). These have revealed that the Orion Nebula is a complex environment with multiple gas interactions. These high velocity systems

cover a wide range of velocities with noticeable differences in the conditions of their emitting gas.

Through the radiation field of the massive stars of the Orion Nebula, HH objects can be photoionized under conditions where the shock between the ambient gas and the HH merely serves to create a dense blob where we can determine the physical conditions and chemical abundances using the standard methods developed to study ionized nebulae (Reipurth & Bally 2001). Moderate velocity ($v < 100 \text{ km s}^{-1}$) shocks in H II regions are predicted to be strongly radiative, showing only a thin high- T_e cooling zone immediately behind the shock, which contributes little to the total emission (Henney 2002). The bulk of the shocked gas returns to thermal equilibrium at the same T_e as the ambient gas, so the combined front (shock plus cooling zone) can be considered isothermal. However, there are few works in the literature dedicated to analyse the chemical composition of photoionized HH objects, isolating their emission from that of the nebula in which they are

[★] E-mail: jemd@iac.es

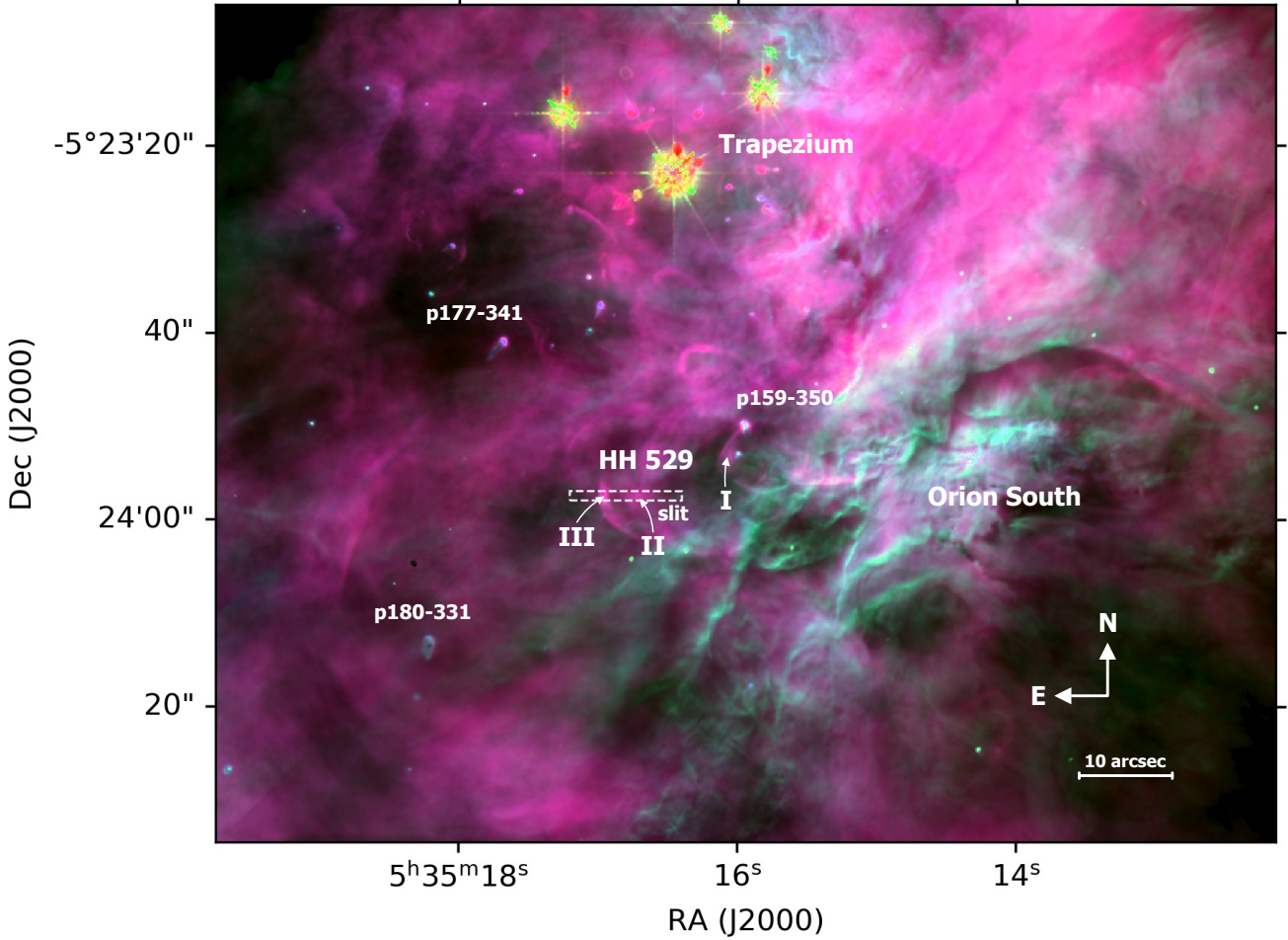


Figure 1. Composite WFPC2 *HST* image of the central Orion Nebula. Three narrow filters were used for the color scale: F502N, F658N and F656N for red, green and blue, respectively (images obtained by [Bally et al. 1998](#)). The slit position of our observations is indicated. It covers the bow shocks HH 529 III and HH 529 II of the Herbig-Haro object HH 529. The position of some protoplanetary discs (proplyds) are also indicated.

immersed. Using high-spectral resolution spectroscopy, [Blagrave et al. \(2006\)](#) and [Mesa-Delgado et al. \(2009\)](#) were able to separate the emission of HH 529 III+II and HH 202 S, respectively, from the main emission of the Orion Nebula. This permitted the analysis of the chemical composition of the ionized gas under the peculiar physical conditions of the HHs and the effects of their interaction with the surrounding nebular gas, such as the chemical effects of dust destruction.

As [Mesa-Delgado et al. \(2008\)](#) showed through long slit spectra, there are important spatial variations in the physical conditions of the Orion Nebula due to the presence of HH objects. These variations also affect some chemical properties of the gas. For example, these authors found an increase in the discrepancy between the abundances obtained from recombination lines (RLs) and collisionally excited lines (CEls) for the same heavy element at the locations of HH objects. Therefore, it is important to investigate the physical and chemical influence that HH objects exert on the gas of ionized nebula and test our knowledge of photoionized regions by analysing objects with complex conditions.

This work aims to be the first in a series devoted to the analysis of photoionized HHs in the Orion Nebula using very high resolution spectroscopy from the Ultraviolet and Visual Echelle Spectrograph (UVES) ([D'Odorico et al. 2000](#)) attached to the UT2 (Kueyen) of the Very Large Telescope (VLT). This paper is dedicated to two bow shocks associated with HH 529: HH 529 II and HH 529 III. HH 529 consists of a series of shocks flowing toward the east in the central region of the Orion Nebula. It is divided into three main shocks designated as HH 529 I, HH 529 II and HH 529 III, numbered from west to east ([O'Dell & Henney 2008](#)). We spatially separate the emission from HH 529 II and HH 529 III and isolate the blueshifted high-velocity emission of the gas of the shock from the nebular one. We analyse our high-spectral resolution observations that cover a wide spectral range (3100–10400 Å) through 4 spatial cuts, obtaining 7 1D spectra: 4 corresponding to the main emission of the Orion Nebula, one for HH 529 II, another one for HH 529 III and one additional 1D spectrum corresponding to the sum of all the 1D spectra. This last spectrum simulates a single low-spectral resolution longslit observation, including the mixing

of the HH emission with that of the nebular gas, summing up the emission of all the velocity components for each emission line. In this paper we analyse the physical conditions, chemical composition and kinematic properties of HH 529 II and HH 529 III as well as the Orion Nebula in several small and nearby areas.

The paper is organized as follows: in Section 2 we describe the observations and the reduction process for the spectroscopic data, as well as the *HST* imaging used to calculate the proper motions of HH 529 in the plane of the sky. In Section 3 we describe the emission line measurements, identifications and the reddening correction as well as a comparison between our observations and those from Blagrave et al. (2006) over the common spectral range (3500–7500 Å). In Section 4 we describe the excitation mechanism in the high-velocity components. In Section 5 we derive the physical conditions of the gas throughout different methods, using CELs, RLs and continuum emission. In Section 6 we derive ionic abundances using both RLs and CELs. In Section 7 we describe the temperature fluctuations paradigm and estimate values of t^2 , based on the different temperature diagnostics. In Section 8 we discuss the abundance discrepancy (AD) between ionic abundances derived with CELs and RLs. In Section 9 we analyse the total abundances obtained from RLs and CELs, in the second case both with and without the assumption of the existence of temperature fluctuations ($t^2 > 0$ and $t^2 = 0$, respectively). We also discuss the increase in the gaseous Fe abundance due to dust destruction in HH 529 II and HH 529 III. In Section 10 we describe the radial velocity structure of each component, both the nebular and the high-velocity ones. We also derive the electron temperature from the thermal broadening of the line profiles. In Sections 11 and 12 we calculate the proper motions of HH 529 and discuss some physical properties of the shock, such as the pre-shock density. Finally, in Section 13 we summarize our main conclusions. In the appendix, some extra information, tables and figures are attached as supporting material.

2 OBSERVATIONS AND DATA REDUCTION

The observations were made under photometric conditions during the night of November 28 and 29, 2013 using UVES in the UT2 of the Very large Telescope (VLT) in Cerro Paranal, Chile. The slit position was centred at the coordinates RA(J2000)= $05^{\text{h}}35^{\text{m}}16\text{s}.80$, DEC(J2000)= $-05^{\circ}23'57.48''$, with a slit length of 10 arcsec in the blue arm and 12 arcsec in the red arm in order to give an adequate interorder separation. Table 1 shows the main parameters of UVES observations. The slit width was set to 1 arcsec, which provides an effective spectral resolution $\lambda/\Delta\lambda \approx 40000$ (6.5 km s^{-1}). To perform the flux calibration of the data, three exposures of 150s of the standard star GD71 (Moehler et al. 2014a,b) were taken under similar conditions of seeing and airmass than the science observations during the same night. The spatial coverage of the slit is shown in Fig. 1.

Our observations cover the spectral range between 3100–10420 Å, using two standard dichroic settings of UVES. Dichroic #1 setting split the light in two wavelengths ranges: from 3100 to 3885 Å in the blue arm and from 4785 to 6805 Å in the red one, while the dichroic #2 setting covers from 3750 to 4995 Å in the blue arm and from 6700 to 10420 Å in the red one. However, in our high resolution and wide spectral range observations, there are some observational gaps. The red arm use two CCDs, and due to their physical separation, spectral ranges 5773–5833 Å and 8540–8650 Å could not be observed. Additionally there are some narrow gaps that could not be observed in the redmost part of the red arm

Table 1. Main parameters of UVES spectroscopic observations.

Date	$\Delta\lambda$ (Å)	Exp. time (s)	Seeing (arcsec)	Airmass
2013-11-29	3100-3885	5, 3×180	0.79	1.20
2013-11-29	3750-4995	5, 3×600	0.65	1.14
2013-11-29	4785-6805	5, 3×180	0.79	1.20
2013-11-29	6700-10420	5, 3×600	0.65	1.14

Table 2. *HST* observations used in proper motion study.

Date	Program	Camera, CCD, Filter	Reference
1995-03	5469	WFPC2, PC, F656N	Bally et al. (1998)
2005-04	10246	ACS, WFC, F658N	Robberto et al. (2013)
2015-01	13419	WFC3, UVIS, F656N	Bally & Reipurth (2018)

in the dichroic #2 setting because the spectral orders could not fit entirely within the CCD. These ranges are ~ 8911 –8913 Å, 9042–9046 Å, 9178–9182 Å, 9317–9323 Å, 9460–9469 Å, 9608–9619 Å, 9760–9774 Å, 9918–9935 Å, 10080–10100 Å and 10248–10271 Å.

We reduced the spectra using a combination of tasks from the public ESO UVES pipeline (Ballester et al. 2000) under the GASGANO graphic user interface, and tasks built by ourselves based on IRAF¹ (Tody 1993) and several python packages. Firstly, we used IRAF tasks FIXPIX and IMCOMBINE to mask known bad pixels in our images and to combine all the images with the same exposure time. Then, we used the ESO UVES pipeline for bias subtraction, background subtraction, aperture extraction, flat-fielding and wavelength calibration. As a product, we obtained a 2D science spectrum for each arm in each dichroic setting without flux calibration. We followed the same procedure for GD 71 but extracting both a 2D and a 1D spectrum. The 2D spectrum of the calibration star helps us to note the presence of faint sky lines which are also present in the science spectra.

One crucial step of the data reduction is to perform adequate cuts in the spatial direction of the slit to extract 1D spectra. We chose these spatial cuts in order to study in detail each observed velocity component and trying to maximise the shock/nebular emission ratio. We relied on the [Fe III] $\lambda 4658$ line, which is relatively bright in the high-velocity components, to delimit the cuts. In the bi-dimensional spectrum shown in Fig. 2 for some representative lines, we show that the seeing conditions permit us to spatially separate HH 529 II from HH 529 III. HH 529 II has a “ball shape” while HH 529 III presents an elongated distribution along the spectral axis. This is related to the morphology of the outflow system of HH 529 (firstly identified by Bally et al. 2000). This system shows three prominent bright arcs, identified by the numbers I, II and III, being numbered by their position from west to east (O’Dell & Henney 2008). However, the system is more complex than just three homogeneous arcs as we will analyse in Section 11. The length covered by each cut in the spatial direction is 1.23 arcsec, 4.43 arcsec, 2.46 arcsec and 1.23 arcsec for cuts 1, 2, 3 and 4, respectively. The numbering of the cuts has been defined from west to east. The high-velocity component of cut 3 corresponds to HH 529 III, while that of cut 2 is HH 529 II. We have also defined an additional 1D spectrum, labelled as “combined cuts”. This was created by adding the flux of the lines measured in all the components of all cuts. The lines included in this spectrum

¹ IRAF is distributed by National Optical Astronomy Observatory, which is operated by Association of Universities for Research in Astronomy, under cooperative agreement with the National Science Foundation

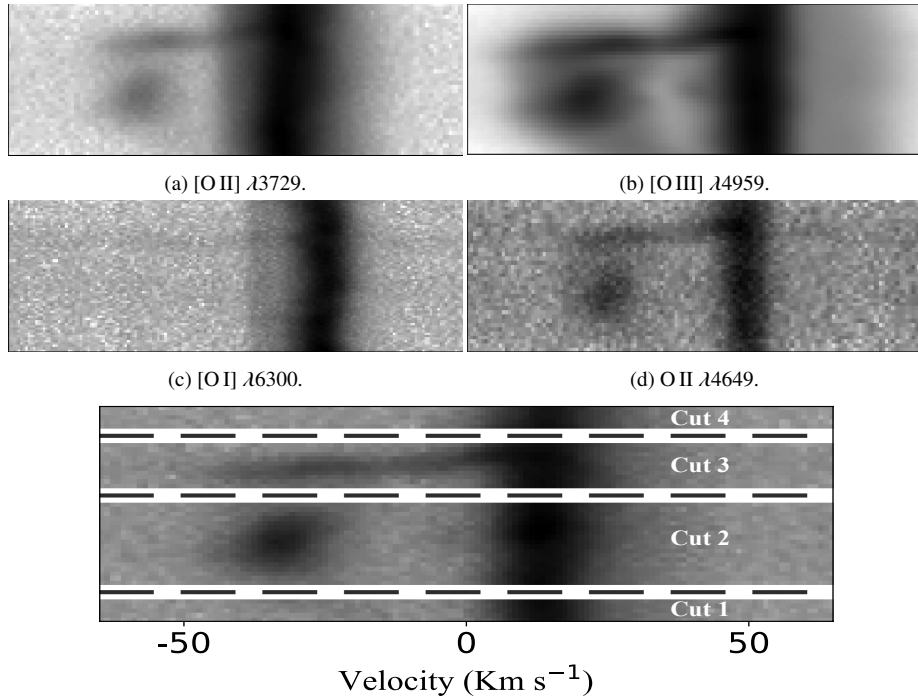
(e) $[\text{Fe III}] \lambda 4658$. The 4 cuts are identified. Bottom: Cut 1, Top: Cut 4.

Figure 2. *Upper panels:* Sample of representative lines in the bi-dimensional spectrum. The Y axis corresponds to the spatial direction (up east, down west, see Fig. 1 for the spatial location of the slit) while the X axis is the spectral axis. All figures are centered at λ_0 , the rest-frame reference wavelength of each line. The “ball-shaped” emission corresponds to HH 529 II while the elongated one to HH 529 III. The blueshifted high-velocity components do not present emission from neutral elements as $[\text{O I}]$ and rather faint emission from low ionization ions such as $[\text{O II}]$. *Bottom panel:* Emission of the $[\text{Fe III}] \lambda 4658.17$ line as well as the limits and extension of the different spatial cuts selected to analyse each velocity component. Cut 1 is at the bottom, which corresponds to the westernmost one. The spatial coverage is 1.23 arcsec, 4.43 arcsec, 2.46 arcsec and 1.23 arcsec for cuts 1, 2, 3 and 4, respectively. The velocity scale is heliocentric.

were those detected and identified in the nebular component of all cuts. The spectrum of the combined cuts is useful for analysing the effect that a non-resolved shock component would have in the properties of a low-resolution spectrum. We used the Python-based Astropy package (Astropy Collaboration et al. 2013; Price-Whelan et al. 2018) to obtain 1D spectra for each cut, doing the conversion between the different pixel scale of the CCDs in the blue and the red arm. Each spatial cut covers an area larger than the seeing size during the observations, as is shown in Table 1. We used the IRAF tasks STANDARD, SENSFUNC and CALIBRATE to perform the flux calibration of each 1D spectra of all cuts. The radial velocity correction was made using Astropy.

For the determination of the proper motion of HH 529, we take advantage of the 20 years of archival *HST* imaging that is now available. We employ three epochs of observations, as detailed in Table 2. All data were downloaded from the Barbara A. Mikulski Archive for Space Telescopes².

3 LINE INTENSITIES AND REDDENING

We used the SPLOT task from IRAF to measure line intensities and estimate their uncertainties. We applied a double Gaussian profile fit for the nebular and the high-velocity component, delimiting the continuum by eye. The error estimations are carried out by SPLOT by Monte-Carlo simulations around a gaussian sigma defined as the

average *rms* measured on the continuum on both sides of each line with 100 iterations. The error estimates are one sigma estimates. We also consider an error of the absolute flux calibration of 2%, added quadratically. In case of evident line blending, we applied as many Gaussians as necessary to properly reproduce the line profile. As was mentioned in Section 2, the observed wavelength range (3100–10420 Å) was covered in 4 sections (two dichroic settings splitting the light into two spectrograph arms). Between each section, there is an overlapping zone from where we used the most intense lines to normalize the entire spectrum with respect to $\text{H}\beta$. The measured flux of $\text{H I} \lambda 3835$, $[\text{O III}] \lambda 4959$ and $[\text{S II}] \lambda 6731$ lines were used to normalize the spectra from the blue arm of dichroic #1, the red arm of dichroic #1 and the red arm of dichroic #2 settings respectively ($\text{H}\beta$ is in the blue arm of dichroic #2 setting). This normalization eliminates the differences in flux between each part of the spectrum due to the different pixel scale between the blue and the red arms.

The emission lines were corrected for reddening using Eq. (1), where $f(\lambda)$ is the adopted extinction curve from Blagrave et al. (2007), normalized to $\text{H}\beta$. We calculate the reddening coefficient, $c(\text{H}\beta)$, by using the ratios of $\text{H}\epsilon$, $\text{H}\delta$, $\text{H}\gamma$ and $\text{H}\alpha$ Balmer lines and the P12, P11, P10, P9 Paschen lines with respect to $\text{H}\beta$ and the emissivity coefficients of Storey & Hummer (1995).

$$\frac{I(\lambda)}{I(\text{H}\beta)} = \frac{F(\lambda)}{F(\text{H}\beta)} \times 10^{c(\text{H}\beta)f(\lambda)}. \quad (1)$$

The final adopted $c(\text{H}\beta)$ value is the weighted average value obtained from the aforementioned Balmer and Paschen lines and is shown in Table 3 for each component. The selected HI lines are

² MAST, <https://archive.stsci.edu/>

Table 3. Reddening coefficients for each component.

	c(H β)	
	High-velocity	Nebula
Cut 1	-	0.82 ± 0.02
Cut 2	0.90 ± 0.03	0.83 ± 0.02
Cut 3	0.89 ± 0.05	0.84 ± 0.03
Cut 4	-	0.83 ± 0.02
Combined cuts	-	0.85 ± 0.02

free of line-blending or telluric absorptions that may affect the determination of $c(H\beta)$. Despite the existence of further isolated and bright Balmer and Paschen lines in the spectra, we did not use them since their emission depart from the case B values. This behaviour was reported previously in the Orion Nebula (Mesa-Delgado et al. 2009), the Magellanic Clouds (Domínguez-Guzmán et al. 2019) and in several planetary nebulae (PNe, see Rodríguez 2020).

Blagrade et al. (2006) (hereinafter BMB06) observed a zone of the Orion Nebula that includes HH 529 II+III using the 4m Blanco telescope at the Cerro Tololo Inter-American Observatory, covering the 3500–7500Å spectral region. Fig. 3 shows a comparison between their reddening corrected nebular spectrum and ours (from cut 2). For the comparison, we have excluded lines flagged with notes of “Avg”, “blend” or “small FWHM” in Table 1 of BMB06, due to their uncertain fluxes. For example, [Ne III] $\lambda 3967.46$ line, marked with an “Avg”, is inconsistent with the measured intensity of [Ne III] $\lambda 3868.75$, since their observed ratio is 2.02, quite far from the theoretical one of 3.29 (McLaughlin et al. 2011). A least squares linear fit of the data represented in Fig. 3 yields the relationship $y = 1.00 (\pm 0.01) x + 0.05 (\pm 0.02)$, indicating that the BMB06’s spectrum (y values) presents systematically larger (by a factor of ~ 1.12) line ratios (relative to H β) than ours (x values). This is very noticeable in the spectral region of the high-level Balmer lines (3660–3720Å), where this difference can reach up to 50%. This may be due to the relative weakness of these lines, coupled with the abrupt change in the continuum level due to the closeness to the Balmer discontinuity. In Table D1, we compare our values of some selected reddening-corrected Balmer line ratios with those obtained by BMB06. It is very surprising that the Balmer line ratios with respect to H β obtained by BMB06 for both components differ significantly from the theoretical values. However, this does not seem to be the case when we use ratios of Balmer lines excluding H β . An underestimation of around 10% in the flux of H β in the BMB06’s spectrum explains the systematic trend observed in Fig. 3. We do not compare the high-velocity component of BMB06 with our data of HH 529 II and HH 529 III because their slit position is slightly different than ours and their seeing of 2–2.5 arcsec did not permit them to adequately separate spatially HH 529 II from HH 529 III.

Fig. 4 shows the [O III] $\lambda 4958.91$ line profile in the different cuts. As can be seen, the reddest component of each profile (corresponding to the nebular component) shows practically the same shape in all cuts except in cut 3, where the line is broadened by the presence of a larger velocity dispersion in the high-velocity component. The complexity of the velocity components of HH 529 is discussed in more detail in Section 11.

Line identifications were consistently made by adopting the theoretical wavelengths of Peter Van Hoof’s latest Atomic Line List v2.05b21³ (Van Hoof 2018) for all ions except for Cl III, Cl IV and Ne III due to some inconsistencies found (see Section 10 for

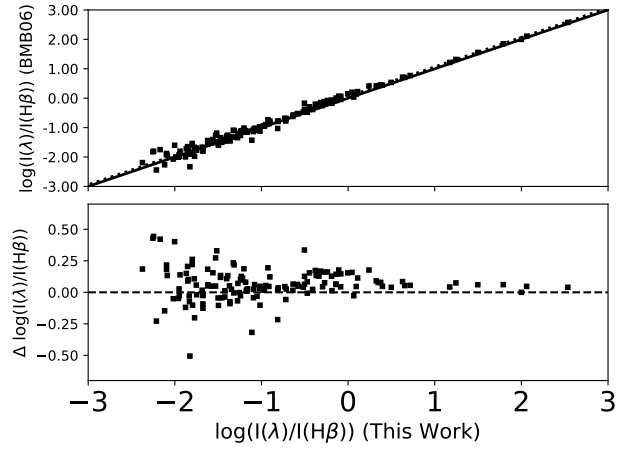


Figure 3. *Upper panel:* Comparison between the reddening corrected nebular spectrum ($\log(I(\lambda)/I(H\beta))$) from Blagrade et al. (2006) and this work. The dotted line represents the linear fit $y = 1.00x + 0.05$, while the solid line represents $y = x$. *Bottom panel:* Difference of the logarithm of line intensity ratios with respect to $I(H\beta)$ in the spectrum of BMB06 and ours.

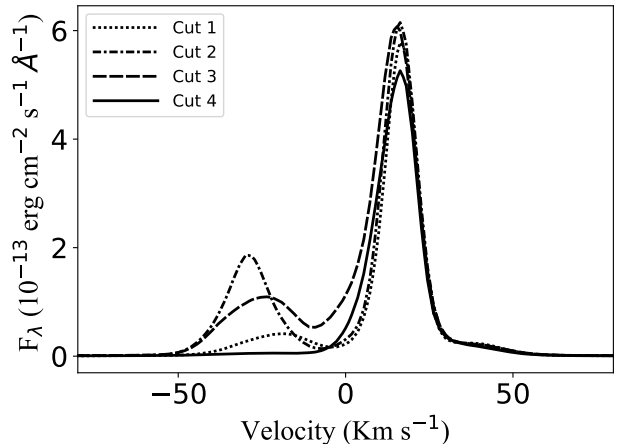


Figure 4. Profile of [O III] $\lambda 4958.91$ line in each of the analysed spatial cuts. The velocity scale is heliocentric.

a detailed discussion). The number of lines we have identified in our spectra is very large. Line identifications and observed and dereddened flux line ratios are presented in 4 online tables, one for each analysed cut. Tables of cut 2 and cut 3 contain, in addition to the observed nebular component, the spectra of HH 529 II and HH 529 III, respectively. These tables contain, for each measured line, the identified rest-frame wavelength (λ_0), the identified ion, the observed wavelength (λ), the radial velocity with respect to λ_0 (v_r), the full width at half maximum (FWHM), the observed flux relative to $F(H\beta)=100$ ($F(\lambda)/F(H\beta)$), the reddening corrected intensity relative to $I(H\beta)=100$ ($I(\lambda)/I(H\beta)$), the estimated error of the reddening corrected intensity and some notes. In the nebular components, 514, 633, 579 and 522 lines were measured in cuts 1, 2, 3 and 4, respectively. For HH 529 II and HH 529 III, 376 and 245 lines were detected, respectively. Multi-line blends were counted as single detections. As an example of our line tables, in Table D2 we show a sample of 15 lines of the spectra of cut 2.

³ <https://www.pa.uky.edu/~peter/newpage/>

4 EXCITATION MECHANISM IN HH 529 II AND HH 529 III

5 PHYSICAL CONDITIONS

5.1 Physical conditions based on CELs

We use PyNeb (version 1.1.10) (Luridiana et al. 2015) and the updated atomic dataset listed in Table D3 to calculate physical conditions based on the intensity ratios of CELs from different ions.

The first step was to test all the intensity ratios of CELs that can serve as a temperature or density diagnostic using the PyNeb task *getCrossTemDen*. This task uses two line ratios at the same time: one as density diagnostic and the other one for temperature, giving their convergence to a pair n_e, T_e as a result. We tried all possible permutations for all the available diagnostics in all components from all cuts. We only discarded the use of lines strongly affected by blends, telluric emissions and/or absorptions or reflections in the optical system of the spectrograph. We did not consider the n_e diagnostic based on [NI] $\lambda\lambda 5198/5200$ owing to a significant fluorescent contribution in the Orion Nebula (Ferland et al. 2012).

Diagnostics based on [Ni III] λ_1/λ_2 , where $\lambda_1, \lambda_2 \in [6000, 6534, 6682, 6797, 6946, 7890]$ do not give any useful physical information since they either did not converge or showed convergences at values highly discordant with the other diagnostics. This will be discussed in Section C. Another interesting diagnostics are based on [Fe III] λ_1/λ_2 , where $\lambda_1, \lambda_2 \in [4658, 4702, 4734, 4881, 5011, 4925, 4987, 5271]$. With the exception of [Fe III] 4658/4702, all the diagnostics converge in a fairly wide range of physical conditions. This is due to the ambivalence and/or high dependence of these ratios on both density and temperature. This will be discussed in Section 5.2.

After the initial exploration, we define the ratios we consider good indicators of electron density and temperature. Then we use Monte Carlo simulations with 1000 points to estimate uncertainties in the physical conditions given by the *getCrossTemDen* task of PyNeb. For example, using [O III] $\lambda 4363/\lambda 4959+5007$ as a temperature indicator and the following density diagnostics: [Cl III] $\lambda 5538/\lambda 5518$, [Fe III] $\lambda 4658/\lambda 4702$, [O II] $\lambda 3726/\lambda 3729$, [S II] $\lambda 6731/\lambda 6716$ and [Ar IV] $\lambda 4740/\lambda 4711$, we estimate the convergence in T_e and n_e and their uncertainties in every case. Analogously, we use the rest of T_e -diagnostics. The central value of T_e or n_e corresponds to the median of the Monte Carlo distribution and the errors are represented by the deviations to 84th and 16th percentiles, corresponding to $\pm 1\sigma$ in the case of a Gaussian. After this procedure, all diagnostics (either T_e or n_e), will have a result for each cross-comparison.

For the nebular components on each cut, we define the representative n_e as the weighted mean⁴ in each cross-comparison with all the the temperature indicators. In the case of high-velocity components, the treatment is more complex since all the density diagnostics based on CELs reveal considerably higher densities than in the nebular components, reaching values at or above the critical densities of the atomic levels involved in some diagnostics as shown in Table D5. At densities of $10^4 - 10^6 \text{ cm}^{-3}$, diagnostics based on [Fe III] lines are more reliable than other classic ones such as [O II] $\lambda 3726/\lambda 3729$ or [S II] $\lambda 6731/\lambda 6716$. In addition, dust destruction processes release gaseous Fe in the shock front that should favor

⁴ The weights were defined as the inverse of the square of the error associated to each density diagnostic.

the larger contribution of the emission of [Fe III] lines of the post-shock gas and, therefore, the derived physical conditions would be biased to those of the post-shock zones. We adopted a maximum-likelihood method to determine the density from [Fe III] lines for the high-velocity components. This procedure and its interpretation is described in detail in Section 5.2.

Finally, using the adopted representative n_e , we calculate T_e with the available diagnostics using the *getTemDen* task of PyNeb. Assuming the scheme of two ionization zones, we define $T_{\text{e}}(\text{high})$ as the weighted mean T_e obtained from [Ar III] $\lambda 5192/\lambda 7136+7751$, [O III] $\lambda 4363/\lambda 4959+5007$ and [S III] $\lambda 6312/\lambda 9069+9531$ line ratios. Similarly, we define $T_{\text{e}}(\text{low})$ based on the resulting T_e obtained from [S II] $\lambda 4069+76/\lambda 6716+31$, [N II] $\lambda 5755/\lambda 6584$ and [O II] $\lambda 3726+29/\lambda 7319+20+30+31$ line ratios.

We note that in the nebular component of all cuts the observed [S III] $\lambda 9531/\lambda 9069$ line intensity ratio does not agree with the theoretical value. This is owing to strong telluric absorptions that affect the [S III] $\lambda 9069$ line that, on the other hand, do not affect the blueshifted lines of the high velocity components. After an inspection in the 2D spectra of the calibration star and in the science object, we concluded that [S III] $\lambda 9531$ is not affected by telluric absorptions or emissions at the earth velocities at which the observations were taken. In the nebular component of all cuts, we assumed the theoretical ratio $I([S \text{ III}] 9531)/I([S \text{ III}] 9069) = 2.47$ obtained from the atomic data given in Table D3 to estimate T_e ([S III]).

Plasma diagnostic plots shown in Fig. D1, indicate that the resulting values of each diagnostic are consistent with each other. The numerical values in each case are presented in Table 4.

5.2 Physical conditions based on [Fe III] lines.

As mentioned in Section 5.1, density diagnostics based on different [Fe III] line intensity ratios give apparently discordant results. This is mainly due to the ambivalence in the density dependence of some observed intensity ratios and/or due to their high dependence on T_e as well as on n_e . These two scenarios are exemplified in Fig. 5 for [Fe III] $\lambda 4881/\lambda 4658$ and $\lambda 5271/\lambda 4658$ line ratios, upper and middle panels, respectively. $\lambda 4881/\lambda 4658$ has a broad maximum around $n_e \sim 2 \times 10^4 \text{ cm}^{-3}$, so only becomes an accurate density diagnostic for $n_e < 5 \times 10^3 \text{ cm}^{-3}$ or $n_e > 10^5 \text{ cm}^{-3}$. In the case of $\lambda 5271/\lambda 4658$, the T_e dependence is always important except for some narrow density ranges between $\sim 10^2 \text{ cm}^{-3}$ and $\sim 10^3 \text{ cm}^{-3}$ and between $\sim 10^5 \text{ cm}^{-3}$ and $\sim 10^6 \text{ cm}^{-3}$. For the expected densities in the different components observed in this work (n_e between $\sim 10^3 \text{ cm}^{-3}$ and $\sim 10^5 \text{ cm}^{-3}$), these diagnostics are not very enlightening on their own. On the other hand, for $10^3 \text{ cm}^{-3} < n_e < 10^6 \text{ cm}^{-3}$, $\lambda 4658/\lambda 4702$ (see bottom panel of Fig. 5) varies monotonically with n_e and is insensitive to T_e . Thus, it is the most reliable diagnostic in our case.

We consider that the option to determine the physical conditions based on the observed intensity ratios of [Fe III] lines is using a maximum-likelihood process. This method is based on a χ^2 minimization by testing a wide range of parameters. The value of χ^2 is defined in Eq. (2), as the sum of the quadratic differences between the abundance of ion X^i (in this case Fe^{2+}) determined with each

Table 4. Physical conditions.

Diagnostic	Cut 1 Nebula	Cut 2 HH 529 II	Cut 3 HH 529 III	Cut 4 Nebula	Combined Cuts
Density					
[O II] $\lambda\lambda 3726/\lambda 3729$	5460 ⁺¹⁰⁰⁰ ₋₇₅₀	10570 ⁺³⁶⁸⁰ ₋₂₄₂₀	5220 ⁺⁹⁶⁰ ₋₇₂₀	18020 ⁺¹⁷¹⁷⁰ ₋₆₉₃₀	5530 ⁺¹⁰⁰⁰ ₋₈₀₀
[S II] $\lambda\lambda 6731/\lambda 6716$	4230 ⁺⁹⁶⁰ ₋₉₀₀	9390 ⁺¹⁰¹⁷⁰ ₋₃₉₅₀	4160 ⁺¹⁵⁷⁰ ₋₁₀₄₀	13130 ⁺¹⁵⁸²⁰ ₋₆₅₅₀	4130 ⁺²⁰²⁰ ₋₁₂₅₀
[Cl III] $\lambda\lambda 5538/\lambda 5518$	7020 ⁺⁹⁶⁰ ₋₉₀₀	8170 ⁺¹⁸¹⁰ ₋₁₆₁₀	6670 ⁺⁹²⁰ ₋₈₆₀	15040 ⁺⁵⁶²⁰ ₋₄₄₉₀	7370 ⁺¹¹⁹⁰ ₋₁₁₂₀
[Fe III] $\lambda\lambda 4658/\lambda 4702$	9260 ⁺³⁷⁰⁰ ₋₂₈₉₀	12390 ⁺⁵⁰¹⁰ ₋₃₄₆₀	8990 ⁺²⁸⁴⁰ ₋₂₃₅₀	33800 ⁺¹³⁸²⁰ ₋₁₀₅₃₀	10490 ⁺⁴²⁴⁰ ₋₃₀₉₀
[Ar IV] $\lambda\lambda 4740/\lambda 4711$	4480 ⁺¹⁷⁰⁰ ₋₁₆₄₀	6410 ⁺¹⁹⁰⁰ ₋₁₈₈₀	5920 ⁺⁹⁸⁰ ₋₉₄₀	15050 ⁺¹³³⁰⁰ ₋₉₂₄₀	6400 ⁺¹⁶⁹⁰ ₋₁₆₆₀
O II*	4710 ± 710	3490 ± 340	4390 ± 400	3600 ± 850	4920 ± 550
[Fe III]*	8530 ± 1050	11880 ± 1860	9430 ± 1010	30200 ± 8080	10330 ± 1700
Adopted	5830 ± 1210	11880 ± 1860	5870 ± 970	30200 ± 8080	6180 ± 1220
Temperature					
T(H I) Balmer	-	-	-	-	7520 ± 790
T(H I) Paschen	-	-	-	-	7550 ± 1160
T(He I)	8280 ⁺⁵²⁰ ₋₅₇₀	7200 ± 550	8060 ⁺⁵⁴⁰ ₋₅₁₀	7340 ± 710	8090 ± 530
[N II] $\lambda\lambda 5755/\lambda 6584$	9910 ± 250	10150 ⁺⁵⁷⁰ ₋₅₁₀	9850 ± 240	11040 ⁺⁹²⁰ ₋₉₇₀	10060 ⁺²⁶⁰ ₋₂₈₀
[O II] $\lambda\lambda 3726+29/\lambda\lambda 7319+20+30+31$	10340 ⁺¹³³⁰ ₋₉₄₀	-	-	-	11230 ⁺¹³³⁰ ₋₁₁₁₀
[S II] $\lambda\lambda 4069+76/\lambda\lambda 6716+31$	11430 ⁺⁵²⁹⁰ ₋₁₈₇₀	-	11070 ⁺²⁴²⁰ ₋₁₄₅₀	-	10550 ⁺²⁴⁵⁰ ₋₁₅₇₀
[O III] $\lambda\lambda 4363/\lambda\lambda 4959+5007$	8430 ± 90	8240 ± 80	8410 ⁺⁸⁰ ₋₇₀	8600 ⁺¹¹⁰ ₋₁₂₀	8510 ± 90
[S III] $\lambda\lambda 6312/\lambda\lambda 9069+9531$	9220 ⁺²⁹⁰ ₋₂₃₀	8670 ± 310	8990 ⁺²⁹⁰ ₋₃₃₀	9040 ⁺⁴¹⁰ ₋₄₂₀	8920 ⁺³³⁰ ₋₃₀₀
[Ar III] $\lambda\lambda 5192/\lambda\lambda 7136+7751$	8280 ⁺²⁸⁰ ₋₃₁₀	8620 ⁺⁵⁰⁰ ₋₅₄₀	8390 ⁺²²⁰ ₋₂₈₀	-	8250 ⁺²⁶⁰ ₋₂₉₀
O II*	-	-	9350 ± 1090	-	-
[Fe III]*	7800 ± 800	8500 ± 1050	8450 ± 730	7900 ± 1910	7970 ± 920
Thermal broadening	-	8670 ± 50	8340 ± 410	10470:	-
T_e (low) Adopted	9930 ± 140	10150⁺⁵⁷⁰₋₅₁₀	9860 ± 240	11040⁺⁹²⁰₋₉₇₀	10070 ± 270
T_e (high) Adopted	8470 ± 200	8270 ± 110	8440 ± 140	8630 ± 120	8510 ± 120
					8360 ± 140
					8480 ± 150

* A maximum likelihood method was used.

emission line included in the procedure and the weighted average of the abundance defined in Eq. (3).

$$\chi^2 = \sum_{\lambda} \frac{\left(n \left(\frac{X^i}{H^+} \right)_{\lambda} - \overline{n \left(\frac{X^i}{H^+} \right)} \right)^2}{\Delta n \left(\frac{X^i}{H^+} \right)_{\lambda}}, \quad (2)$$

$$\overline{n \left(\frac{X^i}{H^+} \right)} = \frac{\sum_{\lambda} \left(n \left(\frac{X^i}{H^+} \right)_{\lambda} / \Delta n \left(\frac{X^i}{H^+} \right)_{\lambda} \right)}{\sum_{\lambda} \left(1 / \Delta n \left(\frac{X^i}{H^+} \right)_{\lambda} \right)}. \quad (3)$$

This self-consistent procedure gives the physical parameters that minimize χ^2 with an associated uncertainty based on the resulting values within $\chi^2 - \chi^2_{\min} \leq 1$. This method requires a strict control on the variables that affect the line fluxes, otherwise a spurious contribution appears, and can change the resulting parameters that minimize χ^2 . For example, undetected blends in the studied lines can result in incorrect density and/or temperature determinations.

We have considered several aspects to choose the set of [Fe III] lines that should be included in the maximum-likelihood process. We discard lines with evident line blending or contamination by telluric emission or ghosts. To test unnoticed line blends or inaccuracies in flux estimations, we use ratios of observed lines that should depend only on transition probabilities and not on physical conditions. The results are shown in Table D6. As can be seen, there are some deviations between the theoretical and the observed values in the cases of [Fe III] $\lambda\lambda 4667/\lambda 4734$, $\lambda 4778/\lambda 4667$, $\lambda 4607/\lambda 4702$, $\lambda 4607/\lambda 4770$ and $\lambda 4881/\lambda 4987$ due to the contamination of [Fe III] $\lambda 4667$ by a ghost, by the blend of [Fe III] $\lambda 4607$ with N II $\lambda 4607.15$ and by the blend of [Fe III] $\lambda 4987.29$ with N II $\lambda 4987.38$. On the

other hand, we detect that $\lambda 4778$ line is 35% wider than the rest of the [Fe III] bright lines in HH 529 II, although, this is not observed in HH 529 III. This suggests that, due to the higher signal to noise ratio in the cut 2 spectrum, a line blend with an emission feature is detected in HH 529 II while for HH 529 III it remains below the detection level. The line ratio with the largest deviation is [Fe III] $\lambda 5011/\lambda 4085$. This could be mainly due to the low signal-to-noise ratio of the [Fe III] $\lambda 4085$ line. However, [Fe III] $\lambda 5011$ is located close to [O III] $\lambda 5007$, which presents broad wings in its line profile that affects the shape of the continuum close to [Fe III] $\lambda 5011$ and perhaps the measurement of its line flux. The presence of bright lines affecting the continuum shape in areas close to relatively weak [Fe III] lines may also contribute to some differences between the observed and predicted line ratios shown in Table D6. This problem is reduced by using the brightest line of each ratio in the maximum-likelihood process.

We select the following [Fe III] lines for the maximum-likelihood process: $\lambda\lambda 4658.17$, 4701.64 , 4734.00 , 4881.07 and 5270.57 . This selection includes the brightest [Fe III] lines that are free of blends or telluric emissions and/or absorptions. Moreover, these lines lie in a relatively small spectral range and hence, uncertainties in the reddening correction would have a negligible effect. This allows us to restrict the parameter space to electron density and temperature to test χ^2 . Studies of the primordial helium abundance have used similar maximum-likelihood procedures to calculate the He⁺ abundance and have found that this procedure can lead to degeneracies in the fitted parameters and χ^2 (see Olive & Skillman 2004; Aver et al. 2011, and references therein). Because of this, it is important to have an overview of the behavior of χ^2 in the complete parameter space. In Fig. 6 we present the convergence of χ^2 in the $n_e - T_e$ space for both high-velocity and nebular components of cut 2. As it can be seen, χ^2 falls into a single minimum in each case, corresponding to $T_e = 8500 \pm 1050$ K and $n_e = 11880 \pm 1860$ cm⁻³.

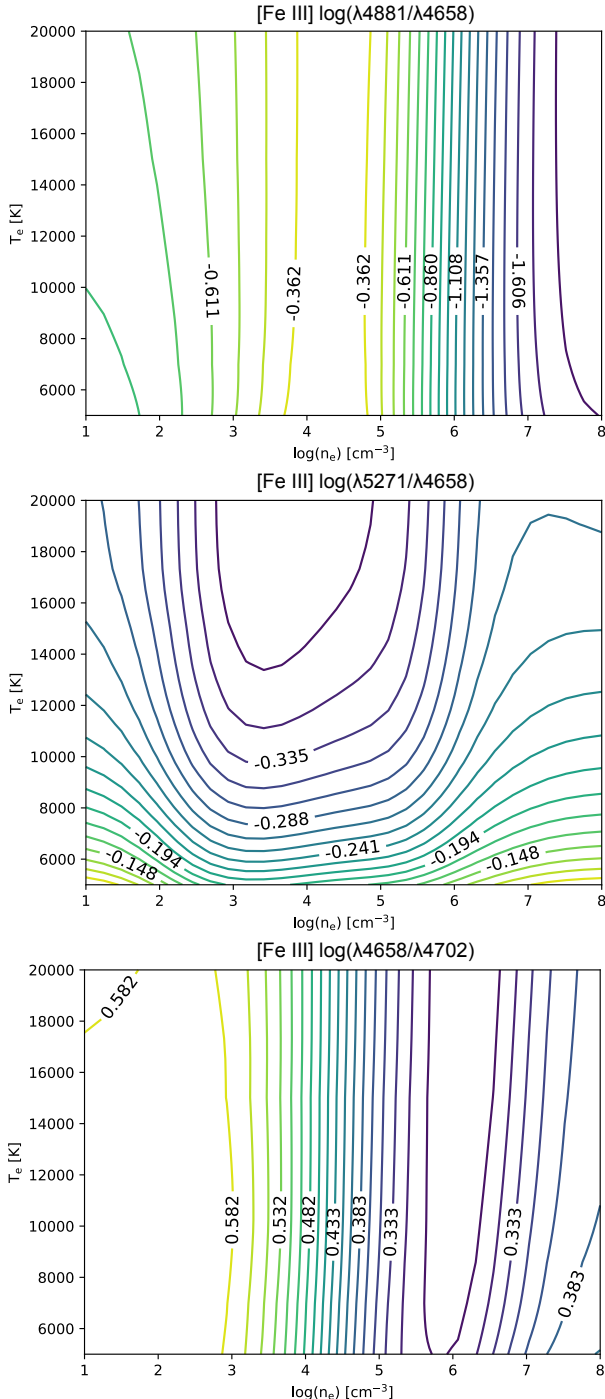


Figure 5. Predicted dependence of the [Fe III] $\lambda 4881/\lambda 4658$, $\lambda 5271/\lambda 4658$ and $\lambda 4658/\lambda 4702$ line intensity ratios with physical conditions.

for HH 529 II and $T_e = 8450 \pm 730$ K and $n_e = 9430 \pm 1010$ cm $^{-3}$ for the nebular component. The T_e and n_e values obtained for the rest of cuts using this approach are presented in Table 4. The convergence to the resulting n_e is consistent with the diagnostic based on [Fe III] $\lambda 4658/\lambda 4702$ ratio but with a smaller uncertainty due to the application of the χ^2 maximum-likelihood procedure. It is notable that in all cases, [Fe III] lines give n_e values higher than the usual diagnostics based on CELs such as [S II] $\lambda 6731/\lambda 6716$ or [O II] $\lambda 3726/\lambda 3729$. The largest difference is found in the high-velocity

components, in particular in HH 529 III. In the case of nebular components, the low dependence on density of some ratios such as $\lambda 4734/\lambda 4658$, $\lambda 4658/\lambda 4702$ or $\lambda 4734/\lambda 4702$ at density values smaller than $\sim 10^3$ cm $^{-3}$, gives more weight to the higher-density zones within the line of sight. On the other hand, in the high-velocity components, the larger differences suggest the presence of high densities in the range of $10^4 - 10^5$ cm $^{-3}$, where the usual density diagnostics, such as [S II] $\lambda 6731/\lambda 6716$ or [O II] $\lambda 3726/\lambda 3729$, are uncertain, being well above the critical densities, as is shown in Table D5. In addition, as found in HH 202 (Mesa-Delgado et al. 2009; Espíritu et al. 2017) and in this work (see Section 9.1.3), the gaseous Fe abundance is higher in the high-velocity components due to the dust destruction where the Fe is commonly depleted, thus, the flux of [Fe III] lines increase in the shock front, where the gas is being compressed. Therefore, the n_e determinations based on [Fe III] lines will be biased to the higher values of the density at the head of the shock although the volume of gas integrated in the high-velocity components include not only the denser gas of the head but also some contribution of the jet beam gas behind since it is fully photoionized and flowing towards the observer (see Section 12).

The results indicate a closer similarity between T_e ([Fe III]) and T_e (high), contrary to what the ionization potential of Fe $^{2+}$ would suggest, closer to N $^+$ than to O $^{2+}$, which are ions representative of the low and high ionization zones, respectively. In the case of the nebular components, the fact that the [Fe III] density diagnostics give more weight to the high-density zones in the line of sight, as we mentioned previously, may bias the results towards lower temperatures, which are not representative for all the Fe $^{2+}$. On the other hand, in the high-velocity components, this indicates that in the shock front, where further dust destruction and incorporation of Fe into the gas phase is expected, the high-ionization gas dominates over the remaining low-ionization one, which may be flowing behind of the shock front. This suggests that the optimal temperature to calculate the Fe $^{2+}$ abundance in the high-velocity components is T_e (high). Estimates of Fe $^{2+}$ abundances based on both T_e (low) and T_e (high) will be discussed separately in Section 9.1.3.

5.3 Physical conditions based on RLs.

5.3.1 Physical conditions based on O II RLs

To estimate physical conditions based on O II RLs, we use the effective recombination coefficients from Storey et al. (2017). These coefficients fully account the dependence on electron density and temperature of the population distribution among the ground levels of O II. We follow a similar maximum-likelihood procedure as described in Section 5.2 to derive the physical conditions. For this case, we chose the observed lines from multiplet 1 and $\lambda\lambda 4089.29, 4275.55$ from 3d-4f transitions, due to the following reasons: (1) lines from multiplet 1 are the brightest O II RLs and are comparatively less affected by line blending or instrumental reflections as is illustrated in Fig. 7 for cut 2. (2) The line ratios within multiplet 1 deviate from the local thermodynamic equilibrium (LTE) values for $n_e \leq 10^5$ cm $^{-3}$ (Storey et al. 2017), providing a density diagnostic. (3) O II $\lambda\lambda 4089.29, 4275.55$ RLs corresponding to 3d-4f transitions depend slightly stronger on T_e than the lines from multiplet 1 and their ratio with O II $\lambda 4649.13$ is practically insensitive to n_e , since the population of the levels that arise these lines depend on the population of the same 3P_2 ground level (Storey et al. 2017), giving a T_e diagnostic. Nevertheless, $\lambda\lambda 4089.29, 4275.55$ are relatively weak and we expect comparatively larger uncertainties in the T_e determinations than using diagnostics based on CELs.

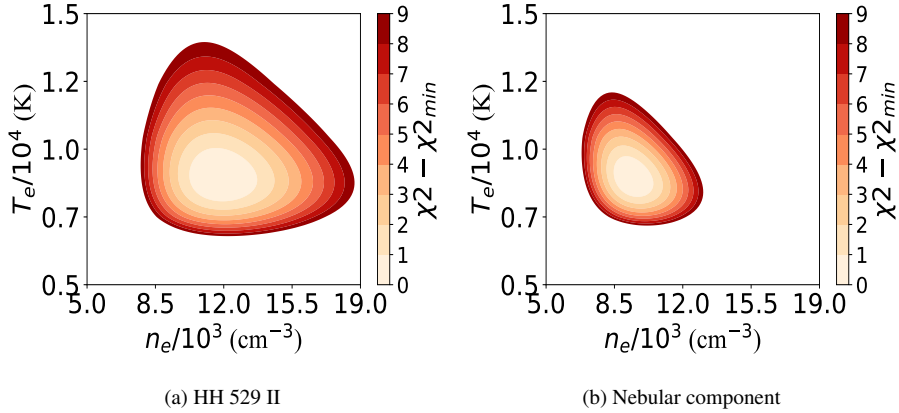


Figure 6. χ^2 in the space of T_e and n_e in the maximum-likelihood procedure for [Fe III] lines. Both in the case of HH 529 II (left panel) and the nebular component of cut 2 (right panel) there is a convergence to well defined physical conditions.

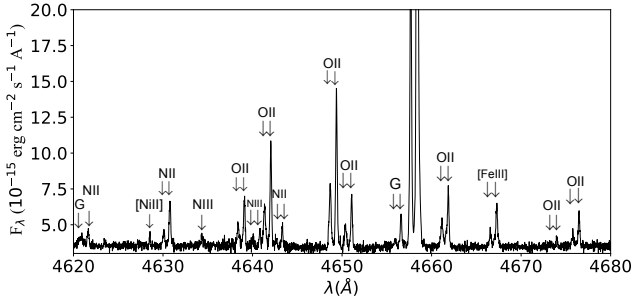


Figure 7. Section of the spectrum of the spatial cut 2 covering the spectral range 4620–4680 Å. Several couples of O II lines from multiplet 1 are present, showing the quality of the spectra of HH 529 II and the nebular component. Emissions marked with a G are ghosts (see Section A).

Fig. 8 shows χ^2 -maps in the space of T_e and n_e for both components of cut 2. As it can be seen, HH 529 II has a temperature degeneracy. This is not surprising, due to the fact that multiplet 1 is rather independent of T_e and the weak line $\lambda 4275.55$ is the only one that can break the degeneracy in this component since O II $\lambda 4089.29$ is blended with a ghost feature (see Section A). However, it is clear that the density dependence is well limited within a range of 3000–3700 cm^{-3} . Fixing the temperature to the adopted one for the high ionization zone using CELs, we obtain $n_e = 3490 \pm 340 \text{ cm}^{-3}$ for HH 529 II. On the other hand, since we were able to use the O II $\lambda 4089.29$ together with $\lambda 4275.55$ in the nebular component of cut 2, we have a convergence within a more limited interval of values. The physical conditions that minimizes χ^2 in this case are $n_e = 4390 \pm 400 \text{ cm}^{-3}$ and $T_e = 9350 \pm 1090 \text{ K}$. This result is compatible with $T_e(\text{[O III]})$ within the uncertainties, indicating that the emission of CELs and RLs of O^{2+} comes basically from the same gas (see Section 9.3).

In Table 4, we can see that the density values obtained from O II lines are similar to those obtained from other diagnostics in the nebular components but lower in the high-velocity ones. This may be because, although formally the population of the 3P_J levels from O^{2+} do not reach the statistical equilibrium until densities of $\sim 10^5 \text{ cm}^{-3}$, the density dependence becomes rather weak from values above $\sim 10^4 \text{ cm}^{-3}$, as it is shown in Fig. 4 from Storey et al. (2017). Therefore, the values obtained by this diagnostic may not be representative of the shock front, where the density is expected to be higher than 10^4 cm^{-3} but from a lower density component

flowing in the jet beam. A gas component with a density around $\sim 10^3 \text{ cm}^{-3}$ has larger deviations from LTE in the populations of the levels from which multiplet 1 arise. This might bias the results to lower values. However, this discrepancy may have a different origin, which requires further investigation.

5.3.2 Electron temperature from He I recombination line ratios

Following the procedure used by Zhang et al. (2005) for PNe, we have used the $I(\text{He I } \lambda 7281)/I(\text{He I } \lambda 6678)$ ratio for deriving T_e (He I) in our spectra. The use of those particular lines have several advantages. First, $\lambda 7281$ and $\lambda 6678$ are among the brightest He I RLs and their use minimizes observational errors. Second, they are produced in transitions between singlet levels, ensuring that they are free of significant self-absorption effects. We have explored the temperature dependence of other intensity ratios of He I $\lambda 7281$ with respect to other relevant singlet lines ($\lambda\lambda 4388, 4922, 4438, 3614, 3965$ and 5016) using the recombination coefficients of Porter et al. (2012, 2013). Intensity ratios of transitions coming from 1S , 1D , 3D levels to 2P show the strongest dependence on T_e (see Fig. D4). 2P is the same lower level of the transition producing the He I $\lambda 7281$ line, which comes from the 3S level. On the other hand, comparatively, the $I(\text{He I } \lambda 7281)/I(\text{He I } \lambda 6678)$ ratio has the weakest n_e dependence, in agreement with the conclusion of Zhang et al. (2005), despite using different recombination coefficients.

Fig. D5 shows that the T_e dependence of $I(\text{He I } \lambda 7281)/I(\text{He I } \lambda 6678)$ ratio is practically linear in the interval $5000 \text{ K} \leq T_e(\text{K}) \leq 10000 \text{ K}$. The deviation between the determination of $T_e(\text{He I})$ using a linear fit (as in Eq. (4)) and a more complex interpolation of the recombination coefficients of Porter et al. (2012, 2013) is always smaller than 35 K. At $T_e > 10000 \text{ K}$, any linear fit will fail for almost all n_e values except for the lowest ones ($n_e \leq 100 \text{ cm}^{-3}$). In these cases, a more complex treatment is necessary to estimate $T_e(\text{He I})$. The linear fit (slope and intercept) varies significantly in the lower density ranges, and tends to remain almost constant for densities $n_e \geq 10000 \text{ cm}^{-3}$.

$$T_e(\text{He I}) (\text{K}) = \alpha \left[\frac{I(\lambda 7281)}{I(\lambda 6678)} \right] + \beta. \quad (4)$$

In Table D7, we present the slope and intercept values given by Eq. (4) for a density range representative for H II regions and some PNe. The resulting $T_e(\text{He I})$, using the average values obtained with

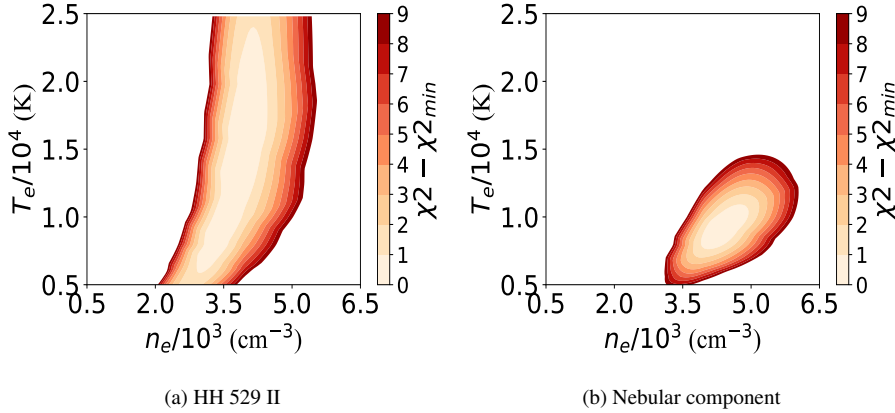


Figure 8. The same as in Fig. 6 but using O II lines. In this case, there is an evident T_e degeneracy in HH 529 II (left panel) because that the temperature-dependent O II RL $\lambda\lambda 4089.29$ cannot be measured in its spectrum. A clear convergence can be seen in the nebular component (right panel). The uncertainties are somewhat large owing to the relative weakness of the temperature-dependent O II lines ($\lambda\lambda 4089.23, 4275.55$).

$I(\lambda 7281)/I(\lambda 6678)$, $I(\lambda 7281)/I(\lambda 4922)$ and $I(\lambda 7281)/I(\lambda 4388)$ ratios, are all consistent with each other and are included in Table 4 for all components.

5.4 Electron temperature determinations from nebular continuum.

Thanks to the high signal-to-noise ratio of our spectra, we can obtain a good determination of the Balmer and Paschen discontinuities of the nebular continuum in the spectrum obtained adding all the cuts (see Fig. 9). We used Eq. (5), taken from Liu et al. (2001) for $\text{He}^{2+}/\text{H}^+ = 0$ to estimate $T_e(\text{HI})_{\text{Balmer}}$. This formula is based on theoretical continuum emission of H I, He I and He II calculated by Brown & Mathews (1970) and the theoretical line emission of H I $\lambda 3770.63$ (H11) from Storey & Hummer (1995). Analogously, we used Eq. (6), taken from Fang & Liu (2011) to estimate $T_e(\text{HI})_{\text{Paschen}}$ using the measured Paschen discontinuity and the intensity of H I $\lambda 8862.78$ (P11) line.

$$T_e(\text{HI})_{\text{Balmer}}(\text{K}) = 368 \times \left(1 + 0.259 \frac{\text{He}^+}{\text{H}^+}\right) \left(\frac{\text{BJ}}{\text{H11}}\right)^{-3/2}. \quad (5)$$

$$T_e(\text{HI})_{\text{Paschen}}(\text{K}) = 8.72 \times \left(1 + 0.52 \frac{\text{He}^+}{\text{H}^+}\right) \left(\frac{\text{PJ}}{\text{P11}}\right)^{-1.77}. \quad (6)$$

The estimation of the temperature requires a precise fit to the continuum emission at both sides of 3646 Å and 8204 Å, the approximate wavelengths of the Balmer and Paschen discontinuities, respectively, since both estimations are very sensitive to changes in the jump value. We do not determine $T_e(\text{HI})_{\text{Balmer}}$ and $T_e(\text{HI})_{\text{Paschen}}$ in the remaining cuts because of the much larger noise level of the continuum in their spectra. However, using the spectrum of the combined cuts has the drawback of mixing the emission of the nebular and the high-velocity components in the continuum. In any case, as Bohigas (2015) suggests, the total $T_e(\text{HI})$ would be the weighted average of the individual values of the mixed components, where the weight would be the H^+ mass of each component. Thus, given that the high-velocity component should contain a much smaller mass, we can assume that the contribution of the high-velocity component to the continuum should be small, not affecting the $T_e(\text{HI})$ determination in a substantial manner.

Fig. 9 shows the discontinuities and the fitted Balmer and

Paschen continua in the normalized and reddening corrected spectrum. The best fit is achieved with $\text{BJ}/I_{H\beta} = 0.532 \pm 0.036$ and $\text{PJ}/I_{H\beta} = 0.031 \pm 0.002$.

6 CHEMICAL ABUNDANCES

6.1 Ionic abundances from CELs

We determine the ionic abundances based on the observed CELs using the PyNeb routines and the transition probabilities and collision strengths given in Table D3. Abundances for O^+ , N^+ , S^+ , Ni^{2+} and Cl^+ were derived using the n_e and $T_e(\text{low})$ adopted for each component of each cut, while abundances for O^{2+} , Ne^{2+} , Cl^{3+} , Fe^{3+} , Ar^{2+} and Ar^{3+} rely on the adopted $T_e(\text{high})$. S^{2+} and Cl^{2+} abundances were derived using $T_e(\text{[S III]})$ (see Section B). In the case of Fe^{2+} , estimations of its abundance are presented using both $T_e(\text{high})$ and $T_e(\text{low})$ (see Table D8 and Table D9). This will be analysed in Section 9.1.3. General results are presented in Table 5.

6.2 Ionic abundances from RLs

6.2.1 He^+ abundance

To estimate the He^+ abundance, we use the flux of some of the most intense He I lines: $\lambda\lambda 3188, 3614, 3889, 3965, 4026, 4388, 4438, 4471, 4713, 4922, 5016, 5876, 6678, 7065, 7281$. He I $\lambda\lambda 4121, 5048$ lines were discarded because they are contaminated by ghost lines (see Section A). The 15 selected lines correspond to both singlet and triplet configurations, as it is shown in Fig. D4. The fluxes of triplet lines are affected by the metastability of the 2^3S level. The comparatively much longer lifetime of 2^3S means that transitions to this level can become optically thick, altering the flux ratios predicted by recombination theory for some He I lines. For example, self-absorption of He I $\lambda 3188$ photons can increase the flux of He I $\lambda\lambda 3889, 5876$ and 7065 lines at the expense of He I $\lambda 3188$, which flux decreases accordingly. On the other hand, self-absorption of the He I $\lambda 3889$ line is also important and increase the flux of He I $\lambda 7065$ at the expense of He I $\lambda 3889$. However, the sum of the fluxes of He I $\lambda\lambda 3188, 3889, 4713, 5876$, and 7065 lines should remain independent of the optical depth (parameterized by τ_{3889} or τ_{3188} ; Porter et al. 2007).

In Table D13, we show the He^+ abundances determined using

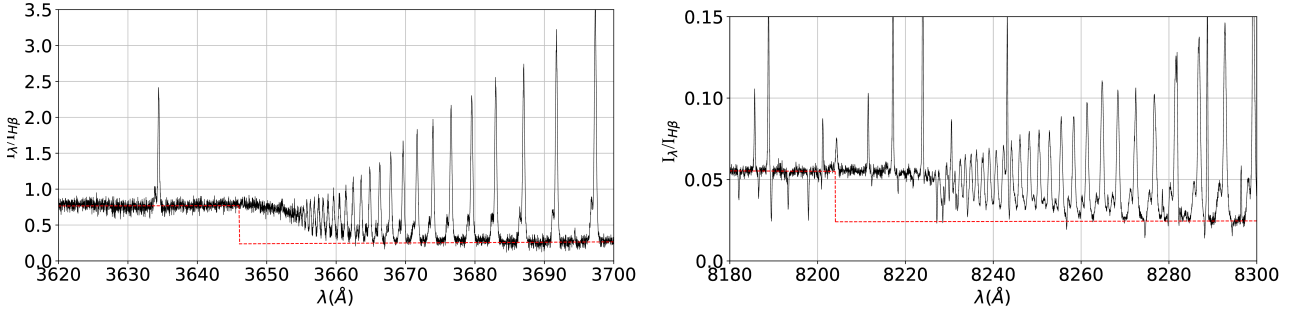


Figure 9. Reddening-corrected spectrum resulting after adding all cuts, showing the Balmer (left panel) and Paschen (right panel) discontinuities. Both jump estimations are shown in red.

Table 5. Chemical abundances based on CEL's without considering the temperature fluctuations scenario ($t^2 = 0$).

Ion	Cut 1		Cut 2		Cut 3		Cut 4	Combined cuts
	Nebula	HH 529 II	Nebula	HH 529 III	Nebula	Nebula	Nebula	
O ⁺	7.88 ± 0.04	$7.36^{+0.12}_{-0.09}$	$7.83^{+0.06}_{-0.05}$	$7.51^{+0.22}_{-0.14}$	$7.76^{+0.07}_{-0.06}$	$7.81^{+0.07}_{-0.06}$	7.75 ± 0.05	
O ²⁺	8.32 ± 0.03	$8.54^{+0.03}_{-0.02}$	8.35 ± 0.03	$8.48^{+0.03}_{-0.02}$	$8.35^{+0.03}_{-0.02}$	8.36 ± 0.03	8.37 ± 0.03	
N ⁺	7.00 ± 0.02	$6.19^{+0.06}_{-0.05}$	6.99 ± 0.03	$6.45^{+0.12}_{-0.08}$	$6.91^{+0.04}_{-0.03}$	$6.98^{+0.04}_{-0.03}$	6.89 ± 0.03	
Ne ²⁺	7.67 ± 0.04	7.91 ± 0.03	$7.70^{+0.04}_{-0.03}$	7.80 ± 0.03	7.73 ± 0.03	$7.75^{+0.04}_{-0.03}$	$7.73^{+0.04}_{-0.03}$	
S ⁺	5.58 ± 0.05	$4.88^{+0.08}_{-0.07}$	$5.57^{+0.05}_{-0.04}$	$5.17^{+0.15}_{-0.12}$	$5.53^{+0.06}_{-0.05}$	5.59 ± 0.05	5.49 ± 0.05	
S ²⁺	6.79 ± 0.04	$6.92^{+0.05}_{-0.04}$	$6.85^{+0.09}_{-0.07}$	$6.89^{+0.06}_{-0.05}$	$6.86^{+0.05}_{-0.04}$	$6.82^{+0.05}_{-0.04}$	6.85 ± 0.04	
Cl ⁺	3.72 ± 0.04	$2.95^{+0.14}_{-0.13}$	3.71 ± 0.04	<3.34	3.68 ± 0.04	3.75 ± 0.04	3.63 ± 0.04	
Cl ²⁺	$4.88^{+0.06}_{-0.05}$	$5.01^{+0.06}_{-0.05}$	$4.93^{+0.06}_{-0.05}$	$5.03^{+0.08}_{-0.07}$	$4.96^{+0.06}_{-0.05}$	$4.95^{+0.06}_{-0.05}$	$4.94^{+0.05}_{-0.04}$	
Cl ³⁺	3.28 ± 0.06	3.60 ± 0.05	$3.28^{+0.04}_{-0.03}$	3.40 ± 0.10	3.33 ± 0.04	3.45 ± 0.04	3.38 ± 0.05	
Ar ²⁺	6.31 ± 0.03	6.39 ± 0.02	6.31 ± 0.03	6.36 ± 0.03	6.33 ± 0.02	6.29 ± 0.03	6.32 ± 0.03	
Ar ³⁺	$4.39^{+0.06}_{-0.05}$	$4.67^{+0.04}_{-0.03}$	$4.47^{+0.04}_{-0.03}$	4.51 ± 0.07	4.50 ± 0.04	$4.61^{+0.04}_{-0.03}$	$4.52^{+0.05}_{-0.04}$	
*Fe ²⁺	5.77 ± 0.02	5.94 ± 0.05	5.82 ± 0.02	5.75 ± 0.05	5.78 ± 0.02	5.76 ± 0.03	5.80 ± 0.02	
**Fe ²⁺	5.52 ± 0.03	5.62 ± 0.07	5.57 ± 0.02	5.40 ± 0.06	5.52 ± 0.04	5.48 ± 0.03	5.53 ± 0.04	
Fe ³⁺	$5.68^{+0.13}_{-0.11}$	$6.25^{+0.10}_{-0.09}$	$5.70^{+0.09}_{-0.08}$	<6.58	$5.73^{+0.11}_{-0.10}$	$5.73^{+0.13}_{-0.12}$	$5.75^{+0.11}_{-0.10}$	
Ni ²⁺	4.37 ± 0.14	4.50 ± 0.08	4.33 ± 0.17	$4.28^{+0.15}_{-0.11}$	4.32 ± 0.16	4.36 ± 0.12	4.38 ± 0.10	

* indicates that T_e (high) was used.

** indicates that T_e (low) was used.

the fluxes of He I $\lambda\lambda 3188, 3889, 4713, 5876$, and 7065 lines and the values of n_e and $T_e(\text{He I})$ corresponding to each component of each cut. In the same table, we also include the He⁺ abundance obtained from the sum of the fluxes of all the individual lines of the table and re-distributing them assuming $\tau_{3188} = \tau_{3889} = 0$. In Table D14 we show the He⁺ abundances determined from singlet lines and those triplet ones that are expected to be less affected by self-absorption (see Table 2 from Benjamin et al. 2002). Tables D13 and D14 show a good agreement between the average values of He⁺/H⁺ ratios included in Table D14 (the last row) and those obtained summing the fluxes of the lines included in Table D13. This last table also shows that the self-absorption effects are less important in the high-velocity components than in the nebular one. This is noticeable in the lower dispersion of the abundances obtained with individual lines in the high-velocity components. As discussed in Osterbrock & Ferland (2006, see their figure 4.5) if the nebula has ionized zones at different velocities, the self-absorption effects can be reduced due to the Doppler shift between the emitting and absorbing zones. For example, the effect of self-absorption in the intense He I $\lambda 5876$ line is notable in the nebular component, giving He⁺ abundances about 0.05 dex higher than the sum value. In this

sense, the common procedure of using a flux-weighted average of He I $\lambda 5876$ and other bright optical He I lines (as $\lambda 4471$ and $\lambda 6678$) for obtaining the mean He⁺ abundance would provide rather an upper limit of it.

Another interesting fact that can be noted in Table D14 is that the He⁺ abundance determined from the He I $\lambda 5016$ line is lower than the values obtained from other lines in the high-velocity components. An abnormally low flux of this line was noted by Esteban et al. (2004), and this was attributed to self-absorption effects in the singlet configuration of He I. Porter et al. (2007) discussed this, proposing that the most likely explanation is a deviation from case B of the He I $\lambda\lambda 537.0$ and 522.0 lines, that go to the ground level, partially escaping before being reabsorbed. This is probably the case in the high-velocity components where any kind of self-absorption of photons emitted by the “static” nebular gas should be reduced. The adopted He⁺/H⁺ values are presented in Table 6.

6.2.2 O^{2+} abundance

In Table D15, we present the O^{2+} abundance obtained from RLs of O II. We use T_e (high) and the values of n_e obtained from O II (see section 5.3.1) and [Fe III] lines for the nebular and high-velocity components, respectively. We used the recombination coefficients calculated by Storey et al. (2017) that consider the distribution of population among the O^{2+} levels with some improvements over similar estimates from Bastin & Storey (2006). Previous references (as Storey 1994) assumed that the O^{2+} levels are populated according to their statistical weight, which is not suitable for densities below the critical one.

In Table D15, we also present the weighted average abundance for each multiplet. In the last row of Table D15 we give the O^{2+} abundance obtained averaging the values obtained for multiplets 1, 2, 10, 20 and $3d - 4f$ transitions. These multiplets and transitions give consistent values and were also considered by Esteban et al. (2004) for determining their mean values. However, we decided to consider only the abundance obtained from multiplet 1 as representative of the O^{2+} abundance, as we show in Table 6. This is because, although it gives values consistent with the average of the other aforementioned multiplets and transitions, the inclusion of multiplets with fainter lines increases the formal uncertainties of the final mean O^{2+} abundance.

6.2.3 Determination of the abundance of other heavy elements based on RLs.

Due to the high quality of our deep spectra, we were able to determine abundances of other heavy element ions such as O^+ , C^{2+} and Ne^{2+} based on the fluxes of RLs and the recombination coefficients presented in Table D4.

O^+ abundances were obtained from the lines of multiplet 1 of O I $\lambda\lambda 7771.94, 7774.17$ and 7775.39 together with the adopted density and temperature of the low ionization zone for each component of each cut. Due to the high spectral resolution of our data, these O I lines are not blended with telluric emission features, as is shown in Fig 10. We do not detect the lines of multiplet 1 of O I in the high-velocity components. In these cases, we have estimated upper limits of their intensity and corresponding abundances considering an hypothetical line with a flux of 3σ of the rms of the adjacent continuum. The resulting O^+ abundances and the estimated upper limits for the high-velocity components are shown in Table 6.

For C^{2+} and Ne^{2+} , we adopt the temperature of the high ionization zone for each component of each cut. C II RLs from different transitions were considered to derive C^{2+} abundances, as is shown in Table D16. Multiplet 6 of C II present two lines at 4267.00 and $4267.18 + 4267.26$ Å resolved at our spectral resolution, as shown in Fig. 11. In general, lines from all multiplets of C II considered give consistent values of C^{2+} abundances. RLs from multiplet 1 of Ne II were used to calculate the Ne^{2+} abundance. Although they are rather faint lines (see Fig. 12), the Ne^{2+} abundances derived from Ne II $\lambda\lambda 3694.21$ and 3766.26 lines for each component of cut 2 are consistent with each other. In addition, the Ne^{2+} abundance we derive for the nebular component in cuts 2 and 3 is in good agreement with that obtained by Esteban et al. (2004, see their Table 11).

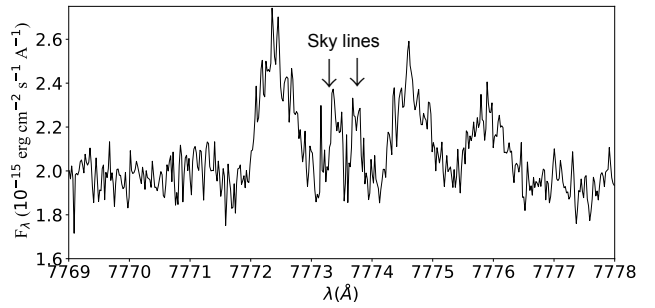


Figure 10. Lines of multiplet 1 of OI ($3s^5S^0-3p^5P$) in the spatial cut 2. No emission from HH 529 II is observed, only the nebular component is noticeable. These lines are produced from transitions of quintet levels (Grandi 1975a) and arise purely by recombination. Due to high spectral resolution and the earth motion during the observations, these lines are free of blending with sky lines.

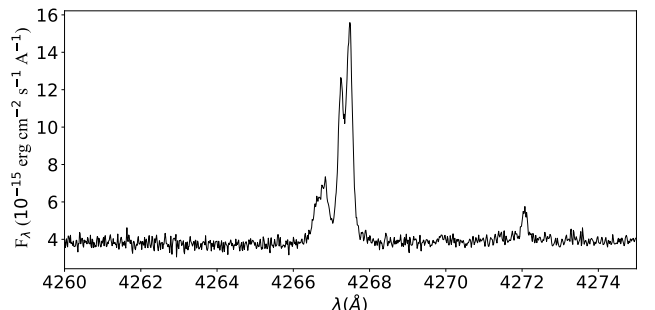


Figure 11. Lines of multiplet 6 of CII ($3d^2D-4f^2F^0$) in the spatial cut 2. Due to our high spectral resolution, we can partially separate $\lambda 4267.00$ from $\lambda 4267.18 + \lambda 4267.26$ both in the component corresponding to HH 529 II and to the nebular one.

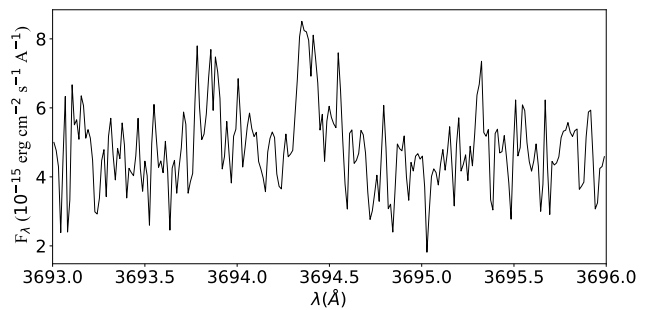


Figure 12. Lines of multiplet 1 of NeII ($3s^4P-3p^4P^0$) in the spatial cut 2.

7 TEMPERATURE FLUCTUATIONS

Following the procedure described by Peimbert (1967), we define the average temperature as it is shown in Eq. (7) and the mean square temperature fluctuation as in Eq. (8).

$$T_0 = \frac{\int T_e n_e n_i dV}{\int n_e n_i dV}, \quad (7)$$

$$t^2 = \frac{\int (T_e - T_0)^2 n_e n_i dV}{T_0 \int n_e n_i dV}. \quad (8)$$

In the case of a temperature derived from the ratio of two

Table 6. Chemical abundances based on RL's.

Ion	Cut 1		Cut 2		Cut 3		Cut 4	
	Nebula	HH 529 II	Nebula	HH 529 III	Nebula	Nebula	Combined cuts	
He ⁺	10.89 ± 0.02	10.95 ± 0.03	10.90 ± 0.01	10.95 ± 0.03	10.90 ± 0.02	10.91 ± 0.02	10.91 ± 0.02	
O ⁺	8.34 ± 0.10	< 7.91	8.25 ± 0.06	< 7.95	8.28 ± 0.07	8.27 ± 0.07	8.19 ± 0.07	
O ²⁺	8.47 ± 0.04	8.83 ± 0.07	8.52 ± 0.02	8.84 ± 0.09	8.52 ± 0.03	8.53 ± 0.03	8.58 ± 0.02	
C ²⁺	8.34 ± 0.03	8.46 ± 0.02	8.35 ± 0.03	8.56 ± 0.03	8.34 ± 0.03	8.33 ± 0.02	8.37 ± 0.03	
Ne ²⁺	-	8.60 ± 0.06	8.07 ± 0.03	-	8.04 ± 0.15	-	-	

quantities that depend on two different powers of temperature, α and β respectively (as the case of the temperature derived from RLs or the ratio between the Balmer or Paschen discontinuities and the flux of any H I line), the measured temperature $T_{\alpha/\beta}$ depends on t^2 and T_0 as follows:

$$T_{\alpha/\beta} = T_0 \left(1 - \frac{\alpha + \beta - 1}{2} t^2 \right). \quad (9)$$

On the other hand, two quantities with an individual temperature dependence proportional to $\frac{e^{\frac{\Delta E}{kT}}}{T^{1/2}}$, as the intensity of CELs, will produce a line intensity ratio with a temperature dependence on $e^{\frac{\Delta E_2 - \Delta E_1}{kT_{\lambda_1/\lambda_2}}}$. We can derive the temperature T_{λ_1/λ_2} :

$$T_{\lambda_1/\lambda_2} = T_0 \left[1 + \left(\frac{\Delta E_1 + \Delta E_2}{kT_0} - 3 \right) \frac{t^2}{2} \right] \quad (10)$$

When α and β in Eq. (9) are negative, the low-temperature zones within the line of sight will have a larger weight on $T_{\alpha/\beta}$, while in the cases where $\frac{\Delta E_1 + \Delta E_2}{kT_0}$ is larger than 3, the contribution of the high-temperature zones will be more important (Peimbert 1967).

On the basis of Eq. (9) and the estimations of the α and β coefficients given by Peimbert & Costero (1969) and Zhang et al. (2005), for the H I and He I temperature, respectively, we have Eq. (11) and Eq. (12).

$$T_e(\text{H I})_{\text{BJ-PJ}} = T_0 \left(1 - 1.67 t^2 \right), \quad (11)$$

$$T_e(\text{He I})_{7281/6678} = T_0 \left(1 - 1.07 t^2 \right). \quad (12)$$

On the other hand, for estimations of temperatures based on intensity ratios of CELs, we have Eq. (13), Eq. (14) and Eq. (15).

$$T_e([\text{O III}])_{4363/4959+5007} = T_0 \left[1 + \left(\frac{91300}{T_0} - 3 \right) \frac{t^2}{2} \right], \quad (13)$$

$$T_e([\text{S III}])_{6312/9069+9531} = T_0 \left[1 + \left(\frac{54000}{T_0} - 3 \right) \frac{t^2}{2} \right], \quad (14)$$

$$T_e([\text{N II}])_{5755/6584} = T_0 \left[1 + \left(\frac{68950}{T_0} - 3 \right) \frac{t^2}{2} \right]. \quad (15)$$

We have applied the combination of Eq. (11) and Eq. (13) using $T_e(\text{H I})$ and $T_e([\text{O III}])$ to estimate t^2 (Peimbert 2003; Esteban et al. 2004; García-Rojas et al. 2004, 2005, 2007). Implicitly, this assumes that $t^2(\text{H}^+) \approx t^2(\text{O}^{2+})$ and $T_0(\text{H}^+) \approx T_0(\text{O}^{2+})$. The same procedure has been used with Eq. (14) and Eq. (15) (Peimbert & Costero 1969; Esteban et al. 1998) in order to estimate representative values of t^2 for different ionization zones. In Table (7), we show the t^2 and T_0 values obtained for each combination of the temperature indicators in the spectrum of the combined cuts, the only one where all the different temperature indicators are available. We have to emphasize the excellent agreement between the results obtained by combining $T_e(\text{H I})$ and the T_e diagnostics based on CELs ratios with that which is obtained using $T_e(\text{He I})$.

However, the above procedure may not be entirely accurate. From equations (7) and (8), it is clear that the values of t^2 and T_0 depend on the integrated volume. Thus, since each ion X^{i+} will have its own Strömgren sphere, each one will have a representative $t^2(X^{i+})$ and $T_0(X^{i+})$. Considering another ion, Y^{i+} , the assumption $t^2(X^{i+}) \approx t^2(Y^{i+})$ will be only correct if X^{i+} and Y^{i+} occupy the same nebular volume. In the case of H^+ and O^{2+} , if there is an appreciable amount of O in other states apart from O^{2+} , the value of $t^2(\text{H}^+)$ may differ from $t^2(\text{O}^{2+})$. Based on a set of Cloudy photoionization models with different input parameters, Kingdon & Ferland (1995) derived t^2 in two manners: as t_{str}^2 from the formal definition of Eq. (8) and the t_{obs}^2 obtained from the comparison of equations (11) and (13). They found that generally $t_{\text{str}}^2 \neq t_{\text{obs}}^2$, with the difference increasing with the T_{eff} of the ionizing sources. However, for the T_{eff} typical of the ionizing stars of H II regions (between 30,000 and 50,000 K), the approximation $t_{\text{str}}^2 \approx t_{\text{obs}}^2$ seems to be valid. The main drawback one faces in determining t_{obs}^2 is its high intrinsic uncertainty. As we mentioned in Section 5.4, the determination of temperature based on the Balmer or Paschen discontinuities is very sensitive to the noise level of the nebular continuum around the position of the discontinuities. The sources of uncertainty in $T_e(\text{He I})$ are slightly smaller, but they are still important. Assuming the two ionization zones scheme for H II regions, a better approximation to t^2 can be obtained using equations (16) and (17), proposed by Peimbert et al. (2002).

$$\gamma = \frac{\int n_e(\text{O}^+) dV}{\int n_e(\text{O}^+) dV + \int n_e(\text{O}^{2+}) dV}, \quad (16)$$

$$T_0(\text{H}^+) = \gamma T_0(\text{O}^+) + (1 - \gamma) T_0(\text{O}^{2+}). \quad (17)$$

To use Eq. (17), we need to estimate the fraction of the total O in O^+ form. For the spectrum of the combined cuts, γ varies from

Table 7. t^2 and T_0 derived from the different combinations of Eq. (11) and Eq. (12) with Eq. (13), Eq. (14) and Eq. (15) for the spectra of all cuts combined.

	$T_e(\text{[O III]})$		$T_e(\text{[S III]})$		$T_e(\text{[N II]})$	
	t^2	T_0	t^2	T_0	t^2	T_0
$T_e(\text{H I})_{\text{BJ}}$	0.020 ± 0.017	7770 ± 850	0.051 ± 0.030	8240 ± 980	0.068 ± 0.023	8510 ± 960
$T_e(\text{H I})_{\text{PJ}}$	0.019 ± 0.025	7800 ± 1260	0.050 ± 0.042	8250 ± 1420	0.068 ± 0.033	8530 ± 1430
$T_e(\text{He I})$	0.018 ± 0.012	7840 ± 520	0.054 ± 0.024	8160 ± 570	0.075 ± 0.018	8360 ± 570

0.36 to 0.23 according to whether the abundances are determined from RLs or CELs, respectively. A reasonable approximation is to take the average value $\gamma \approx 0.3$. On the other hand, He^+ should be present in both, the O^+ and O^{2+} zones. Although there may be coexistence of He^0 and H^+ , the volume that He^0 occupies should be small at the ionization conditions of the Orion Nebula and it can be assumed that the volume containing H^+ and He^+ should be approximately the same. This assumption is reinforced by the fact that the parameter $\eta = (\text{O}^+/\text{O}^{2+})(\text{S}^{2+}/\text{S}^+)$ (Vilchez & Pagel 1988), which is a measure of the radiation hardness and is correlated with the T_{eff} of the ionizing source, has a value of $\log(\eta) = 0.74$ for the “combined cuts” spectrum. Pagel et al. (1992) showed that for $\log(\eta) < 0.9$, the amount of He^0 is negligible for a large variety of photoionization models. Therefore, we can assume $T_0(\text{H}^+) \approx T_0(\text{He}^+)$ and $t^2(\text{H}^+) \approx t^2(\text{He}^+)$. Based on the previous discussion, we use Eq. (11) and Eq. (12) for the “combined cuts” spectrum, obtaining $t^2(\text{H}^+) \approx 0.036$ and $T_0(\text{H}^+) \approx 8000$ K. Using these values in Eq. (17) and assuming that the volume occupied by O^+ and N^+ is the same, and that to first order, $\frac{T_e(\text{[O III]})}{T_e(\text{[N II]})} \approx \frac{T_0(\text{O}^{2+})}{T_0(\text{N}^+)} \approx 0.85$, we obtain $T_0(\text{O}^{2+}) \approx 7580$ and $T_0(\text{N}^+) \approx 8950$. Then, from Eq. (13) and Eq. (15), we estimate $t_{\text{high}}^2 = t^2(\text{O}^{2+}) \approx 0.025$ and $t_{\text{low}}^2 = t^2(\text{N}^+) \approx 0.050$.

The remarkably good agreement between the values obtained with Eq. (17) and those presented in Table 7 reinforces the suitability of the temperature fluctuations paradigm to describe the results in the “combined cuts” spectrum. Considering the numerical values obtained for the “combined cuts” spectrum, we adopt the average values $t_{\text{high}}^2 = 0.021 \pm 0.003$, $t_{\text{inter}}^2 = 0.051 \pm 0.009$ and $t_{\text{low}}^2 = 0.064 \pm 0.011$, where the uncertainties correspond to the standard deviation of the average. Unfortunately, $T_e(\text{H I})$ based on the Balmer and Paschen discontinuities can not be calculated for the individual components of the different cuts, and the estimations of t^2 must rely exclusively on the calculated $T_e(\text{He I})$. However, calculations following the same procedure as the previously described to obtain the values presented in Table 7 for the individual components of each cut show similar results. These values are presented in Table D17. Considering the higher uncertainty of the estimated t^2 based on $T_e(\text{He I})$ without using $T_e(\text{H I})$, we adopt the values of the “combined cuts” spectrum as representative for the other components of each cut.

Using Eq. (15), Eq. (14) and Eq. (13) with the adopted t^2 values for each ionization zone, T_0 is estimated in each case for all components. Following the same scheme described in Section 6.1, we estimate the ionic abundances within the the paradigm of temperature inhomogeneities and the results are shown in Table 8.

8 THE ABUNDANCE DISCREPANCY FACTOR

A major problem in the analysis of photoionized regions is the discrepancy between the chemical abundances derived from RLs

and CELs, known as the abundance discrepancy (AD) problem. The relatively weak RLs, give systematically higher abundances than CELs. This difference is commonly quantified through the abundance discrepancy factor (ADF, Liu et al. 2000), defined here as:

$$\text{ADF}\left(X^i\right) = \log\left(\frac{n(X^i)_{\text{RLs}}}{n(X^i)_{\text{CELS}}}\right). \quad (18)$$

There is an extensive collection of works dedicated to this problem in the literature (see Torres-Peimbert et al. 1980; Liu et al. 2001; Stasińska et al. 2007; García-Rojas & Esteban 2007; Tsamis et al. 2011; Nicholls et al. 2012; Gómez-Llanos & Morisset 2020, and references therein). Although there is no definitive solution, there are several hypotheses to explain the AD. For example, temperature fluctuations (see Section 7), which would primarily affect abundances based on CELs, underestimating the real values; semi-ionized gas clumps, overestimating abundances based on RLs and underestimating those of CELs; chemical inhomogeneities with different physical conditions, affecting both estimates depending on each specific case and so on. It is even possible that the AD is the result of the sum of various phenomena affecting each nebula in a different degree. Using a set of deep spectra of Galactic H II regions, García-Rojas & Esteban (2007) found that the ADF is fairly constant around a factor 2, showing no trend with ionization degree, T_e or the effective temperature of the ionizing stars. They found that temperature fluctuations is the most likely explanation for the AD in H II regions.

In Table 9, we present the ADF obtained from O^+ , O^{2+} , Ne^{2+} and C^{2+} abundances determined from RLs and CELs for each component. The abundances based on CELs do not consider temperature fluctuations. In the case of C^{2+} , the value of the abundance from CELs have been taken from the UV observations reported by Walter et al. (1992). We have considered the mean value of their positions number 5 and 7, which are the nearest to our slit and give $12 + \log(\text{C}^{2+}/\text{H}^+) = 7.835$. We do not estimate the $\text{ADF}(\text{C}^{2+})$ for the high-velocity component since the UV CELs values can only be compared with the nebular component. We emphasize that the estimated value of t^2 comes from the comparison of different temperature diagnostics and the formalism described in Section 7. Therefore $t^2 > 0$, does not necessarily mean $\text{ADF} > 0$, unless the measured value of t^2 is compatible with this.

From Table 9, it is remarkable that the ADF is slightly different for each ion and higher in the high-velocity components. Comparing the values included in Table D15 and Table 8, we can see that using the value of t^2 adopted for each ionization zone of the nebular components, the O^{2+} abundances based on CELs become fairly consistent with those determined from RLs. In the case of the O^+ abundances, although the CELs abundances obtained with $t^2 > 0$ do not agree completely with those obtained from RLs, they become clearly more similar. Definitively, this is not the case for the Ne^{2+} abundances, in which values determined from CELs and RLs still

Table 8. Chemical abundances based on CELs derived within the paradigm of temperature inhomogeneities ($t^2 > 0$).

Ion	Cut 1	Cut 2		Cut 3		Cut 4	Combined cuts
	Nebula	HH 529 II	Nebula	HH 529 III	Nebula	Nebula	
O ⁺	8.18 ^{+0.10} _{-0.08}	7.65 ^{+0.20} _{-0.12}	8.14 ^{+0.12} _{-0.09}	7.74 ^{+0.34} _{-0.17}	8.05 ^{+0.13} _{-0.09}	8.12 ^{+0.13} _{-0.09}	8.05 ^{+0.11} _{-0.08}
O ²⁺	8.48 ^{+0.06} _{-0.05}	8.72 ^{+0.04} _{-0.03}	8.50 ^{+0.05} _{-0.04}	8.64 ^{+0.04} _{-0.03}	8.51 ± 0.04	8.52 ^{+0.05} _{-0.04}	8.53 ^{+0.05} _{-0.04}
N ⁺	7.18 ^{+0.05} _{-0.04}	6.36 ^{+0.11} _{-0.08}	7.17 ^{+0.07} _{-0.05}	6.59 ^{+0.18} _{-0.11}	7.09 ^{+0.07} _{-0.05}	7.16 ^{+0.07} _{-0.06}	7.07 ^{+0.06} _{-0.05}
Ne ²⁺	7.86 ^{+0.07} _{-0.06}	8.12 ± 0.04	7.89 ^{+0.06} _{-0.05}	7.99 ^{+0.05} _{-0.04}	7.91 ^{+0.05} _{-0.04}	7.94 ^{+0.06} _{-0.05}	7.93 ^{+0.06} _{-0.05}
S ⁺	5.75 ^{+0.07} _{-0.06}	5.04 ^{+0.12} _{-0.08}	5.75 ^{+0.07} _{-0.06}	5.30 ^{+0.19} _{-0.13}	5.70 ^{+0.08} _{-0.07}	5.77 ^{+0.08} _{-0.06}	5.66 ^{+0.07} _{-0.06}
S ²⁺	6.87 ^{+0.05} _{-0.04}	7.01 ^{+0.06} _{-0.05}	6.94 ^{+0.06} _{-0.05}	6.97 ^{+0.07} _{-0.06}	6.95 ^{+0.06} _{-0.05}	6.91 ± 0.05	6.94 ± 0.05
Cl ⁺	3.87 ± 0.05	3.09 ^{+0.16} _{-0.14}	3.86 ^{+0.06} _{-0.05}	<3.49	3.81 ^{+0.06} _{-0.05}	3.90 ^{+0.07} _{-0.06}	3.76 ^{+0.06} _{-0.05}
Cl ²⁺	5.00 ^{+0.07} _{-0.06}	5.15 ^{+0.09} _{-0.07}	5.06 ^{+0.08} _{-0.06}	5.15 ^{+0.11} _{-0.08}	5.09 ^{+0.08} _{-0.06}	5.08 ^{+0.08} _{-0.06}	5.07 ^{+0.07} _{-0.06}
Cl ³⁺	3.30 ± 0.06	3.71 ± 0.05	3.38 ± 0.04	3.50 ^{+0.11} _{-0.10}	3.43 ± 0.04	3.55 ^{+0.05} _{-0.04}	3.48 ^{+0.06} _{-0.05}
Ar ²⁺	6.42 ± 0.04	6.51 ± 0.03	6.42 ^{+0.04} _{-0.03}	6.46 ± 0.03	6.43 ± 0.03	6.40 ^{+0.04} _{-0.03}	6.43 ^{+0.04} _{-0.03}
Ar ³⁺	4.55 ^{+0.07} _{-0.06}	4.84 ^{+0.05} _{-0.04}	4.63 ^{+0.06} _{-0.05}	4.66 ^{+0.08} _{-0.07}	4.66 ^{+0.05} _{-0.04}	4.79 ^{+0.06} _{-0.05}	4.69 ^{+0.06} _{-0.05}
Fe ^{2+*}	5.93 ± 0.02	6.11 ± 0.05	5.97 ± 0.02	5.91 ± 0.05	5.94 ± 0.02	5.92 ± 0.03	5.96 ± 0.01
Fe ^{2+**}	5.75 ± 0.02	5.84 ± 0.06	5.81 ± 0.02	5.57 ± 0.06	5.75 ± 0.02	5.72 ± 0.03	5.76 ± 0.02
Fe ³⁺	5.99 ^{+0.16} _{-0.12}	6.59 ^{+0.12} _{-0.10}	6.00 ^{+0.12} _{-0.09}	<6.68	6.23 ^{+0.18} _{-0.16}	6.05 ^{+0.16} _{-0.13}	6.16 ^{+0.18} _{-0.15}
Ni ²⁺	4.52 ± 0.19	4.68 ± 0.09	4.51 ± 0.18	4.42 ^{+0.20} _{-0.13}	4.48 ± 0.16	4.51 ± 0.13	4.54 ± 0.11

* indicates that T_e (high) was used.

** indicates that T_e (low) was used.

do not agree even considering $t^2 > 0$. The results obtained for O²⁺ and O⁺ suggest that the temperature fluctuation paradigm may be capable of explaining the ADF, at least for these ions, the ones with the best abundance determinations based on RLs. Among different scenarios, the existence of H-deficient clumps has been advocated as a possible cause of the very high ADF values found in some PNe (e.g. Péquignot et al. 2002). Since the heating of ionized gas is mainly due by photoionization of H and He and the cooling by the emission of CELs of metallic ions, this scenario implies significant lower temperatures in the clumps (Péquignot et al. 2002). As we mentioned in Section 5.3.1, the T_e (O II) determined for the nebular component of cut 2 (which must be representative of the other nebular components) is consistent with T_e ([O III]) within the uncertainties, which rules out the aforementioned scenario in the nebular components analysed in this work. The situation seems to be different for the high-velocity components. Assuming $t^2 > 0$, the ionic abundances obtained from CELs do not increase enough to match the values obtained from RLs. For example, in the case of HH 529 II, considering the adopted value $t^2 = 0.021$, the ADF(O²⁺) is reduced from 0.29 to 0.11 but is not zero. Even if we consider the value of $t^2 = 0.025$ from Table D17, the ADF(O²⁺) would be 0.08. A similar situation is found in HH 529 III, where for $t^2 = 0.021$ the ADF(O²⁺) is 0.20 while considering $t^2 = 0.030$ the ADF(O²⁺) would be 0.12. Since we do not find evidence of higher temperature fluctuations than those previously commented, these results suggest the presence of another physical process apart (or in addition) to the classic description of temperature inhomogeneities to explain the ADF. A similar result was found by Mesa-Delgado et al. (2009) in the case of HH 202 S (see their Sec 5.5). For the high-velocity components, the presence of a H-deficient material can not be discarded as we will discuss in Section 9.3.

9 TOTAL ABUNDANCES

We have to use ionization correction factors (ICFs) to estimate the contribution of unseen ions to the total abundance of some elements. Following the detailed analysis of Arellano-Córdova et al. (2020), we have used the ICF schemes for C, N, Ne and Ar adopted by those authors, which are shown in Table 10. In the case of S, He, Fe and Ni, we use the ICFs from Stasińska (1978), Kunth & Sargent (1983), Rodríguez & Rubin (2005) and Delgado-Inglada et al. (2016), respectively. Results of total abundances based on CELs are presented in Table 11 and in Table 12, for the cases of $t^2 = 0$ and $t^2 > 0$, respectively. Total abundances based on RLs are presented in Table 13. In this case, we do not expect significant changes in the total abundances within the temperature fluctuation paradigm due to the low dependence of RLs on temperature. The ICFs are generally based on the degree of ionization indicated by the abundance ratio of O ions. For consistency, in the case of abundances based on CELs, we use the degree of ionization determined also with CELs. An analogous procedure is applied for abundances determined from RLs.

9.1 Total abundances with CELs

9.1.1 Oxygen, Chlorine and Argon

All ionization states of O and Cl expected in the nebula show emission lines in our spectra and the calculation of their total abundances do not require an ICF. In HH 529 III, we could only estimate an upper limit for Cl⁺. However, even assuming this upper limit, the contribution of this ion to the total Cl abundance is negligible. In the case of Ar, the ICF model of Izotov et al. (2006) indicates that the contribution of Ar^{+/H⁺} to the total Ar abundance is also negligible in all the analysed components. Thus, we will consider Ar/H = Ar^{2+/H⁺} + Ar^{3+/H⁺}. The Cl/O and Ar/O ratios are consistent with the solar values recommended by Lodders (2019) within the uncertainties, whether we use abundances determined from CELs

Table 9. Abundance discrepancy factor (ADF), defined in Eq. 18, for different ions in the components of each cut.

Cut	Component	ADF(O ⁺)	ADF(O ²⁺)	ADF(Ne ²⁺)	ADF(C ²⁺) [*]
1	Nebular	0.46 ± 0.14	0.15 ± 0.07	-	0.51 ± 0.03
2	HH 529 II	<0.55	0.29 ± 0.10	0.79 ± 0.09	-
2	Nebular	0.42 ± 0.12	0.17 ± 0.05	0.37 ± 0.04	0.52 ± 0.03
3	HH 529 III	<0.44	0.36 ± 0.11	-	-
3	Nebular	0.52 ± 0.14	0.17 ± 0.06	0.31 ± 0.15	0.51 ± 0.03
4	Nebular	0.46 ± 0.14	0.17 ± 0.06	-	0.50 ± 0.02
Combined cuts		0.44 ± 0.12	0.21 ± 0.05	-	0.54 ± 0.03

* We adopt $12 + \log(C^{2+}/H^+) = 7.835$ from UV CELs considering the slit positions 5 and 7 of [Walter et al. \(1992\)](#).

Table 10. ICFs used to estimate the abundance of unseen ions.

Element	ICF Reference
He	Kunth & Sargent (1983)
C	Berg et al. (2019)
N	Peimbert & Costero (1969)
Ne	Peimbert & Costero (1969)
S	Stasińska (1978)
Ar	Izotov et al. (2006)
Fe	Rodríguez & Rubin (2005)
Ni	Delgado-Ingla et al. (2016)

considering $t^2 = 0$ or $t^2 > 0$. In addition, there are no appreciable differences between the Cl/O and Ar/O ratios determined in the nebular and the high-velocity components.

9.1.2 Nitrogen, Neon and Sulfur

The total abundances of N, Ne and S depend strongly on the adopted ICF values. The schemes used for these elements are indicated in Table 10. The calculation of total N may be somewhat uncertain because of the high degree of ionization of the Orion Nebula and the high-velocity components and since N⁺ is the only observable ion. The estimated fraction N/N⁺ can reach values between 4 and 16 for the nebular and the high-velocity components, respectively. Using $t^2 = 0$ for the nebular components, the average value of log(N/O) is -0.86 ± 0.02 , in very good agreement with the suggested solar value of -0.88 ± 0.14 ([Lodders 2019](#)). However, in the case of $t^2 > 0$, the corresponding log(N/O) = -0.98 ± 0.02 becomes lower for the nebular components, although still consistent within the relatively large uncertainties of the solar abundance ratio. In the high-velocity components, we obtain log(N/O) = $-1.17^{+0.18}_{-0.11}$ and log(N/O) = $-1.08^{+0.41}_{-0.18}$ for HH 529 II and HH 529 III, respectively with $t^2 = 0$. Considering the scenario of temperature fluctuations, these values are log(N/O) = $-1.30^{+0.38}_{-0.17}$ and log(N/O) = $-1.24^{+0.72}_{-0.28}$, respectively. These results suggest that the ICF values are rather uncertain at the high degree of ionization of the high-velocity components.

[Rubin et al. \(2011\)](#) determined the Ne/H ratio of the Orion Nebula from FIR spectra taken with the *Spitzer Space Telescope*, that permitted to detect fine-structure [Ne II] and [Ne III] lines, avoiding the use of ICFs. They obtain $12 + \log(\text{Ne}/\text{H}) = 8.01 \pm 0.01$, which is consistent with the Ne/H values we obtained for the nebular component assuming $t^2 > 0$. It is important to remark that the intensity of FIR CELs has a very small dependence on T_e . Therefore, the agreement between the Ne/H ratios obtained from FIR CELs and optical ones assuming $t^2 > 0$ supports the temperature fluctuations paradigm for describing the spectral properties of the nebula.

The Ne/O and S/O ratios are rather similar in the nebular and high-velocity components. The average values of log(Ne/O) are -0.64 ± 0.02 and -0.61 ± 0.02 for $t^2 = 0$ and $t^2 > 0$, respectively,

which are consistent with the solar value of -0.58 ± 0.12 ([Lodders 2019](#)) within the uncertainties. In the case of S/O, the average values of log(S/O) for $t^2 = 0$ and $t^2 > 0$ are -1.50 ± 0.05 and -1.63 ± 0.05 , respectively, while the solar value is -1.58 ± 0.08 ([Lodders 2019](#)).

9.1.3 Nickel and Iron

Ni/H abundances are estimated using the ICF scheme derived by [Delgado-Ingla et al. \(2016\)](#) and are presented in Table 11 and Table 12 for $t^2 = 0$ and $t^2 > 0$, respectively. The estimation of this abundance is rather uncertain as discussed in Section C.

In the case of Fe, considering the absence of He II lines in our spectra, we do not expect to have Fe⁴⁺ in the nebula and therefore $\text{Fe}/\text{H} = \text{Fe}^+/H^+ + \text{Fe}^{2+}/H^+ + \text{Fe}^{3+}/H^+$. We have determined the abundance of Fe²⁺ and Fe³⁺ in all the components of each cut except in HH 529 III, where we could only estimate an upper limit to Fe^{3+}/H⁺. In the high-velocity components, the absence of usually relatively intense [Fe II] lines as $\lambda\lambda 4287, 5158$ and 5262 , together with the high ionization degree of the gas, indicates a negligible contribution of Fe⁺ to the total abundance. Thus, in these cases $\text{Fe}/\text{H} = \text{Fe}^{2+}/H^+ + \text{Fe}^{3+}/H^+$. In the nebular components, although a large number of [Fe II] lines have been detected, their emission is mainly produced by fluorescence ([Rodríguez 1999; Verner et al. 2000](#)) and most of the observed lines will not provide reliable estimates of Fe⁺ abundance. Unfortunately, [Fe II] $\lambda 8617$, a line almost insensitive to fluorescence ([Lucy 1995; Baldwin et al. 1996](#)) can not be observed due to the physical gap of the CCDs in the Red Arm of UVES. However, previous studies with direct estimations of Fe⁺ in the Orion Nebula as [Rodríguez \(2002\)](#) or [Mesa-Delgado et al. \(2009\)](#), obtain Fe⁺/Fe²⁺ ratios between 0.05 and 0.27. Considering the approximation $\text{Fe}/\text{H} = \text{Fe}^{2+}/H^+ + \text{Fe}^{3+}/H^+$, the neglected Fe⁺/H⁺ ratio would contribute to Fe/H up to 0.06 dex in the worst case (calculating Fe^{2+}/H^+ with T_e (high) and assuming $\text{Fe}^+/\text{Fe}^{2+} = 0.27$). This maximum contribution is within the range of uncertainties associated with the sum of Fe²⁺ and Fe³⁺ abundances and therefore, it seems reasonable to consider $\text{Fe}/\text{H} \approx \text{Fe}^{2+}/H^+ + \text{Fe}^{3+}/H^+$ for the nebular component as well.}

[Rodríguez & Rubin \(2005\)](#) proposed two ICFs for Fe, one derived from photoionization models and other based on observations with detection of [Fe III] and [Fe IV] lines. The values of Fe/H obtained using both ICFs are discrepant, perhaps due to errors in the atomic data of the ions involved. The true total Fe abundance is expected to be in between the values obtained from both ICFs ([Rodríguez & Rubin 2005; Delgado-Ingla et al. 2014](#)). We use the aforementioned ICFs only for HH 529 III and we give its Fe/H ratio as the interval of values obtained from both ICFs, as it is shown in Table 11 and Table 12.

In HH 529 II, the abundances of Fe/H and Fe/O are higher than in the nebular components independently of whether the temperature T_e (low) or T_e (high) is considered to derive Fe^{2+}/H^+ . The

same behavior is observed in HH 529 III for $t^2 = 0$, although the uncertainty in Fe/H do not allow us to be conclusive in the case of $t^2 > 0$. However, as is discussed in Section 5.2, the representative temperature to derive $\text{Fe}^{2+}/\text{H}^+$ in HH 529 II and HH 529 III is likely to be $T_e(\text{high})$ while in the nebular components is $T_e(\text{low})$.

Considering the discussion above, the average $\log(\text{Fe}/\text{O})$ value in the nebular components is -2.53 ± 0.02 while for HH 529 II it is -2.14 ± 0.08 , both values computed assuming $t^2 = 0$. This represents an increase of the gaseous Fe abundance by a factor of 2.45 in HH 529 II. The same increase is observed when considering $t^2 > 0$. For HH 529 III the increase is between 1.78 and 4.37. Taking the solar value of $\log(\text{Fe}/\text{O}) = -1.28 \pm 0.08$ recommended by Lammers (2019), we find that only 6% of the total Fe is in gaseous phase in the nebular component, while this fraction increases to 14% in HH 529 II and between 10% and 25% in HH 529 III. In the case of HH 202 S, Mesa-Delgado et al. (2009) found that the gaseous phase fraction is around 44%. These results are consistent with theoretical studies predicting that fast shocks are effective at destroying dust grains (see Jones et al. 1994; Mouri & Taniguchi 2000, and references therein). However, this also indicate that most of the Fe is still depleted into dust grains in the shocks associated with the HH objects. Another evidence of surviving dust is the detection of thermal emission of dust at $11.7 \mu\text{m}$ coincident with HH 529 II and III as well as HH 202 S (Smith et al. 2005). A key factor is exploring correlations between the dust depletion factor of Fe and physical properties of the HH objects, such as their velocity or distance to the ionizing source, among others. The 3D velocity of HH 202 S is $\sim 89 \text{ km s}^{-1}$ (see Sec 5.4 of Mesa-Delgado et al. (2009)) while for HH 529 it is $\sim 65 \text{ km s}^{-1}$ (see Section 12), indicating that the fraction of gaseous Fe in the shock front seems to depend on the velocity of the HH. In any case, we need to study additional photoionized HH objects with different velocities to confirm such presumed correlation.

9.2 Total abundances with RLs

9.2.1 Helium

Considering the absence of an ionization front in HH 529 II and HH 529 III because of the non-detection of emission lines of neutral elements in their spectra, it is likely that the He^0/H^+ ratio should be negligible in the high-velocity components and, therefore, we can assume $\text{He}/\text{H} = \text{He}^+/\text{H}^+$. In the nebular components, we estimate the fraction of neutral helium within the ionized zone making use of the ICF scheme by Kunth & Sargent (1983), obtaining that the He^0/He fraction is approximately 10%. This value is consistent with the other ICF schemes tested by Méndez-Delgado et al. (2020) for the Orion Nebula. In Table 13, we can see that the He/H ratios obtained for all the cuts are in complete agreement.

9.2.2 Oxygen

The total O abundances based on RLs are determined directly from $\text{O}/\text{H} = \text{O}^+/\text{H}^+ + \text{O}^{2+}/\text{H}^+$. In the high-velocity components, the absence of OI RLs indicate a small contribution of O^+/H^+ to the O/H ratio. In Section 6.2.3 we estimate an upper limit to this ionic abundance in HH 529 II and HH 529 III, which can contribute up to 0.05 dex to the total O/H ratio. Thus, for these high-velocity components the O abundance is assumed to be equal to O^{2+}/H^+ , considering the possible contribution of O^+/H^+ of the order of the error of the O/H ratio.

9.2.3 Carbon and Neon

In the case of the high-velocity components, due to the high degree of ionization estimated from the ionic O abundances based on RLs, we expect to have small or negligible contributions of C^+/H^+ and Ne^+/H^+ to the total C/H and Ne/H abundances, respectively. In these cases we have assumed ICF=1. For the nebular components, we use the ICF from Peimbert & Costero (1969) for Ne, as in Section 9.1.2, but using the ionic abundances of O based on RLs. The resulting $\log(\text{Ne}/\text{O})$ value based on RLs is -0.44 ± 0.03 and -0.23 ± 0.10 for the nebular components and HH 529 II respectively, both values are larger than the $\log(\text{Ne}/\text{O})$ determined from CELs for the same components (see Section 9.1.2). In the nebular components, $\log(\text{Ne}/\text{O})$ values both based on RLs and CELs are in agreement with the solar value of -0.58 ± 0.12 (Lammers 2019) within the error. However, for HH 529 II, the Ne/O ratio is significantly larger than the solar value indicating that the $\text{Ne}^{2+}/\text{H}^+$ ratio may be overestimated for this component.

We use the ICF proposed by Berg et al. (2019) to estimate the contribution of C^+/H^+ to the total C/H abundance of the nebular components. It is important to note that this ICF may not be completely adequate for the Orion Nebula since it has been optimized for low-metallicity objects (up to $12+\log(\text{O}/\text{H})=8.0$). Despite this, the results obtained with this scheme are more consistent with the expected solar values, compared to those obtained with other available ICF schemes, as has been discussed by Arellano-Córdova et al. (2020). For comparison, in Table 13, we present the C/H ratio obtained using the ICF proposed by Amayo et al. (in prep, private communication), whose scheme is optimized for a wider range of metallicities, including the solar one. We can see in Table 13 that the values obtained with both ICFs are consistent within the uncertainties. The average $\log(\text{C}/\text{O})$ value for the nebular components is -0.20 ± 0.02 using the ICF of Berg et al. (2019) and -0.26 ± 0.02 using the scheme of Amayo et al. (in prep). This last value is more consistent with the recommended solar value of -0.26 ± 0.09 by Lammers (2019). The $\log(\text{C}/\text{O})$ value for HH 529 II is -0.37 ± 0.08 while for HH 529 III is -0.28 ± 0.12 .

9.3 A slight higher metallicity in the high-velocity components?

An interesting result of our analysis is that the metal abundances are higher in the high-velocity components, HH 529 II and HH 529 III, than in the nebular ones. In the case of the O abundance, that difference can reach up to 0.14 dex, regardless if abundances are calculated with CELs or RLs. Mesa-Delgado et al. (2009) estimated that 0.12 ± 0.03 dex of $\log(\text{O}/\text{H})$ is depleted into dust grains in the Orion Nebula. In principle one may explain the 0.14 dex increase of O/H in the HH objects as produced by dust destruction, and that all the O locked in grains has been released to the gas phase. Nevertheless, the Ar/O, Ne/O, S/O and Cl/O ratios remain almost the same in all components. Since Ar and Ne are noble gases, they can not be depleted into dust grains and, therefore, lower abundance ratios would be expected if dust destruction is increasing the gaseous O abundance. In addition to this, considering that the O trapped onto dust grains is in olivine $(\text{Mg}, \text{Fe})_2\text{SiO}_4$, pyroxene $(\text{Mg}, \text{Fe})\text{SiO}_3$ or oxides like Fe_2O_3 , then the gaseous O must grow in proportion to the release of elements like Fe to the gas phase. Considering this, Mesa-Delgado et al. (2009) estimated that 0.06 dex of $\log(\text{O}/\text{H})$ can be attributed to dust destruction in HH 202 S. As we mention in Section 9.1.3, the proportion of gaseous Fe present in HH 529 II and HH 529 III is lower than in HH 202 S, and therefore, the

Table 11. Total abundances based on CELs with $t^2 = 0$.

Element	Cut 1		Cut 2		Cut 3		Cut 4		Combined cuts
	Nebula	HH 529 II	Nebula	HH 529 III	Nebula	HH 529 III	Nebula	HH 529 III	
O	8.45 ± 0.02	8.57 ± 0.03	8.46 ± 0.03	8.53 ± 0.03	8.45 ± 0.03	8.47 ± 0.03	8.46 ± 0.03	8.46 ± 0.03	
N	7.57 ± 0.04	7.40 ^{+0.16} _{-0.10}	7.62 ^{+0.07} _{-0.05}	7.45 ^{+0.37} _{-0.17}	7.60 ^{+0.08} _{-0.07}	7.64 ^{+0.08} _{-0.06}	7.60 ^{+0.06} _{-0.05}	7.60 ^{+0.06} _{-0.05}	
Ne	7.81 ± 0.04	7.94 ± 0.03	7.82 ± 0.04	7.84 ± 0.04	7.83 ± 0.03	7.86 ± 0.04	7.82 ± 0.04	7.82 ± 0.04	
S	6.89 ± 0.04	7.18 ^{+0.07} _{-0.06}	6.96 ^{+0.08} _{-0.09}	7.09 ^{+0.11} _{-0.07}	6.98 ± 0.05	6.94 ± 0.05	6.98 ± 0.04	6.98 ± 0.04	
Cl	4.92 ± 0.06	5.03 ± 0.05	4.97 ± 0.06	5.05 ± 0.08	4.99 ± 0.06	4.99 ± 0.06	4.97 ± 0.05	4.97 ± 0.05	
Ar	6.32 ± 0.03	6.40 ± 0.02	6.32 ± 0.03	6.37 ± 0.03	6.34 ± 0.02	6.30 ± 0.03	6.33 ± 0.03	6.33 ± 0.03	
Fe*	6.03 ± 0.06	6.42 ± 0.07	6.07 ± 0.04	6.24–6.63	6.06 ± 0.05	6.05 ± 0.06	6.08 ± 0.05	6.08 ± 0.05	
Fe**	5.91 ± 0.07	6.34 ± 0.08	5.94 ± 0.05	5.90–6.28	5.94 ± 0.07	5.92 ± 0.08	5.95 ± 0.07	5.95 ± 0.07	
Ni	4.59 ± 0.14	5.12 ^{+0.15} _{-0.10}	4.58 ^{+0.18} _{-0.17}	4.75 ^{+0.29} _{-0.17}	4.60 ^{+0.17} _{-0.16}	4.62 ^{+0.13} _{-0.12}	4.67 ^{+0.11} _{-0.10}	4.67 ^{+0.11} _{-0.10}	

* indicates that T_e (high) was used to compute $\text{Fe}^{++}/\text{H}^+$.** indicates that T_e (low) was used to compute $\text{Fe}^{++}/\text{H}^+$.**Table 12.** Total abundances based on CELs with $t^2 > 0$.

Element	Cut 1		Cut 2		Cut 3		Cut 4		Combined cuts
	Nebula	HH 529 II	Nebula	HH 529 III	Nebula	HH 529 III	Nebula	HH 529 III	
O	8.66 ± 0.05	8.76 ± 0.04	8.66 ± 0.05	8.70 ± 0.05	8.64 ± 0.04	8.67 ± 0.05	8.65 ± 0.05	8.65 ± 0.05	
N	7.66 ^{+0.11} _{-0.08}	7.45 ^{+0.35} _{-0.16}	7.69 ^{+0.14} _{-0.10}	7.46 ^{+0.63} _{-0.28}	7.68 ^{+0.16} _{-0.10}	7.71 ^{+0.15} _{-0.10}	7.68 ^{+0.13} _{-0.09}	7.68 ^{+0.13} _{-0.09}	
Ne	8.04 ± 0.08	8.16 ± 0.04	8.05 ± 0.07	8.04 ± 0.06	8.04 ± 0.06	8.08 ^{+0.08} _{-0.07}	8.05 ^{+0.07} _{-0.06}	8.05 ^{+0.07} _{-0.06}	
S	6.95 ± 0.05	7.24 ^{+0.10} _{-0.07}	7.03 ± 0.06	7.15 ^{+0.14} _{-0.09}	7.05 ^{+0.07} _{-0.06}	7.01 ^{+0.06} _{-0.05}	7.05 ^{+0.06} _{-0.05}	7.05 ^{+0.06} _{-0.05}	
Cl	5.04 ± 0.06	5.17 ± 0.09	5.10 ± 0.07	5.17 ± 0.11	5.12 ± 0.07	5.12 ± 0.07	5.10 ± 0.07	5.10 ± 0.07	
Ar	6.44 ± 0.04	6.52 ± 0.03	6.43 ± 0.04	6.47 ± 0.04	6.44 ± 0.03	6.42 ± 0.04	6.44 ± 0.04	6.44 ± 0.04	
Fe*	6.26 ± 0.09	6.71 ± 0.09	6.29 ± 0.06	6.38–6.72	6.41 ± 0.12	6.29 ± 0.09	6.37 ± 0.11	6.37 ± 0.11	
Fe**	6.19 ± 0.10	6.66 ± 0.10	6.22 ± 0.07	6.04–6.37	6.35 ± 0.14	6.22 ± 0.11	6.31 ± 0.13	6.31 ± 0.13	
Ni	4.70 ± 0.19	5.22 ^{+0.26} _{-0.13}	4.71 ^{+0.19} _{-0.18}	4.81 ^{+0.42} _{-0.28}	4.71 ^{+0.18} _{-0.16}	4.72 ^{+0.15} _{-0.13}	4.78 ^{+0.13} _{-0.12}	4.78 ^{+0.13} _{-0.12}	

* indicates that T_e (high) was used to compute $\text{Fe}^{++}/\text{H}^+$.** indicates that T_e (low) was used to compute $\text{Fe}^{++}/\text{H}^+$.**Table 13.** Total abundances based on RLs.

Element	Cut 1		Cut 2		Cut 3		Cut 4		Combined cuts
	Nebula	HH 529 II	Nebula	HH 529 III	Nebula	HH 529 III	Nebula	HH 529 III	
O	8.71 ± 0.03	8.83 ± 0.07	8.70 ± 0.03	8.84 ± 0.09	8.71 ± 0.03	8.72 ± 0.03	8.73 ± 0.03	8.73 ± 0.03	
He	10.94 ± 0.02	10.95 ± 0.03	10.94 ± 0.01	10.95 ± 0.03	10.94 ± 0.02	10.95 ± 0.02	10.94 ± 0.02	10.94 ± 0.02	
C*	8.56 ± 0.04		8.52 ± 0.03		8.52 ± 0.04		8.51 ^{+0.04} _{-0.03}	8.51 ^{+0.04} _{-0.03}	
C**	8.48 ^{+0.08} _{-0.07}	8.46 ± 0.02	8.45 ± 0.05	8.56 ± 0.03	8.45 ^{+0.07} _{-0.06}	8.44 ± 0.06	8.45 ^{+0.06} _{-0.05}	8.45 ^{+0.06} _{-0.05}	
Ne	-	8.60 ± 0.06	8.26 ± 0.04	-	8.23 ± 0.15	-	-	-	

* Total abundances of the nebular components derived with the ICF of [Berg et al. \(2019\)](#).

** Total abundances of the nebular components derived with the ICF of Amayo et al. (in prep.).

expected increase of $\log(\text{O/H})$ in the two bow shocks of HH 529 should be consequently less than 0.06 dex.

BMB06 also report a higher O abundance in HH 529 with respect to the nebular one. The difference they obtained was slightly larger than ours, of around 0.2 dex. This value is confirmed in the later reanalysis of BMB06 data carried out by [Simón-Díaz & Stasińska \(2011\)](#). However, as we discussed in Section 3, part of the larger difference found by BMB06 with respect to our O/H ratio may be due to their underestimation of $I(\text{H}\beta)$, as we illustrate in Table D1.

Assuming that the abundance difference between the kinematical components is real, one possible explanation is that the bulk

of the material of the HH objects comes from H-deficient material expelled by the source of the gas flow. As we mentioned in Section 8, an H-deficient ionized gas should be colder than one with normal chemical composition but this is not observed (see Table 4). This may be because the possible over-metallicity is actually small, which might not significantly alter the temperature. The origin of the H-deficient material may be in the evaporation of protoplanetary discs around newly formed stars ([Yuan et al. 2011](#)), a probable scenario for the origin of HH 529. In this sense, it is a well-known fact that HH 529 is a source of IR emission ([Robberto et al. 2005](#); [Smith et al. 2005](#)), emitting strongly at $10\mu\text{m}$ and $11.7\mu\text{m}$. [Smith et al. \(2005\)](#) show that the $11.7\mu\text{m}$ radiation arises from thermal

dust emission and is visible both behind the leading bow shock and within the jet body of HH 529 (see their Fig. 7). After analysing different scenarios, Smith et al. (2005) conclude that the dust may be entrained from the origin of the jet, which implies that at least part of the ejected material comes from a radius larger than the sublimation radius in the accretion disc of the source. Some of this material may originally come from H-deficient solids. However, the mechanism of expulsion of this H-deficient material and its interaction with the ambient gas requires a deeper analysis of solid body destruction in new formed stars, an idea further explored in planetary nebulae (Henney & Stasińska 2010). Tsamis et al. (2011) obtained deep optical integral field spectroscopy of the LV2 proplyd in The Orion Nebula, determining, for the first time, the chemical composition in this kind of objects. They find that the abundances of O, C and Ne in the ionized gas of the proplyd are between 0.11 and 0.52 dex higher than in the rest of the nebula. This result is somehow qualitatively consistent with the overmetallicity we find for the bow-shocks of HH 529, supporting the possibility that the entrained material of the HH objects may come from the source of the gas flow. However, the abundance pattern found for LV2 is not confirmed in the proplyd HST 10, where the chemical composition is not substantially different from the nebular gas (Tsamis et al. 2013).

Finally, we should keep in mind that the apparently larger metallicity of the HH objects may be simply produced by the atomic data used for the analysis. As Juan de Dios & Rodríguez (2017) have discussed, uncertainties in the atomic data may be more important for high-density objects (densities above 10^4 cm^{-3}) because there is less possibility to check them observationally. Subsequent analysis of new photoionized HH objects, whose analysis we are carrying out, can shed further light on this issue.

10 KINEMATICAL ANALYSIS FROM UVES DATA

We calculate the radial velocity of each line in the heliocentric framework by comparing its observed wavelength (after applying the radial velocity correction) with its theoretical wavelength in air. All the theoretical values have been taken from the Atomic Line List v2.05b21 (Van Hoof 2018). Wavelengths from this compilation list are mainly calculated from the theoretical energy difference between the levels connected by the transition. The exception are the hydrogenic lines, which include a weighted average of all the fine structure components.

We detect some evident inaccuracies in the theoretical wavelengths of [Cl III], [Cl IV] and [Ne III] in the Atomic Line List v2.05b21. This conclusion is based on the discrepant velocities that those lines show with respect to the rest of lines in the high-velocity components, that show fairly similar velocities independently of the ionization state of the ions and elements (see Section 10.1). For example, in the case of [Ne III] $\lambda\lambda 3869, 3967$, the Atomic Line List v2.05b21 gives $\lambda\lambda 3869.07 \pm 0.09$ and 3967.79 ± 0.10 based on the works of Persson et al. (1991) and Feuchtgruber et al. (1997). These wavelengths give velocities about -20 km s^{-1} displaced with respect to the mean velocity obtained for the rest of the lines. In this case, we decided to adopt the wavelengths $\lambda\lambda 3868.75$ and 3967.46 obtained by Bowen (1955) from high-resolution spectroscopy of nebulae. The [Cl III] and [Cl IV] lines show a similar problem; in this case, we adopt the reference wavelengths used by Esteban et al. (2004) that give consistent velocities. The wavelengths adopted for [S III] lines deserve special attention. The values given by the Atomic Line List v2.05b21 are $\lambda\lambda 6312.1 \pm 0.36$, 8829.4 ± 0.49 , 9068.6 ± 0.52 and

9530.6 ± 0.57 , taken from the work by Kaufman & Martin (1993). There is a small (but noticeable at our spectral resolution) discrepancy in the velocity obtained for [S III] $\lambda 6312$ and the rest of the lines of about 10 km s^{-1} . Assuming the velocities measured for the HI lines of HH 529 II, our best estimation of the rest wavelengths of the observed [S III] lines are: $\lambda\lambda 6312.07 \pm 0.01$, 8829.70 ± 0.01 , 9068.93 ± 0.04 and 9530.98 ± 0.01 .

10.1 Radial velocity structure

In Table D18, we present the average velocity and full width at half maximum (FWHM) of each ion observed in the nebular component of cut 2 and in HH 529 II and III. The behaviour of the nebular component of cut 2 is representative of what is observed in the nebular components of the other cuts. In each column, we include in parentheses the number of lines of each kind whose values have been averaged. In this analysis, we discard lines with known blends and those affected by ghosts or by telluric emissions/absorptions. For O I, O II, C II and Ne II lines, we include only those used in Section 6.2 for abundance determinations, which are the lines that are assumed to be produced by pure recombination and are most probably not affected by fluorescence. In the special case of [S III] lines we consider only the $\lambda 6312$ line, due to the aforementioned evident inaccuracies in the theoretical wavelengths of the rest of the [S III] lines. Fig. 13 shows the heliocentric velocity as a function of ionization potential relation for the data collected in Table D18.

From the upper left panel of Fig. 13, it is clear that the nebular component presents a pattern consistent with the ‘‘blister’’ model for the Huygens Region of the Orion Nebula (O’Dell 2001; Ferland 2001; O’Dell et al. 2020, and references therein). The basic idea is that a layer of gas of the Orion Molecular Cloud (OMC) facing the direction towards the Sun is ionized by θ^1 Ori C, which is located in the foreground of OMC. As the gas gets ionized, it is accelerated towards the observer. Velocities of [O I], [C I], and [N I] are similar to the average velocity of the molecules in the OMC of $\sim 28 \text{ km s}^{-1}$ (Goudis 1982; O’Dell 2018, and references therein), then a rapid drop in the observed velocity (which means an increase in velocity compared to the OMC’s systemic velocity) of the ions whose ionization potential are between 6.77 and 13.6 eV is observed as well as a constant velocity after 13.6 eV. This behaviour has been observed in previous works (Kaler 1967; Fehrenbach 1977; O’Dell & Wen 1992; Esteban & Peimbert 1999).

In the lower panels of Fig. 13, we present the observed radial velocity of the ions as a function of their ionization potential for the high-velocity components: HH 529 II (lower left panel) and HH 529 III (lower right panel). Contrary to what the nebular components show, all the ions of the high-velocity components show a fairly constant radial velocity, independently of their ionization potential. Moreover, the high-velocity components do not show emission lines of neutral ions. These features are consistent with the scenario of a fully ionized slab of gas moving at a different velocity with respect to the rest of the nebular gas.

In the upper right panel of Fig. 13, we present the difference between the radial velocity pattern of the nebular component and HH 529 II (the subtraction of the upper and lower left panels of Fig. 13) rescaled using the average radial velocity of 51 HI lines in HH 529 II, whose rest-frame reference wavelengths λ_0 are the best determined among all the ions. Doing that subtraction, we can see that the dispersion of the data points represented initially in the upper left panel decreases substantially. This fact indicates that the dispersion is not due to errors associated with the determination of the wavelength of the lines or to a complex velocity structure,

but to inaccuracies in the adopted rest-frame reference wavelengths or possibly in the wavelength calibration. By eliminating the aforementioned dispersion, we can demonstrate that the acceleration of the gas in the Orion Nebula is constant for ionization potential between 6.77 and 13.6 eV, becoming zero for energies above, reaching a constant velocity of $16.4 \pm 0.8 \text{ km s}^{-1}$.

There is a difference of $5.18 \pm 1.25 \text{ km s}^{-1}$ between the radial velocities of HH 529 II and III. This is due to the presence of unresolved lower velocity components in HH 529 III, as it is shown in Fig. 14, which also contribute to increase the dispersion in the radial velocity structure of this component.

The radial velocities of the selected O I, O II and Ne II lines are practically the same as those of [O II], [O III] and [Ne III] CELs, respectively, in the nebular component. This reinforces the assumption that they are produced by pure recombination. For example, let's consider the O I RLs from multiplet 1, which come from quintuplet levels. If these lines were produced by fluorescence, they would be emitted in neutral and partially ionized zones of the nebula and should show a radial velocity similar to the systematic one of the OMC. In fact, O I lines from transitions between triplet levels (such as multiplet 4 $\lambda\lambda 8446.25, 8446.36, 8446.76$) are displaced around $\sim 10 \text{ km s}^{-1}$ with respect to the velocity of the aforementioned multiplet 1, clearly indicating the different nature of both multiplets, with the lines of multiplet 4 originating in starlight excitation (Grandi 1975b).

10.2 Electron temperature from thermal broadening of the line profiles

The observed line widths are the result of several physical processes. Apart from the instrumental width, σ_{ins} , the main contributors are the thermal width, σ_{th} , the fine structure broadening, σ_{fs} and the non-thermal contribution, σ_{nt} , which includes effects such as turbulence and any other additional broadening process. Following García-Díaz et al. (2008, hereinafter GHLD08, see their equation 2), we use Eq. (19) to express the relationship commented above.

$$\sigma_{\text{obs}}^2 = \sigma_{\text{th}}^2 + \sigma_{\text{fs}}^2 + \sigma_{\text{ins}}^2 + \sigma_{\text{nt}}^2. \quad (19)$$

The thermal contribution of Eq. (19) is the Doppler broadening and depends linearly on the temperature, $\sigma_{\text{th}}^2 = 82.5 T_4 / A (\text{km s}^{-1})^2$, where A is the atomic weight of the emitting ion and $T_4 = T_e / 10^4$ (GHLD08).

In principle, using Eq. (19) we can estimate T_e from the subtraction of the observed widths of H I and [O III] lines. The instrumental width affects the same for both kinds of lines and should be cancelled in the subtraction. GHLD08 estimated σ_{fs}^2 (H I) = $10.233 (\text{km s}^{-1})^2$, finding that σ_{fs}^2 ([O III]) is negligible. On the other hand, σ_{nt}^2 (H I) is not strictly equal to σ_{nt}^2 ([O III]), since the nebular volume occupied by both ions is different. GHLD08 define f as the fraction of the volume of H^+ occupied by O^{2+} and $(1-f)$ the fraction filled by O^+ and other ions with lower degree of ionization, as N^+ . We assume the average value $\langle f \rangle = 0.76$ estimated by GHLD08 for the Orion Nebula. Using equations 7 to 10 from GHLD08, we obtain $T_e = 8340 \pm 410 \text{ K}$ for the nebular component. In the case of the high-velocity components, we assume $f = 1.0$, obtaining $T_e = 8670 \pm 50 \text{ K}$ and $T_e = 10470 \pm 790 \text{ K}$ for HH 529 II and HH 529 III, respectively.

The resulting T_e values in the nebular component of cut 2 and HH 529 II are in remarkably good agreement with T_e ([O III]) from

CEL ratios as shown in Table 4. In the case of HH 529 III, the large difference between the values obtained from both methods may be due to the contamination by several unresolved velocity components, as it is shown in Fig. 14 and discussed in Section 11, that broadens the lines, providing overestimated temperatures.

11 PROPER MOTIONS OF HH 529 II AND III

The plane-of-sky motions of the bow shocks in HH 529 have been previously reported in Table 3 of O'Dell & Henney (2008) and in sec 3.3.1.3 of O'Dell et al. (2015). However, the reported tangential velocities are very disparate, so we have re-measured the proper motions, using HST imaging over 20 years as described in Section 2. The 1995 and 2015 images were aligned to the 2005 ACS image using Astrodrizzle⁵ and rebinned to the ACS pixel scale of 0.05 arcsec. The 2005 image itself has been aligned to the absolute astrometric reference of 2MASS, as painstakingly described in sec 3.3 of Robberto et al. (2013). Proper motions are estimated for the two intervals, 1995–2005 and 2005–2015, using the Fourier Local Correlation Tracking (FLCT) method (Welsch et al. 2004; Fisher & Welsch 2008)⁶ with a kernel width of 10 pixels (0.5 arcsec). For an assumed distance of 417 pc, a shift of 1 pixel in 10 years corresponds to approximately 10 km s^{-1} . A potential disadvantage of using the ACS data in this study is that the F658N ACS filter is relatively broad and includes both $\text{H}\alpha \lambda 6563$ and $[\text{N II}] \lambda 6583$, whereas the WFPC2 and WFC3 F656N filters are narrower and more effectively isolate $\lambda 6563$. Ionization gradients in the nebula can therefore contribute to differences in the images obtained, which would obscure the signal due to the gas motions. However, the degree of ionization in HH 529 III and II is so high that this turns out not to be an issue in this object. Results are presented in Table 14 and Figure 14.

We find that HH 529 III consists of at least two distinct moving structures. The large outer curved bow, which we call III a, is relatively smooth, spanning about 7 arcsec in its brightest part, but with fainter wings (best visible on the ratio image) that extend farther. We cover the bright part of the bow with 5 sample ellipses: a1 to a5, where a3 seems to be the apex of the bow but a2 is the one that falls in the UVES slit. Roughly 0.7 arcsec to the east of III a is a smaller, knottier bow, which we call III b and cover with 3 sample ellipses: b1, b2 and b3. The brightest knot is b2, but it is the b1 sample that falls in the UVES slit. HH 529 II is found to consist of three distinct bows with separations of order 1 arcsec, which we call II a, II b, and II c, with II a and II b falling in the UVES slit.

12 PHYSICAL ASPECTS OF THE HIGH VELOCITY COMPONENTS

As mentioned in the introduction and described in Section 4 moderate velocity shocks in H II regions can be considered isothermal. In a non-magnetic case, the total compression is given by

$$\frac{n_{\text{post}}}{n_{\text{pre}}} = M^2, \quad (20)$$

⁵ <https://drizzlepac.readthedocs.io>

⁶ We used version 1.07 of FLCT, obtained from <http://cgem.ssl.berkeley.edu/cgi-bin/cgem/FLCT/home>, together with version 1.04 of the Python wrapper pyflct, obtained from <https://github.com/PyDL/pyflct>.

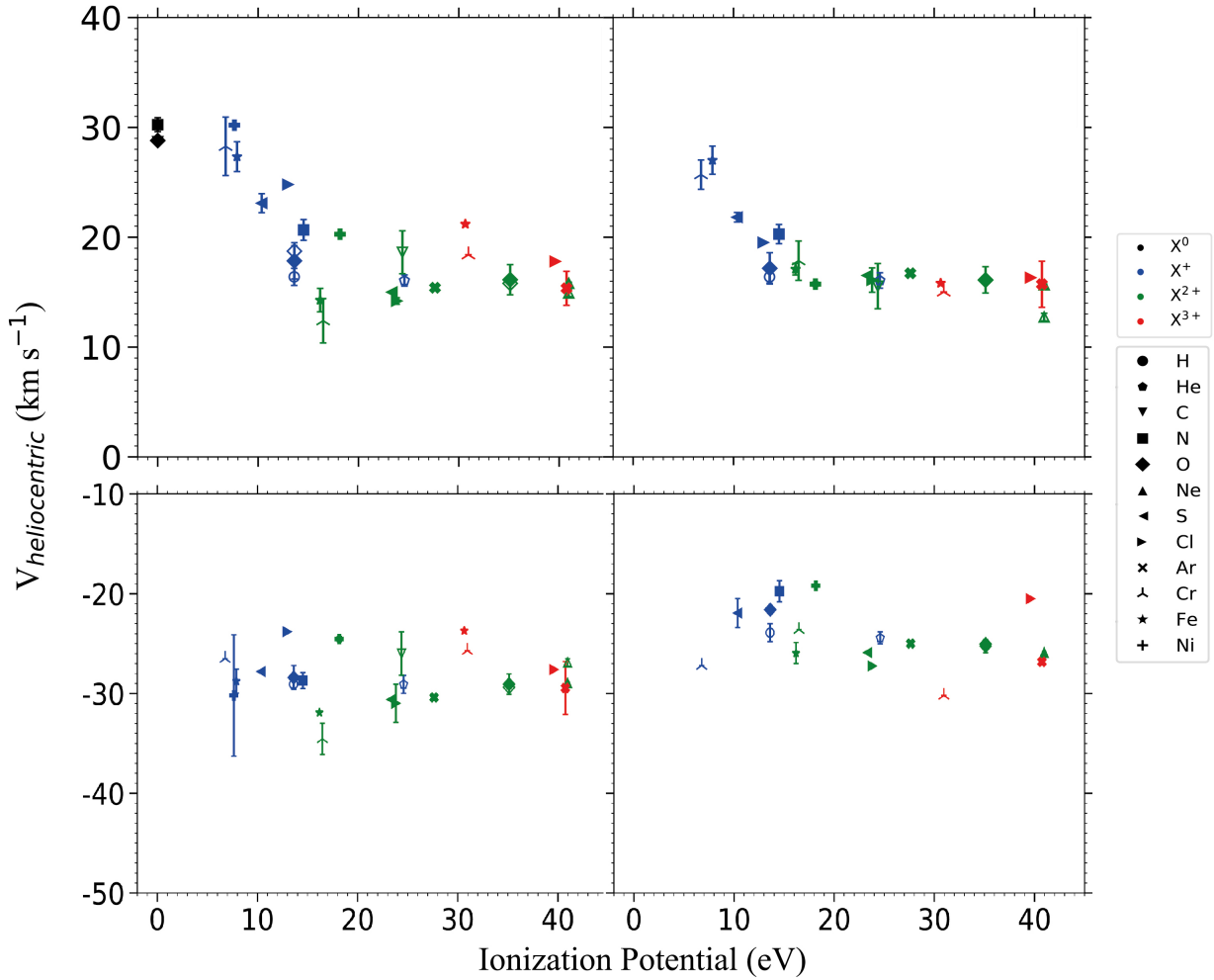


Figure 13. Observed radial velocity of the ions as function of the ionization potential. The upper left, bottom left and bottom right panels correspond to the radial velocities derived by considering the rest-frame reference wavelength λ_0 and the observed one λ in the heliocentric frame of reference for the nebular component of the cut 2, HH 529 II and HH 529 III, respectively. The upper right panel is defined with the difference of velocities between the nebular component and HH 529 II (subtraction of the upper and lower left panels) and rescaled using the velocity determined for H I lines, whose rest-frame reference wavelengths λ_0 are the best determined ones.

where M is the Mach number, while (n_{pre}) and (n_{post}) are the densities ahead and behind the shock, respectively. However, the presence of magnetic fields can be relevant in the structure of shocks since they can couple with the ions present in the gas creating a magnetohydrodynamical wave (Osterbrock & Ferland 2006).

Using the total or 3D velocity (v_{tot}) of the high-velocity components within the reference framework of the shock, and the sound speed in an ionized gas c_0 , we can calculate the Mach number M , using Eq. (21) and Eq. (22).

$$M = \frac{|v_{\text{tot}}|}{c_0}, \quad (21)$$

$$c_0 = \sqrt{\frac{\gamma k T}{\mu_0 m_H}}, \quad (22)$$

where k is the Boltzmann constant, T the temperature, μ_0 the mean mass per particle, m_H the hydrogen mass and γ the adiabatic index.

In Section 10.1, the heliocentric velocities of the different ions were presented for both shocks. Considering the OMC reference frame ($28 \pm 2 \text{ km s}^{-1}$, Goudis 1982) and the weighted average tangential motion of $35 \pm 5 \text{ km s}^{-1}$, calculated with the components a , b , $a2$ and $b1$ of HH 529 (see Fig. 14) and considering a systematic uncertainty of 2 km s^{-1} between the OMC and the stellar source of HH529, we obtain v_{tot} values of $62.68 \pm 3.30 \text{ km s}^{-1}$ and $67.01 \pm 3.09 \text{ km s}^{-1}$ for HH 529 III and HH 529 II, respectively. Considering $T_e = 8400 \pm 150 \text{ K}$ for the nebular component and $\gamma = 1$ (isothermal process), we obtain $c_0 = 11.80 \pm 0.10 \text{ km s}^{-1}$. Thus, assuming that both are external working surfaces (i.e. they correspond to shocks between the gas flow and the external nebular gas), we derive Mach numbers of $M = 5.31 \pm 0.28$ and $M = 5.68 \pm 0.27$ for HH 529 III and HH 529 II, respectively.

Using the density values for the HH objects given in Table 4 as representative of n_{post} , we can estimate the densities ahead the shocks. For HH 529 III we obtain $n_{\text{pre}} = 1070 \pm 310 \text{ cm}^{-3}$. This value is consistent with densities determined in photoionized areas of the Orion Nebula outside the Huygens region, where the density

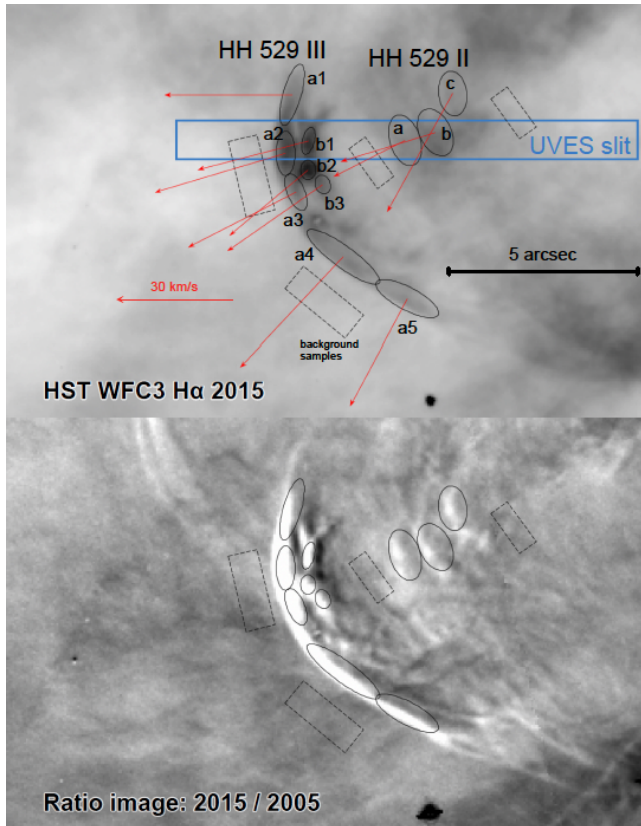


Figure 14. Tangential velocities of shock features in HH 529 II and III derived from 3 epochs of HST imaging. Upper panel shows various discrete features identified in the bow shocks (black ellipses with arrows indicating the average proper motion of each feature). Small dashed rectangles indicate regions where the nebular background brightness was measured and the large rectangle shows the position of the spectrograph slit. The background negative grayscale shows an *HST* WFC3 image in the F656N filter from 2015. Lower panel shows the ratio between the 2015 image and an *HST* ACS image in the F658N filter from 2005 (white means brighter in 2015). This highlights the changes in the nebula over that 10-year period, which are principally due to motions of the shocked gas.

decreases radially (Mesa-Delgado et al. 2008). This would place HH 529 III in the foreground of the main ionization front. On the other hand, considering also HH 529 II as an external working surface, we would obtain a pre-shock density $n_{\text{pre}} = 370 \pm 70 \text{ cm}^{-3}$, indicating that HH 529 II is impacting the ambient gas in a less dense or more external zone from where HH 529 III does. Thus, HH 529 II might be located farther from the main ionization front (and closer to the observer) than HH 529 III. However, this scenario seems unlikely, considering the similar ionization state of the gas in both HH objects. In addition to this, the more complex velocity structure of HH 529 III (that produces a larger velocity dispersion with respect to what is observed in HH 529 II) and that HH 529 III is almost a factor 3 denser than HH 529 II (see Section 5), suggest that HH 529 II may correspond to an internal working surface (Masciadri & Raga 2001) of the jet beam. In this case, the relevant Mach number may be substantially smaller than 5.68. This internal shock may be due to temporal velocity variations in the jet from the common source of HH 529 (possibly located at the star COUP 666, O'Dell et al. 2015). The scenario of HH jets emerging from a neutral cloud into an H II region has been studied in detail by Raga & Reipurth (2004).

Table 14. Proper motions of shock features

Feature	UVES cut	V_t km s $^{-1}$	PA deg	Contrast $S(\text{H}\alpha)/S(\text{H}\alpha, \text{BG})$
(1)	(2)	(3)	(4)	(5)
HH 529 III a1		33 ± 3	90 ± 3	0.46 ± 0.14
HH 529 III a2	3	36 ± 1	107 ± 7	0.82 ± 0.11
HH 529 III a3		32 ± 1	117 ± 3	0.52 ± 0.14
HH 529 III a4		39 ± 2	137 ± 5	0.41 ± 0.07
HH 529 III a5		32 ± 1	152 ± 10	0.27 ± 0.07
HH 529 III b1	3	30 ± 2	105 ± 3	0.95 ± 0.09
HH 529 III b2		27 ± 1	130 ± 1	1.14 ± 0.10
HH 529 III b3		30 ± 2	125 ± 4	0.64 ± 0.07
HH 529 II a	2	21 ± 9	117 ± 58	0.25 ± 0.03
HH 529 II b	2	26 ± 5	107 ± 4	0.35 ± 0.08
HH 529 II c		35 ± 9	151 ± 87	0.22 ± 0.03

COLUMNS: (1) Name of shock feature (see Fig. 14 for positions). (2) Spatial cut of the UVES spectrum where this feature appears, if any. (3) Mean tangential velocity for each feature, weighted by background-subtracted surface brightness, $S(\text{H}\alpha)$, of each pixel. (4) Mean position angle of proper motion, weighted in the same way. (5) Mean relative H α brightness with respect to nebular background (BG). For columns 3, 4, and 5, the \pm uncertainties correspond to the root-mean-square variation over each sample region and do not include systematic uncertainties, which are of order 2 km s $^{-1}$

The absence of [O I] (see Fig. 2) and the weakness of lines of low ionization potential ions (e.g. [O II] or [N II]) demonstrate that HH 529 II and HH 529 III are fully photoionized objects and do not contain a trapped ionization front (Masciadri & Raga 2001), contrary to what was found by Mesa-Delgado et al. (2009) in the case of HH 202 S. Due to the fact that HH 529 is fully photoionized, we can assure that the entire jet beam inside the H II region should be observable in optical emission lines, contrary to partially ionized or neutral Herbig-Haro objects, where only limited regions can be observed in the optical (Raga et al. 2000a,b).

Using the ratio between the tangential ($35 \pm 5 \text{ km s}^{-1}$) and radial ($-57 \pm 2 \text{ km s}^{-1}$) velocities of HH 529 we estimate a flow angle of $58 \pm 4^\circ$. This value is in agreement with the result of O'Dell & Henney (2008) ($\sim 54^\circ$) but discrepant with the values obtained by O'Dell et al. (2015) ($\sim 83^\circ$). The value of the flow angle we obtain implies that the observed spectra of the HH objects should integrate the emission along a fraction of the ionized jet beam, including the compressed gas at the leading working surface and the gas of the jet beam behind. Which of these dominates the total emission depends on the relative densities of the jet and the ambient medium (Hartigan 1989). In the case of HH 529 III, it is possible that the two components, a and b, resolved by HST (see Fig. 14) represent respectively the bowshock (shocked ambient medium) and Mach disk (shocked jet). However, these are unresolved in our slit spectra.

13 SUMMARY AND CONCLUSIONS

We have observed two of the bow shocks of the photoionized Herbig-Haro object HH 529: HH 529 II and HH 529 III, inside the Orion Nebula, under photometric conditions with the UVES echelle spectrograph at VLT. Our observations have an effective spectral resolution of $\sim 6.5 \text{ km s}^{-1}$ and cover a spectral range of 3100–10420Å. We defined 4 spatial cuts in our 10 arcsecs-long slit to separate HH 529 II from HH 529 III. Our spatial and spectral resolution permitted us to resolve the blueshifted high-velocity components of HH 529 II and III from the nebular emission of the Orion

Nebula. Thus, we analysed 6 1D spectra: 4 of the nebular emission and one of each bow shock. We measured up to 633 emission lines in the Orion Nebula and 376 and 245 in the cases of HH 529 II and III, respectively. We defined an additional spectrum labeled as “combined cuts” with the sum of all components to study the impact of the HH objects in a single low-spectral resolution longslit observation. We also take advantage of the 20 years of archival *HST* imaging to analyse proper motions of HH 529 and their physical impact.

Considering the absence of emission lines of neutral elements such as [O I] and the rather faint emission from low ionization ions such as [O II] in HH 529 II and III, we conclude that they are fully photoionized and present a high ionization degree. We analysed 5 density diagnostics based on CEL ratios. We found a mean value of $n_e \approx 6000 \pm 1000 \text{ cm}^{-3}$ for the nebular components. We obtain $n_e = 11880 \pm 1860 \text{ cm}^{-3}$ and $n_e = 30200 \pm 8080 \text{ cm}^{-3}$ for HH 529 II and III, respectively, concluding that at so high values, the density diagnostics based on [Fe III] lines are more suitable than the usual ones. We determined the density of each component using the RLs of multiplet 1 of O II, finding that it does not differ from the one derived from CELs in the nebular components. However, the results based on O II RLs are inconsistent with other diagnostics in the case of HH 529 II and III.

Using CEL ratios, we study 6 T_e -diagnostics. We derive mean values of $T_e(\text{low}) \approx 10000 \pm 200 \text{ K}$ and $T_e(\text{high}) \approx 8500 \pm 150 \text{ K}$ for the temperature of the low and high ionization degree zones, respectively, in the nebular components. For HH 529 II we obtain $T_e(\text{low}) = 10150^{+570}_{-510} \text{ K}$ and $T_e(\text{high}) = 8270 \pm 110 \text{ K}$. For HH 529 III, we derive $T_e(\text{low}) = 11040^{+920}_{-970} \text{ K}$ and $T_e(\text{high}) = 8630 \pm 120 \text{ K}$. These results indicate that the temperature are very similar in the nebular and the high-velocity components, although there is a slight increase in temperature in the shock front (HH 529 III). For the nebular component of cut 2, we were able to estimate T_e from O II RLs, obtaining $T_e(\text{O II}) = 9350 \pm 1090$. The good agreement between $T_e(\text{O II})$ and $n_e(\text{O II})$ with the physical conditions obtained with CELs in the nebular components demonstrate that the emission of CELs and RLs of O²⁺ come basically from the same gas, ruling out the possibility of cold clumps dominating the emission in RLs. For all components, we derive $T_e(\text{He I})$ from He I RL ratios while in the “combined cuts” spectra we were also able to derive $T_e(\text{H I})$ using both the Balmer and the Paschen discontinuities of the nebular continuum. In all the derived physical conditions, we found no significant deviation between the results of the “combined cuts” spectrum and the individual nebular ones. We conclude that the emission of HH 529 II and HH 529 III do not alter the physical conditions and abundances derived from low spectral resolution spectra in areas of size of the order or larger than 10 arcsecs.

Based on the different temperature determinations available and following the Peimbert's t^2 -formalism, we estimate $t_{\text{high}}^2 = 0.021 \pm 0.003$, $t_{\text{inter}}^2 = 0.051 \pm 0.009$ and $t_{\text{low}}^2 = 0.064 \pm 0.011$ for the high, intermediate, and low ionization zones both for the nebular and the high-velocity components. We derive ionic abundances of O⁺, N⁺, S⁺, Cl⁺, Ni²⁺, Fe²⁺, S²⁺, Cl²⁺, O²⁺, Ne²⁺, Ar²⁺, Cl³⁺, Ar³⁺ and Fe³⁺ based on CELs both in the case of $t^2 = 0$ and $t^2 > 0$. We estimated ionic abundances of He⁺, O⁺, O²⁺, C²⁺ and Ne²⁺ based on RLs. The mean ADF values for the nebular components are $\text{ADF(O}^+\text{)} \approx 0.50 \pm 0.13 \text{ dex}$, $\text{ADF(O}^{2+}\text{)} \approx 0.20 \pm 0.05 \text{ dex}$, $\text{ADF(C}^{2+}\text{)} \approx 0.50 \pm 0.03 \text{ dex}$ and $\text{ADF(Ne}^{2+}\text{)} \approx 0.35 \pm 0.10 \text{ dex}$. For HH 529 II, we obtained $\text{ADF(O}^{2+}\text{)} = 0.29 \pm 0.10 \text{ dex}$ and $\text{ADF(Ne}^{2+}\text{)} = 0.79 \pm 0.09 \text{ dex}$ while for HH 529 III we obtained $\text{ADF(O}^{2+}\text{)} = 0.36 \pm 0.11 \text{ dex}$. The t^2 values we obtained are capable

of account for the ADF(O²⁺) in the nebular components but not in the ones corresponding to HH 529 II and III, where larger t^2 values would be needed to reproduce their ADF(O²⁺).

We estimate the total abundances of O, Cl, Ar and Fe without ICFs in the nebular components. In the cases of HH 529 II and III, in addition to the aforementioned elements (except Fe in HH 529 III), we were also able to estimate the total abundances of He and C without using an ICF. By using the Solar value of Fe/O as reference, we estimate that 6% of the total Fe is in gaseous phase in the nebular components while in HH 529 II this fraction reaches 14% and between 10% and 25% in HH 529 III. This increase should be due to destruction of dust grains in the shock fronts. We found a slight overabundance of heavy elements (around 0.12 dex) in the high-velocity components that can not be entirely due to dust destruction processes since it affects also the noble gases. We speculate that its possible origin may lie in the inclusion of H-deficient gas entrained after the evaporation of material in the outer part of the protoplanetary disc of the source of HH 529.

We found a constant value of the radial velocity of the emission lines, irrespective of the ionization potential of the observed ions in HH 529 II ($v_r = -29.08 \pm 0.36 \text{ km s}^{-1}$) and HH 529 III ($v_r = -23.90 \pm 0.89 \text{ km s}^{-1}$). In the nebular emission of the Orion Nebula, we demonstrate that the velocity varies linearly with the ionization potential for ions with ionization potential between 6.77 and 13.6 eV, reaching a constant velocity of $16.4 \pm 0.8 \text{ km s}^{-1}$ for ionization potentials greater than 13.6. From the thermal broadening of the line profiles, we derived $T_e = 8340 \pm 410$, $T_e = 8670 \pm 50$ and $T_e = 10470 \pm 50$ for the nebular components, HH 529 II and III, respectively. The determination for HH 529 III is anomalously large due to the contamination by unresolved velocity components.

We determined the proper motions of HH 529 II and III by using HST imaging over 20 years. We found several discrete features identified in the bow shocks. We estimated an average tangential velocity of $35 \pm 5 \text{ km s}^{-1}$ for the HH 529 II-III system. We also estimate a flow angle with respect to the sky plane of $58 \pm 4^\circ$. By deriving the Mach number of HH 529 II and III, we determine a pre-shock density $n_{\text{pre}} = 1070 \pm 310 \text{ cm}^{-3}$ for HH 529 III, placing it in the foreground of the main ionization front. Several lines of evidence indicate that HH 529 II corresponds to an internal working surface of the jet beam.

DATA AVAILABILITY

The lines measured in the spectra are entirely available in online tables annexed to this article. The rest of information is found in tables or references of this paper.

ACKNOWLEDGEMENTS

We acknowledge support from the State Research Agency (AEI) of the Spanish Ministry of Science, Innovation and Universities (MCIU) and the European Regional Development Fund (FEDER) under grant with references AYA2015-65205-P and AYA2017-83383-P. JG-R acknowledges support from an Advanced Fellowship from the Severo Ochoa excellence program (SEV-2015-0548). The authors acknowledge support under grant P/308614 financed by funds transferred from the Spanish Ministry of Science, Innovation and Universities, charged to the General State Budgets and with funds transferred from the General Budgets of the Autonomous

Community of the Canary Islands by the MCIU. KZA-C acknowledges support from Mexican CONACYT posdoctoral grant 364239. JEM-D acknowledges support of the Instituto de Astrofísica de Canarias under the Astrophysicist Resident Program and acknowledges support from the Mexican CONACyT (CVU 602402). AM-D acknowledges support from the FONDECYT project 3140383. WJH acknowledges support from DGAPA-UNAM PAPIIT IN107019.

REFERENCES

- Arellano-Córdova K. Z., Esteban C., García-Rojas J., Méndez-Delgado J. E., 2020, *MNRAS*, **496**, 1051
- Astropy Collaboration et al., 2013, *A&A*, **558**, A33
- Aver E., Olive K. A., Skillman E. D., 2011, *J. Cosmology Astropart. Phys.*, **2011**, 043
- Baldwin J. A., et al., 1996, *ApJ*, **468**, L115
- Ballester P., Modigliani A., Boitquin O., Cristiani S., Hanuschik R., Kaufer A., Wolf S., 2000, *The Messenger*, **101**, 31
- Bally J., Reipurth B., 2001, *ApJ*, **546**, 299
- Bally J., Reipurth B., 2018, *Research Notes of the American Astronomical Society*, **2**, 46
- Bally J., Sutherland R. S., Devine D., Johnstone D., 1998, *AJ*, **116**, 293
- Bally J., O'Dell C. R., McCaughrean M. J., 2000, *AJ*, **119**, 2919
- Bastin R. J., Storey P. J., 2006, in Barlow M. J., Méndez R. H., eds, IAU Symposium Vol. 234, Planetary Nebulae in our Galaxy and Beyond. pp 369–370, doi:10.1017/S1743921306003280
- Bautista M. A., 2001, *A&A*, **365**, 268
- Benjamin R. A., Skillman E. D., Smits D. P., 2002, *ApJ*, **569**, 288
- Berg D. A., Erb D. K., Henry R. B. C., Skillman E. D., McQuinn K. B. W., 2019, *ApJ*, **874**, 93
- Berg D. A., Pogge R. W., Skillman E. D., Croxall K. V., Moustakas J., Rogers N. S. J., Sun J., 2020, *ApJ*, **893**, 96
- Blagrade K. P. M., Martin P. G., Baldwin J. A., 2006, *ApJ*, **644**, 1006
- Blagrade K. P. M., Martin P. G., Rubin R. H., Dufour R. J., Baldwin J. A., Hester J. J., Walter D. K., 2007, *ApJ*, **655**, 299
- Bohigas J., 2015, *MNRAS*, **453**, 1281
- Bowen I. S., 1955, *ApJ*, **121**, 306
- Brown R. L., Mathews W. G., 1970, *ApJ*, **160**, 939
- Butler K., Zeippen C. J., 1989, *A&A*, **208**, 337
- D'Odorico S., Cristiani S., Dekker H., Hill V., Kaufer A., Kim T., Primas F., 2000, Performance of UVES, the echelle spectrograph for the ESO VLT and highlights of the first observations of stars and quasars. pp 121–130, doi:10.1111/12.390133
- Davey A. R., Storey P. J., Kisielius R., 2000, *A&AS*, **142**, 85
- Delgado-Ingla G., Morisset C., Stasińska G., 2014, *MNRAS*, **440**, 536
- Delgado-Ingla G., Mesa-Delgado A., García-Rojas J., Rodríguez M., Esteban C., 2016, *MNRAS*, **456**, 3855
- Domínguez-Guzmán G., Rodríguez M., Esteban C., García-Rojas J., 2019, arXiv e-prints, p. arXiv:1906.02102
- Ellis D. G., Martinson I., 1984, *Phys. Scr.*, **30**, 255
- Espíritu J. N., Peimbert A., Delgado-Ingla G., Ruiz M. T., 2017, *Rev. Mex. Astron. Astrofis.*, **53**, 95
- Esteban C., Peimbert M., 1999, *A&A*, **349**, 276
- Esteban C., Peimbert M., Torres-Peimbert S., Escalante V., 1998, *MNRAS*, **295**, 401
- Esteban C., Peimbert M., García-Rojas J., Ruiz M. T., Peimbert A., Rodríguez M., 2004, *MNRAS*, **355**, 229
- Fang X., Liu X. W., 2011, *MNRAS*, **415**, 181
- Fang X., Liu X. W., 2013, *MNRAS*, **429**, 2791
- Fehrenbach C., 1977, *A&AS*, **29**, 71
- Ferland G. J., 2001, *PASP*, **113**, 41
- Ferland G. J., Henney W. J., O'Dell C. R., Porter R. L., van Hoof P. A. M., Williams R. J. R., 2012, *ApJ*, **757**, 79
- Feuchtgruber H., et al., 1997, *ApJ*, **487**, 962
- Fisher G. H., Welsch B. T., 2008, in Howe R., Komm R. W., Balasubramanian K. S., Petrie G. J. D., eds, *Astronomical Society of the Pacific Conference Series Vol. 383, Subsurface and Atmospheric Influences on Solar Activity*. p. 373 (arXiv:0712.4289)
- Fritzsche S., Fricke B., Geschke D., Heitmann A., Sienkiewicz J. E., 1999, *ApJ*, **518**, 994
- Froese Fischer C., Tachiev G., 2004, *Atomic Data and Nuclear Data Tables*, **87**, 1
- Froese Fischer C., Rubin R. H., Rodríguez M., 2008, *MNRAS*, **391**, 1828
- Galavis M. E., Mendoza C., Zeippen C. J., 1995, *A&AS*, **111**, 347
- García-Díaz M. T., Henney W. J., López J. A., Doi T., 2008, *Rev. Mex. Astron. Astrofis.*, **44**, 181
- García-Rojas J., Esteban C., 2007, *ApJ*, **670**, 457
- García-Rojas J., Esteban C., Peimbert M., Rodríguez M., Ruiz M. T., Peimbert A., 2004, *ApJS*, **153**, 501
- García-Rojas J., Esteban C., Peimbert A., Peimbert M., Rodríguez M., Ruiz M. T., 2005, *MNRAS*, **362**, 301
- García-Rojas J., Esteban C., Peimbert A., Rodríguez M., Peimbert M., Ruiz M. T., 2007, *Rev. Mex. Astron. Astrofis.*, **43**, 3
- García-Rojas J., Peña M., Morisset C., Delgado-Ingla G., Mesa-Delgado A., Ruiz M. T., 2013, *A&A*, **558**, A122
- García-Rojas J., Madonna S., Luridiana V., Sterling N. C., Morisset C., Delgado-Ingla G., Toribio San Cipriano L., 2015, *MNRAS*, **452**, 2606
- Gómez-Llanos V., Morisset C., 2020, *MNRAS*, **497**, 3363
- Goudis C., 1982, The Orion complex: A case study of interstellar matter. 0067-0057 Vol. 90, doi:10.1007/978-94-009-7712-9,
- Grandi S. A., 1975a, *ApJ*, **196**, 465
- Grandi S. A., 1975b, *ApJ*, **199**, L43
- Grieve M. F. R., Ramsbottom C. A., Hudson C. E., Keenan F. P., 2014, *ApJ*, **780**, 110
- Haro G., 1952, *ApJ*, **115**, 572
- Haro G., 1953, *ApJ*, **117**, 73
- Hartigan P., 1989, *ApJ*, **339**, 987
- Henney W. J., 2002, *Rev. Mex. Astron. Astrofis.*, **38**, 71
- Henney W. J., Stasińska G., 2010, *ApJ*, **711**, 881
- Herbig G. H., 1950, *ApJ*, **111**, 11
- Herbig G. H., 1951, *ApJ*, **113**, 697
- Herbig G. H., 1952, *J. R. Astron. Soc. Canada*, **46**, 222
- Izotov Y. I., Stasińska G., Meynet G., Guseva N. G., Thuan T. X., 2006, *A&A*, **448**, 955
- Johansson S., Zethson T., Hartman H., Ekberg J. O., Ishibashi K., Davidson K., Gull T., 2000, *A&A*, **361**, 977
- Jones A. P., Tielens A. G. G. M., Hollenbach D. J., McKee C. F., 1994, *ApJ*, **433**, 797
- Juan de Dios L., Rodríguez M., 2017, *MNRAS*, **469**, 1036
- Kaler J. B., 1967, *ApJ*, **148**, 925
- Kaufman V., Martin W. C., 1993, *Journal of Physical and Chemical Reference Data*, **22**, 279
- Kaufman V., Sugar J., 1986, *Journal of Physical and Chemical Reference Data*, **15**, 321
- Kingdon J. B., Ferland G. J., 1995, *ApJ*, **450**, 691
- Kisielius R., Storey P. J., Davey A. R., Neale L. T., 1998, *A&AS*, **133**, 257
- Kisielius R., Storey P. J., Ferland G. J., Keenan F. P., 2009, *MNRAS*, **397**, 903
- Kunth D., Sargent W. L. W., 1983, *ApJ*, **273**, 81
- Liu X. W., Storey P. J., Barlow M. J., Danziger I. J., Cohen M., Bryce M., 2000, *MNRAS*, **312**, 585
- Liu X. W., Luo S. G., Barlow M. J., Danziger I. J., Storey P. J., 2001, *MNRAS*, **327**, 141
- Lodders K., 2019, arXiv e-prints, p. arXiv:1912.00844
- Lucy L. B., 1995, *A&A*, **294**, 555
- Luridiana V., Morisset C., Shaw R. A., 2015, *A&A*, **573**, A42
- Masciadri E., Raga A. C., 2001, *A&A*, **376**, 1073
- McLaughlin B. M., Lee T.-G., Ludlow J. A., Land i E., Loch S. D., Pindzola M. S., Ballance C. P., 2011, *Journal of Physics B Atomic Molecular Physics*, **44**, 175206
- McNabb I. A., Fang X., Liu X. W., Bastin R. J., Storey P. J., 2013, *MNRAS*, **428**, 3443

- Méndez-Delgado J. E., Esteban C., García-Rojas J., Arellano-Córdova K. Z., Valerdi M., 2020, *MNRAS*, **496**, 2726
- Mendoza C., 1983, in Aller L. H., ed., IAU Symposium Vol. 103, Planetary Nebulae, pp 143–172
- Mendoza C., Zeippen C. J., 1982a, *MNRAS*, **198**, 127
- Mendoza C., Zeippen C. J., 1982b, *MNRAS*, **199**, 1025
- Mendoza C., Zeippen C. J., 1983, *MNRAS*, **202**, 981
- Mesa-Delgado A., Esteban C., García-Rojas J., 2008, *ApJ*, **675**, 389
- Mesa-Delgado A., Esteban C., García-Rojas J., Luridiana V., Bautista M., Rodríguez M., López-Martín L., Peimbert M., 2009, *MNRAS*, **395**, 855
- Moehler S., Dreizler S., LeBlanc F., Khalack V., Michaud G., Richer J., Sweigart A. V., Grundahl F., 2014a, *A&A*, **565**, A100
- Moehler S., et al., 2014b, *A&A*, **568**, A9
- Mouri H., Taniguchi Y., 2000, *ApJ*, **534**, L63
- Nicholls D. C., Dopita M. A., Sutherland R. S., 2012, *ApJ*, **752**, 148
- O'Dell C. R., 2001, *ARA&A*, **39**, 99
- O'Dell C. R., 2018, *MNRAS*, **478**, 1017
- O'Dell C. R., Henney W. J., 2008, *AJ*, **136**, 1566
- O'Dell C. R., Wen Z., 1992, *ApJ*, **387**, 229
- O'Dell C. R., Ferland G. J., Henney W. J., Peimbert M., García-Díaz M. T., Rubin R. H., 2015, *AJ*, **150**, 108
- O'Dell C. R., Abel N. P., Ferland G. J., 2020, *ApJ*, **891**, 46
- Olive K. A., Skillman E. D., 2004, *ApJ*, **617**, 29
- Osterbrock D. E., Ferland G. J., 2006, Astrophysics of gaseous nebulae and active galactic nuclei
- Osterbrock D. E., Tran H. D., Veilleux S., 1992, *ApJ*, **389**, 305
- Pagel B. E. J., Simonson E. A., Terlevich R. J., Edmunds M. G., 1992, *MNRAS*, **255**, 325
- Peimbert M., 1967, *ApJ*, **150**, 825
- Peimbert A., 2003, *ApJ*, **584**, 735
- Peimbert M., Costero R., 1969, Boletín de los Observatorios Tonantzintla y Tacubaya, **5**, 3
- Peimbert A., Peimbert M., 2013, *ApJ*, **778**, 89
- Peimbert A., Peimbert M., Luridiana V., 2002, *ApJ*, **565**, 668
- Pequignot D., Petitjean P., Boisson C., 1991, *A&A*, **251**, 680
- Péquignot D., Amara M., Liu X. W., Barlow M. J., Storey P. J., Morisset C., Torres-Peimbert S., Peimbert M., 2002, in Henney W. J., Franco J., Martos M., eds, Revista Mexicana de Astronomía y Astrofísica Conference Series Vol. 12, Revista Mexicana de Astronomía y Astrofísica Conference Series, pp 142–143
- Persson W., Wahlström C.-G., Jönsson L., Di Rocco H. O., 1991, *Phys. Rev. A*, **43**, 4791
- Podobedova L. I., Kelleher D. E., Wiese W. L., 2009, Journal of Physical and Chemical Reference Data, **38**, 171
- Porter R. L., Ferland G. J., MacAdam K. B., 2007, *ApJ*, **657**, 327
- Porter R. L., Ferland G. J., Storey P. J., Detisch M. J., 2012, *MNRAS*, **425**, L28
- Porter R. L., Ferland G. J., Storey P. J., Detisch M. J., 2013, *MNRAS*, **433**, L89
- Price-Whelan A. M., et al., 2018, *AJ*, **156**, 123
- Quinet P., 1996, *A&AS*, **116**, 573
- Raga A. C., Reipurth B., 2004, Rev. Mex. Astron. Astrofis., **40**, 15
- Raga A. C., López-Martín J., López J. A., Meaburn J., 2000a, in Arthur S. J., Brickhouse N. S., Franco J., eds, Revista Mexicana de Astronomía y Astrofísica Conference Series Vol. 9, Revista Mexicana de Astronomía y Astrofísica Conference Series, pp 191–193
- Raga A., et al., 2000b, *MNRAS*, **314**, 681
- Ramsbottom C. A., Bell K. L., 1997, *Atomic Data and Nuclear Data Tables*, **66**, 65
- Reipurth B., Bally J., 2001, *ARA&A*, **39**, 403
- Roberto M., et al., 2005, *AJ*, **129**, 1534
- Roberto M., et al., 2013, *ApJS*, **207**, 10
- Rodríguez M., 1999, *A&A*, **348**, 222
- Rodríguez M., 2002, *A&A*, **389**, 556
- Rodríguez M., 2020, *MNRAS*, **495**, 1016
- Rodríguez M., Rubin R. H., 2005, *ApJ*, **626**, 900
- Rubin R. H., Simpson J. P., O'Dell C. R., McNabb I. A., Colgan S. W. J., Zhuge S. Y., Ferland G. J., Hidalgo S. A., 2011, *MNRAS*, **410**, 1320
- Schwartz R. D., 1983, *ARA&A*, **21**, 209
- Simón-Díaz S., Stasińska G., 2011, *A&A*, **526**, A48
- Smith N., Bally J., Shuping R. Y., Morris M., Kassis M., 2005, *AJ*, **130**, 1763
- Stasińska G., 1978, *A&A*, **66**, 257
- Stasińska G., Tenorio-Tagle G., Rodríguez M., Henney W. J., 2007, *A&A*, **471**, 193
- Storey P. J., 1994, *A&A*, **282**, 999
- Storey P. J., Hummer D. G., 1995, *MNRAS*, **272**, 41
- Storey P. J., Zeippen C. J., 2000, *MNRAS*, **312**, 813
- Storey P. J., Sochi T., Badnell N. R., 2014, *MNRAS*, **441**, 3028
- Storey P. J., Sochi T., Bastin R., 2017, *MNRAS*, **470**, 379
- Tayal S. S., 2004, *A&A*, **418**, 363
- Tayal S. S., 2011, *ApJS*, **195**, 12
- Tayal S. S., Zatsarinny O., 2010, *ApJS*, **188**, 32
- Tody D., 1993, IRAF in the Nineties. p. 173
- Torres-Peimbert S., Peimbert M., Daltabuit E., 1980, *ApJ*, **238**, 133
- Tsamis Y. G., Walsh J. R., Vilchez J. M., Péquignot D., 2011, *MNRAS*, **412**, 1367
- Tsamis Y. G., Flores-Fajardo N., Henney W. J., Walsh J. R., Mesa-Delgado A., 2013, *MNRAS*, **430**, 3406
- Van Hoof P. A. M., 2018, *Galaxies*, **6**
- Verner E. M., Verner D. A., Baldwin J. A., Ferland G. J., Martin P. G., 2000, *ApJ*, **543**, 831
- Vilchez J. M., Pagel B. E. J., 1988, *MNRAS*, **231**, 257
- Walter D. K., Dufour R. J., Hester J. J., 1992, *ApJ*, **397**, 196
- Welsch B. T., Fisher G. H., Abbott W. P., Regnier S., 2004, *ApJ*, **610**, 1148
- Wesson R., Jones D., García-Rojas J., Boffin H. M. J., Corradi R. L. M., 2018, *MNRAS*, **480**, 4589
- Wiese W. L., Fuhr J. R., Deters T. M., 1996, Journal of Physical and Chemical Reference Data, Monograph 7, 403
- Yuan H. B., Liu X. W., Péquignot D., Rubin R. H., Ercolano B., Zhang Y., 2011, *MNRAS*, **411**, 1035
- Zhang Y., Liu X. W., 2006, in Barlow M. J., Méndez R. H., eds, IAU Symposium Vol. 234, Planetary Nebulae in our Galaxy and Beyond. pp 547–548 ([arXiv:astro-ph/0605180](https://arxiv.org/abs/astro-ph/0605180)), doi:10.1017/S1743921306004170
- Zhang H. L., Pradhan A. K., 1997, *A&AS*, **126**, 373
- Zhang, Hong Lin 1996, *Astron. Astrophys. Suppl. Ser.*, **119**, 523
- Zhang Y., Liu X. W., Liu Y., Rubin R. H., 2005, *MNRAS*, **358**, 457

APPENDIX A: THE ALLEGED OBSERVATION OF Si IV $\lambda 4088.86$ LINE.

Several authors used the $I(\text{O II } \lambda 4649.13)/I(\text{O II } \lambda 4089.29)$ ratio to derive T_e based on its theoretical dependence on T_e and insensitivity to n_e (see e. g. García-Rojas & Esteban 2007; Fang & Liu 2013; McNabb et al. 2013; Wesson et al. 2018). Nevertheless, Peimbert & Peimbert (2013) discourages its use, due (among other reasons) to the possible contamination of O II $\lambda 4089.29$ by the Si IV $\lambda 4088.86$ line, which would lead to underestimating T_e . The authors consider that Si IV $\lambda 4088.86$ has been detected in 2 H II regions observed with UVES echelle spectrograph at VLT telescope: the Orion Nebula (Esteban et al. 2004) and 30 Doradus (Peimbert 2003). Although it is a real possibility that a line like Si IV $\lambda 4088.86$ may be detected in an H II region, much of the flux attributed to this line is actually due to an observational artifact of UVES spectrum.

Fig. D2 shows the echelle orders extracted in an UVES blue arm spectrum using dichroic #2 ($\Delta\lambda = 3750 - 4995$). Optical reflections produced by the dichroic #2 in the blue arm can be noted as vertical lines crossing the echelle orders. These artifacts are negligible with the exception of those produced by the most intense lines: [O III] $\lambda 4959$, H β and [O III] $\lambda 5007$. The last of those lines does not enter in any complete echelle order in this arm, but it is partially observed at the edge of the CCD, together with its associated high-velocity component. As a consequence 4 main sources of “ghost lines” can be noticed. The third of them (from left to right), affects exactly the $\lambda 4089.07$ position in the echelle order number 11 (bottom up) in our observations. Approximately at this wavelength we expect to have the high velocity component of O II $\lambda 4089.29$ in cuts 2 and 3, but it must be free of emission from HH 529 II and III in cut 4. Fig. D6 shows the emission around $\lambda 4089.29$ in the spectra of cut 4, a pretty similar image than the Fig. 2 from Peimbert & Peimbert (2013).

In our spectra, an hypothetical Si IV $\lambda 4088.86$ line should be observed at $\lambda 4089.08$, considering the kinematical structure of the nebular component and the high ionization potential of the line (see Section 10.1). This means that in case of being detected, the Si IV $\lambda 4088.86$ line would be indistinguishable from the ghost line at $\lambda 4089.07$. We have measured the intensity of ghost lines coming from the same source than $\lambda 4089.07$ along the echelle orders but excluding those ones which are blended with other nebular lines. Fig. D3 shows the decreasing trend of the intensity of ghost emission with respect to its source from higher to lower orders, as well as a least squares fit to predict ghost emission in order 11, where the emission feature at $\lambda 4089.07$ lies. The predicted ghost emission in $\lambda 4089.07$ is $\frac{F(\lambda)}{F(\text{H}\beta)} = 0.007$ while the rms of the noise associated with the continuum in cut 4 around $\lambda 4089.07$ represents a possible contribution of $\frac{F(\text{rms})}{F(\text{H}\beta)} = 0.004$. On the other hand, the measured flux of $\lambda 4089.07$ is $\frac{F(\lambda)}{F(\text{H}\beta)} = 0.012$. Thus, the emission observed at $\lambda 4089.07$ is consistent with purely ghost emission. This ghost emission affects in a similar way the spectra of the Orion Nebula and 30 Dor analysed by Esteban et al. (2004) and Peimbert (2003), respectively.

The main drawback of the T_e diagnostic based on the $I(\text{O II } \lambda 4649.13)/I(\text{O II } \lambda 4089.29)$ ratio in H II regions is that $\lambda 4089.29$ is rather weak, providing uncertain T_e values. Therefore, this diagnostic will only be useful when the O II lines are well measured, or when the object shows significant difference between the T_e of the zone where the O II lines are formed and the rest of the nebula (Wesson et al. 2018). Finally, although Si IV lines are expected to be rather faint in normal H II regions, this may not be the case in high-

ionization planetary nebulae (PNe) as NGC 3918 (García-Rojas et al. 2015).

APPENDIX B: Cl²⁺ AND Cl ABUNDANCES

Domínguez-Guzmán et al. (2019) have proposed the use of $T_e(\text{[N II]})$ to determine the Cl²⁺ abundance in a sample of 37 Galactic and extragalactic H II regions, including the Orion Nebula (using the data of Esteban et al. 2004). They argue that $T_e(\text{[N II]})$ reduces the dispersion of the Cl/O ratio and remove trends in the Cl/O versus O/H relation. However, in a detailed study of each specific object, the optimal temperature to adopt can differ from what statistically would be the best choice. Considering the IP of 23.8 eV of Cl²⁺, in between of those of N⁺ (14.5 eV) and O²⁺ (35.1 eV), we expect that a T_e representative of an intermediate ionization zone as $T_e(\text{[S III]})$ should be more appropriate for determining the Cl²⁺ abundance. **The relationship of $T_e(\text{[S III]})$ with $T_e(\text{[N II]})$ and $T_e(\text{[O III]})$ may depend on the ionization degree of the gas (Berg et al. 2020).** In our spectra, we are able to calculate the total Cl abundance because we measure CELs of all the ionization species of Cl that are expected to be present in the Orion Nebula. We test the resulting Cl abundance considering three different temperatures: $T_e(\text{low})$, $T_e(\text{[S III]})$ and $T_e(\text{high})$ for deriving the Cl²⁺/H⁺ ratio. In Table D10, we present the Cl²⁺ and Cl abundances as well as their corresponding log(Cl/O) values using the three aforementioned temperatures.

Using $T_e(\text{low})$, we obtain a log(Cl/O) value in the high-velocity components about 0.1 dex lower with respect to the value found in the nebular ones of the different cuts. This suggests that $T_e(\text{low})$ is slightly underestimating the Cl/H ratio, although within the uncertainties. Conversely, the Cl/O ratio becomes more consistent when using $T_e(\text{[S III]})$ or $T_e(\text{high})$ to estimate the Cl²⁺ abundance. We obtain a mean log(Cl/O) value of -3.63 ± 0.04 , -3.42 ± 0.03 and -3.50 ± 0.03 when adopting $T_e(\text{low})$, $T_e(\text{high})$ or $T_e(\text{[S III]})$ to calculate the Cl²⁺ abundance, respectively. The log(Cl/O) value obtained using $T_e(\text{[S III]})$ is the one closest to the solar value of -3.50 ± 0.09 recommended by Lodders (2019). Therefore, we finally adopt $T_e(\text{[S III]})$ to estimate the Cl²⁺ abundance.

APPENDIX C: Ni²⁺ ABUNDANCE

The first estimation of the Ni abundance in an H II region was made by Osterbrock et al. (1992) for the Orion Nebula. They used estimates of the atomic data of Ni ions, considering [Ni II] and [Ni III] lines. Since then, the number of Ni abundance determinations in ionized nebulae is still very limited, both for PNe (Zhang & Liu 2006; García-Rojas et al. 2013; Delgado-Inglada et al. 2016) and H II regions (Mesa-Delgado et al. 2009; Delgado-Inglada et al. 2016). There is a considerable amount of [Ni II] and [Ni III] lines in our spectra. However, [Ni II] lines are affected by fluorescence (Lucy 1995) and their use to calculate the abundance of Ni⁺ is restricted to some particular cases as low-excitation nebulae (Zhang & Liu 2006). On the other hand, [Ni III] lines are, in principle, not affected by fluorescence effects and can be used to derive Ni²⁺ abundances. From all the detected [Ni III] lines, we chose [Ni III] $\lambda\lambda 6000, 6534, 6682, 6797, 6946$ and 7890 because they are not affected by blends or telluric absorption.

As we commented in Section 5, all tested diagnostics based on [Ni III] lines fail to provide reliable values of physical conditions, indicating inaccuracies between the observed lines and the theoretical

predictions. [Delgado-Ingla et al. \(2016\)](#) studied the Fe/Ni ratio in eight PNe and three H II regions, including the Orion Nebula. They used different datasets for these last objects, including the high spectral resolution ones from [Esteban et al. \(2004\)](#) and [Mesa-Delgado et al. \(2009\)](#) (which includes HH 202 S), and some previously unpublished observations covering approximately the same area as the Position 1 of [Esteban et al. \(1998\)](#) and the brightest part of the Orion Bar. We have compared our data with some observed flux ratios compiled by [Delgado-Ingla et al. \(2016\)](#) looking for possible undetected line blends or observational inaccuracies. For convenience, we have compared the predicted and observed flux ratios of [Ni III] $\lambda\lambda 6000, 6534$ and 6946 lines that arise from the same atomic level and therefore we expect that their intensity ratios should be constant. In Table D11, we compare the observed flux ratios and the predicted ones using the atomic data of Ni²⁺ by [Bautista \(2001\)](#). As Table D11 shows, the [Ni III] $\lambda 6534/\lambda 6000$ and $\lambda 6946/\lambda 6000$ intensity ratios are not inconsistent with the predicted ones. The most discrepant case is HH 529 II, although it is the component with the greatest dispersion. The intensity ratios based on the data sets with smaller dispersion seems to indicate a systematic value of $\lambda 6534/\lambda 6000 \sim 1.6$ and $\lambda 6534/\lambda 6000 \sim 0.30$ which is compatible with an overestimation of the flux of the [Ni III] $\lambda 6000$ line. However, we discard the presence of sky emission affecting this line. Beside to this, we do not find strong candidates of unusual lines in the literature or in the Atomic Line List v2.05b21 with a wavelength difference below to 0.15 Å (a conservative limit for an appropriate deblending of Gaussian profiles at our spectral resolution). In addition, as can be seen in Table D12, we find an inconsistent pattern of Ni²⁺ abundances in all cuts and components for the six selected lines, with differences up to 0.8 dex. This may be a problem of the currently available atomic data of Ni²⁺, which could not be accurate enough for deriving confident values of its ionic abundances. Therefore, our Ni²⁺/H⁺ abundances must be interpreted with care, since they may include unknown uncertainties.

APPENDIX D: SUPPORTING MATERIAL

In this appendix we include the following material:

- Table D1: Comparison of the Balmer line ratios between [Bla-grave et al. \(2006\)](#) and this work.
- Table D2: Sample of 15 lines of the spectra of cut 2. The complete line list of all cuts is appended in the online supporting material.
- **Table D3** Atomic data set (Transition probabilities and collision strengths) used in this work for the analysis of CELs.
- **Table D4** Effective recombination coefficients used in this work for recombination lines.
- **Table D5** Critical densities of some lines whose ratios are commonly used as density diagnostics.
- **Table D6** Comparison of some observed [Fe III] intensity ratios with the theoretical predictions.
- Table D7: Slopes and intercepts calculated to estimate $T_e(\text{He I})$ using Eq.(4) for a range of usual densities.
- Table D8 and Table D9: Ionic abundances of Fe²⁺/H⁺ derived in all studied components with 11 CELs by using $T_e(\text{low})$ and $T_e(\text{high})$, respectively.
- Table D10: Cl²⁺/H⁺, Cl/H and log(Cl/O) abundances derived with $T_e(\text{low})$, $T_e(\text{[S III]})$ and $T_e(\text{high})$, respectively, for all studied components.
- **Table D11:** Comparison between the predicted and

the measured intensity ratios of Ni²⁺ 2F multiplet ($\lambda\lambda 6000, 6534, 6946$).

- Table D12: Ionic abundances of Ni²⁺/H⁺ derived per line in all studied components.
- **Table D13:** He⁺/H⁺ abundances derived from He I lines highly affected by self-absorption effects.
- **Table D14:** He⁺/H⁺ abundances derived from He I lines not affected by self-absorption effects.
- **Table D15:** O²⁺/H⁺ abundances derived with RLs of several multiplets and transitions.
- **Table D16:** O⁺/H⁺, C²⁺/H⁺ and Ne²⁺/H⁺ abundances derived with RLs.
- Table D17: values of t^2 derived for each component, estimated by using $T_e(\text{He I})$, $T_e(\text{[O III]})$, $T_e(\text{[S III]})$ and $T_e(\text{[N II]})$.
- Table D18: Average radial velocity $\langle V \rangle$ and Full Width at Half Maximum (FWHM) of the lines observed in the nebular component and in HH 529 II-III.
- Fig. D1: Plasma diagnostics used in each analysed component to determine physical conditions based on CEL ratios.
- Fig. D2: Echelle orders extracted using the UVES blue arm with the dichroic #2.
- Fig. D3: Least squares fit of the ghost emission that affects the spectral position $\lambda = 4089.07$.
- Fig. D4: Grotrian diagram of the levels of He I.
- Fig. D5: Dependence of $I(\text{He I } \lambda 7281)/I(\text{He I } \lambda 6678)$ on the physical conditions.
- Fig. D6: Emission spectrum of cut 4 around $\sim \lambda 4089$.

This paper has been typeset from a $\text{\TeX}/\text{\LaTeX}$ file prepared by the author.

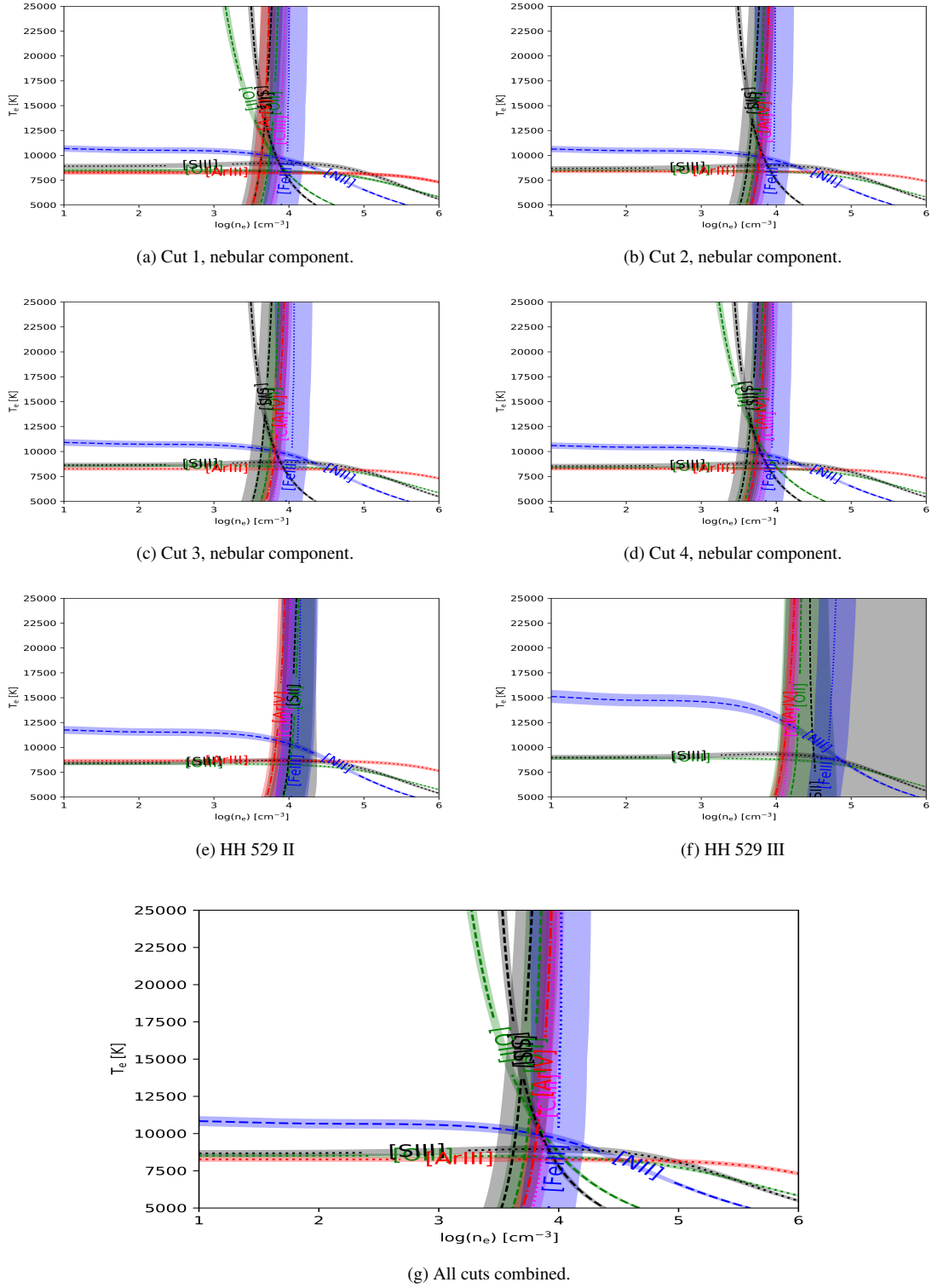


Figure D1. Plasma diagnostic plots for each of the 7 components analysed in this work. The labeled diagnostics correspond to those discussed in Section 5.1, whose results are presented in Table 4.

Table D1. Reddening-corrected Balmer line ratios from Blagrave et al. (2006) and this work.

Ratio	BMB06			This Work		
	High-velocity	Nebular	HH 529 II	HH 529 III	Nebula	Predicted Value
H α /H β	3.65 ± 0.18	3.19 ± 0.03	2.77 ± 0.08	2.87 ± 0.11	2.82 ± 0.09	2.85
H γ /H β	0.74 ± 0.04	0.69 ± 0.01	0.46 ± 0.01	0.46 ± 0.01	0.46 ± 0.01	0.47
H δ /H β	0.34 ± 0.02	0.40 ± 0.01	0.26 ± 0.01	0.26 ± 0.01	0.26 ± 0.01	0.26
H ϵ /H β	0.27 ± 0.02	0.31 ± 0.01	0.16 ± 0.01	0.15 ± 0.01	0.16 ± 0.01	0.16
H γ /H α	0.20 ± 0.01	0.22 ± 0.01	0.17 ± 0.01	0.16 ± 0.01	0.17 ± 0.01	0.17
H δ /H α	0.09 ± 0.01	0.13 ± 0.01	0.09 ± 0.01	0.09 ± 0.01	0.09 ± 0.01	0.09
H ϵ /H α	0.07 ± 0.01	0.10 ± 0.01	0.06 ± 0.01	0.05 ± 0.01	0.06 ± 0.01	0.06

Table D2. Sample of 15 lines of the cut 2 spectra. This cut includes emission from HH 529 II and the Orion Nebula. F(H β)=100.

λ_0 (Å)	Ion	$\lambda(\text{Å})$	v_r km s $^{-1}$	HH 529 II			The Orion Nebula					Notes	
				FWHM km s $^{-1}$	F(λ)/F(H β)	I(λ)/I(H β)	Error (%)	$\lambda(\text{Å})$	v_r km s $^{-1}$	FWHM km s $^{-1}$	F(λ)/F(H β)	I(λ)/I(H β)	
4638.86	O III	4638.40	-29.44	20.68 ± 1.67	0.098	0.098	6	4639.08	14.51	14.86 ± 0.60	0.042	0.045	4
4640.64	N III	4640.07	-36.53	22.68 ± 3.59	0.037	0.040	10	4640.81	11.27	11.95 ± 0.98	0.013	0.014	6
4641.81	O II	4641.35	-29.42	18.60 ± 0.58	0.152	0.164	4	4642.04	15.15	13.76 ± 0.24	0.083	0.089	2
4643.09	N II	4642.64	-28.76	16.21 ± 5.62	0.026	0.028	21	4643.32	15.15	12.01 ± 1.52	0.015	0.016	9
4649.13	O II	4648.67	-29.36	18.90 ± 0.38	0.240	0.258	3	4649.37	15.78	12.51 ± 0.07	0.114	0.122	2
4650.84	O II	4650.38	-29.35	18.89 ± 1.45	0.088	0.095	6	4651.06	14.49	13.28 ± 0.52	0.040	0.043	4
4658.17	[Fe III]	4657.67	-31.86	13.52 ± 0.04	0.887	0.950	2	4658.38	13.83	13.32 ± 0.01	0.770	0.820	2
4661.63	O II	4661.18	-29.26	27.59 ± 1.91	0.124	0.133	6	4661.86	14.47	15.76 ± 0.60	0.048	0.051	4
4667.11	[Fe III]	4666.57	-35.00	19.53 ± 1.62	0.064	0.068	7	4667.28	10.61	18.95 ± 0.59	0.042	0.045	4
4673.73	O II	4673.30	-27.88	29.00 ± 13.54	0.021	0.022	29	4674.00	17.02	11.80 ± 2.54	0.007	0.007	16
4676.23	O II	4675.79	-28.51	19.68 ± 2.89	0.046	0.049	11	4676.47	15.09	13.21 ± 0.69	0.026	0.028	5
4699.22	O II	*	*	*	*	*	*	4699.42	12.50	24.18 ± 9.72	0.011	0.012	33
4701.64	[Fe III]	4701.13	-32.77	12.63 ± 0.25	0.299	0.315	3	4701.85	13.14	13.39 ± 0.05	0.247	0.260	2
4704.55	Ni III?	*	*	*	*	*	*	4704.88	20.78	26.83 ± 3.26	0.014	0.015	9
4705.35	O II	*	*	*	*	*	*	4705.60	15.68	14.40 ± 1.02	0.017	0.018	5

Table D3. Atomic data set used for collisionally excited lines.

Ion	Transition Probabilities	Collision Strengths
O ⁺	Froese Fischer & Tachiev (2004)	Kisielius et al. (2009)
O ²⁺	Wiese et al. (1996), Storey & Zeippen (2000)	Storey et al. (2014)
N ⁺	Froese Fischer & Tachiev (2004)	Tayal (2011)
Ne ²⁺	McLaughlin et al. (2011)	McLaughlin et al. (2011)
S ⁺	Podobedova et al. (2009)	Tayal & Zatsarinny (2010)
S ²⁺	Podobedova et al. (2009)	Grieve et al. (2014)
Cl ⁺	Mendoza & Zeippen (1983)	Tayal (2004)
Cl ²⁺	Fritzsche et al. (1999)	Butler & Zeippen (1989)
Cl ³⁺	Kaufman & Sugar (1986), Mendoza & Zeippen (1982b), Ellis & Martinson (1984)	Galavis et al. (1995)
Ar ²⁺	Mendoza (1983), Kaufman & Sugar (1986)	Galavis, Mendoza & Zeippen (1995)
Ar ³⁺	Mendoza & Zeippen (1982a)	Ramsbottom & Bell (1997)
Fe ²⁺	Quinet (1996), Johansson et al. (2000)	Zhang, Hong Lin (1996)
Fe ³⁺	Froese Fischer et al. (2008)	Zhang & Pradhan (1997)
Ni ²⁺	Bautista (2001)	Bautista (2001)

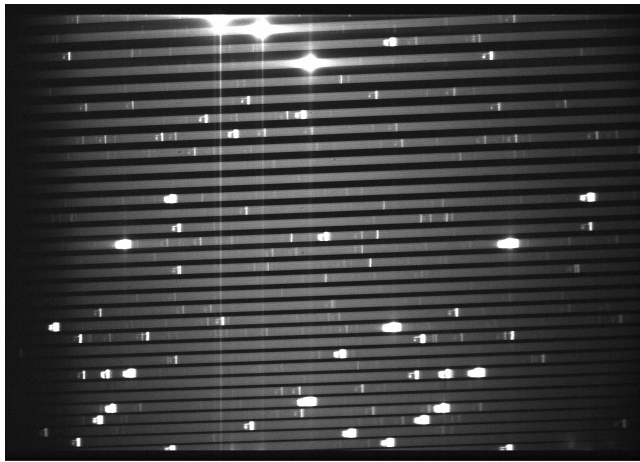


Figure D2. Image of part of the echelle orders extracted in the UVES blue arm using dichroic #2 setting ($\Delta\lambda = 3750 - 4995 \text{ \AA}$). The contrast highlights reflections in the optical system of the spectrograph that can affect some lines. We have established that order 1 is the order at the bottom and 31 at the top.

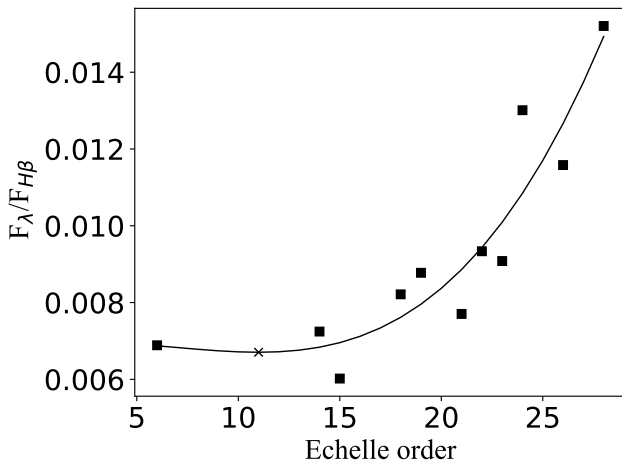


Figure D3. Least Squares fit of the flux emission for the third source of “ghost lines” in the echelle orders. The prediction for the ghost line at $\lambda = 4089.07$ (in the order 11) is marked with a cross.

Table D4. Effective recombination coefficients used for recombination lines.

Ion	Reference
H ⁺	Storey & Hummer (1995)
He ⁺	Porter et al. (2012, 2013)
O ⁺	Pequignot et al. (1991)
O ²⁺	Storey et al. (2017)
C ²⁺	Davey et al. (2000)
Ne ²⁺	Kisielius et al. (1998)

Table D5. Critical densities of density diagnostics for $T_e = 10000 \text{ K}$.

Ion	$\lambda(\text{\AA})$	$n_{\text{crit}} (\text{ cm}^{-3})$
[O II]	3729, 3726	$1.30 \times 10^3, 4.06 \times 10^3$
[S II]	6731, 6716	$3.06 \times 10^3, 1.16 \times 10^3$
[Cl III]	5538, 5518	$3.57 \times 10^4, 7.23 \times 10^3$
[Fe III]	4658, 4702	$5.17 \times 10^6, 3.09 \times 10^6$
[Ar IV]	4740, 4711	$1.26 \times 10^5, 1.39 \times 10^4$

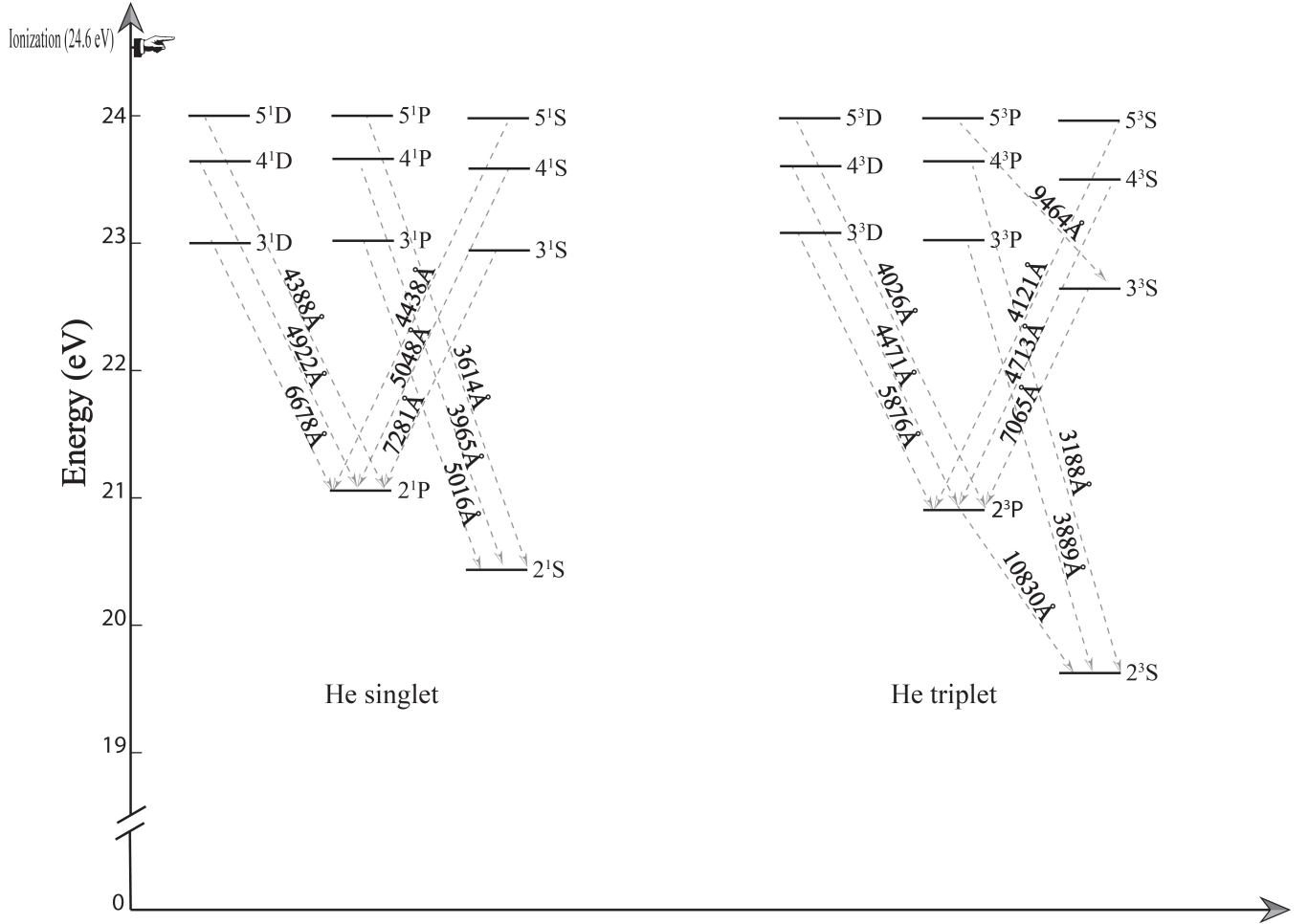
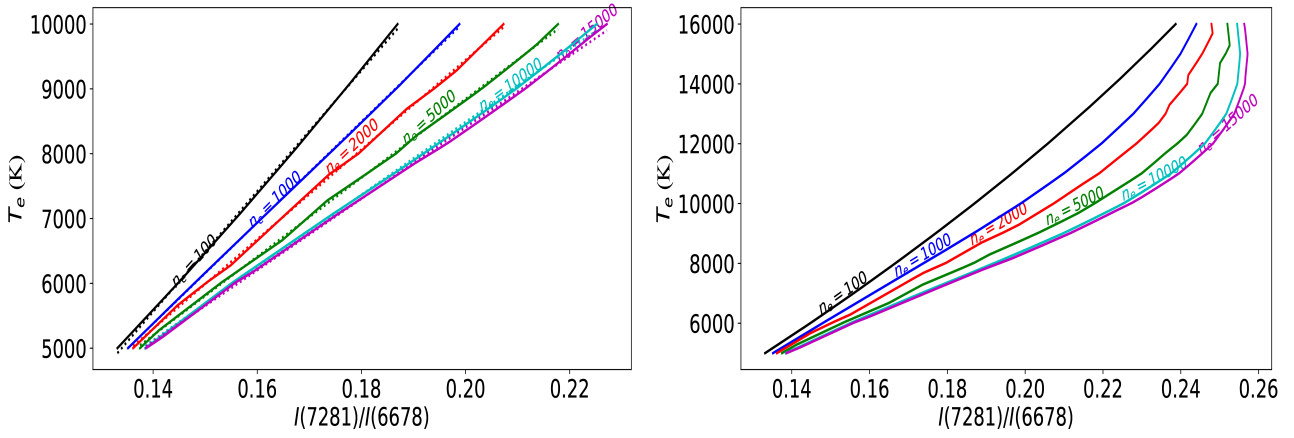


Figure D4. Grotrian diagram of He I for both configurations: triplet and singlet.



(a) A linear fit is accurate for $T_e \leq 10000$ K.

(b) A linear fit is not accurate for $T_e > 10000$ K.

Figure D5. Dependence of $I(\text{He I } \lambda 7281)/I(\text{He I } \lambda 6678)$ on the physical conditions.

Table D6. Comparison of the observed [Fe III] intensity ratios and theoretical ones predicted by the transition probabilities adopted in Table D3

Ratio	Cut 1 Nebula	Cut 2 HH 529 II	Cut 2 Nebula	Cut 3 HH 529 III	Cut 3 Nebula	Cut 4 Nebula	Combined cuts	Prediction
4667/4734*	-	0.52 ± 0.04	0.42 ± 0.02	-	0.45 ± 0.03	0.43 ± 0.03	-	0.28
4778/4734	0.51 ± 0.04	0.70 ± 0.06	0.51 ± 0.03	0.48 ± 0.12	0.44 ± 0.04	0.43 ± 0.03	0.51 ± 0.04	0.48
4778/4667*	-	1.35 ± 0.14	1.22 ± 0.06	-	1.09 ± 0.07	1.00 ± 0.09	-	1.74
4607/4702**	0.24 ± 0.01	0.22 ± 0.02	0.24 ± 0.01	0.24 ± 0.05	0.23 ± 0.02	0.24 ± 0.02	0.23 ± 0.02	0.17
4607/4770**	0.72 ± 0.05	0.60 ± 0.06	0.64 ± 0.03	0.52 ± 0.11	0.64 ± 0.06	0.68 ± 0.05	0.64 ± 0.05	0.51
4702/4770	2.96 ± 0.15	2.68 ± 0.16	2.73 ± 0.10	2.22 ± 0.27	2.74 ± 0.19	2.87 ± 0.14	2.72 ± 0.14	2.93
4658/4755	5.50 ± 0.20	5.28 ± 0.24	5.26 ± 0.15	4.70 ± 0.51	5.32 ± 0.24	5.30 ± 0.19	5.31 ± 0.19	5.49
5011/5085	3.19 ± 0.72	2.51 ± 0.93	5.00 ± 1.00	2.96 ± 1.22	3.61 ± 0.46	3.84 ± 0.94	3.66 ± 0.96	5.94
5271/5412	10.41 ± 1.36	9.39 ± 1.49	10.48 ± 0.81	-	10.37 ± 0.85	9.51 ± 1.24	10.84 ± 1.06	11.01
4881/4987***	4.88 ± 0.31	4.90 ± 0.38	5.07 ± 0.23	2.41 ± 0.46	5.27 ± 0.41	5.98 ± 0.35	4.85 ± 0.37	5.76

* $\lambda 4667$ affected by ghost.** [Fe III] $\lambda 4607.12$ blended with N II $\lambda 4607.15$.*** [Fe III] $\lambda 4987.29$ blended with N II $\lambda 4987.38$.

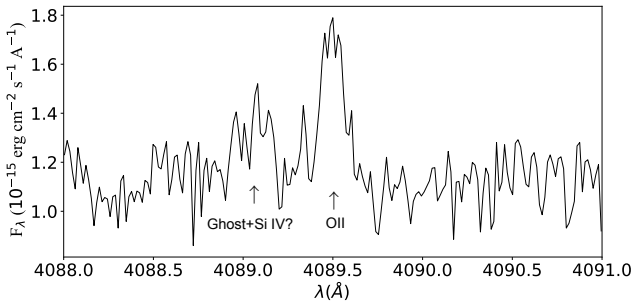


Figure D6. Emission spectrum of the spatial cut 4 around $\lambda 4089.29$. There are no high-velocity components in this spatial cut.

Table D7. Slope and intercept for Eq. 4 for a range of densities.

n_e (cm $^{-3}$)	α	β
100	92984	-7455
500	81830	-6031
1000	77896	-5527
2000	69126	-4378
3000	65040	-3851
4000	62517	-3529
5000	60744	-3305
6000	59402	-3137
7000	58334	-3004
8000	57456	-2895
9000	56715	-2804
10000	56077	-2726
12000	55637	-2676
15000	55087	-2611
20000	54364	-2523
25000	53796	-2452
30000	53329	-2392
40000	52591	-2297
45000	52289	-2257
50000	52019	-2222

Table D8. Fe²⁺/H⁺ abundances based on T_e (low).

λ	Cut 1		Cut 2		Cut 3		Cut 4		Combined cuts
	Nebula	HH 529 II	Nebula	HH 529 III	Nebula	HH 529 III	Nebula	HH 529 III	
4658	5.51 ± 0.02	5.59 ^{+0.08} _{-0.06}	5.56 ^{+0.04} _{-0.03}	5.34 ^{+0.15} _{-0.09}	5.51 ± 0.04	5.47 ^{+0.05} _{-0.04}	5.52 ± 0.03	5.52 ± 0.03	
4702	5.51 ± 0.02	5.59 ^{+0.08} _{-0.06}	5.56 ^{+0.04} _{-0.03}	5.38 ^{+0.15} _{-0.10}	5.52 ± 0.04	5.47 ^{+0.05} _{-0.04}	5.52 ^{+0.04} _{-0.03}	5.52 ^{+0.04} _{-0.03}	
4734	5.48 ± 0.03	5.58 ^{+0.09} _{-0.07}	5.56 ± 0.04	5.36 ^{+0.16} _{-0.16}	5.50 ^{+0.05} _{-0.04}	5.47 ^{+0.05} _{-0.04}	5.52 ± 0.04	5.52 ± 0.04	
4755	5.51 ^{+0.03} _{-0.02}	5.61 ^{+0.09} _{-0.07}	5.58 ^{+0.04} _{-0.03}	5.41 ^{+0.16} _{-0.19}	5.52 ^{+0.05} _{-0.04}	5.49 ^{+0.05} _{-0.04}	5.54 ^{+0.04} _{-0.03}	5.54 ^{+0.04} _{-0.03}	
4770	5.51 ± 0.03	5.63 ^{+0.09} _{-0.07}	5.59 ± 0.04	5.50 ^{+0.15} _{-0.10}	5.55 ^{+0.05} _{-0.04}	5.48 ^{+0.05} _{-0.04}	5.56 ^{+0.04} _{-0.03}	5.56 ^{+0.04} _{-0.03}	
4778	5.51 ± 0.04	5.75 ^{+0.09} _{-0.07}	5.59 ± 0.04	5.36 ^{+0.18} _{-0.12}	5.51 ^{+0.05} _{-0.04}	5.42 ^{+0.06} _{-0.05}	5.55 ± 0.04	5.55 ± 0.04	
4881	5.53 ± 0.02	5.61 ^{+0.09} _{-0.06}	5.58 ^{+0.04} _{-0.03}	5.38 ^{+0.15} _{-0.10}	5.53 ± 0.04	5.49 ^{+0.05} _{-0.04}	5.54 ± 0.03	5.54 ± 0.03	
5011	5.52 ± 0.04	5.78 ^{+0.08} _{-0.07}	5.56 ± 0.04	5.55 ^{+0.15} _{-0.11}	5.51 ^{+0.05} _{-0.04}	5.51 ^{+0.06} _{-0.05}	5.57 ± 0.04	5.57 ± 0.04	
5271	5.55 ± 0.02	5.61 ^{+0.08} _{-0.06}	5.58 ^{+0.04} _{-0.03}	5.40 ^{+0.14} _{-0.09}	5.55 ± 0.04	5.52 ± 0.04	5.55 ± 0.03	5.55 ± 0.03	
5412	5.57 ^{+0.06} _{-0.05}	5.68 ^{+0.10} _{-0.08}	5.60 ^{+0.05} _{-0.04}	-	5.57 ^{+0.05} _{-0.04}	5.58 ^{+0.07} _{-0.06}	5.56 ± 0.05	5.56 ± 0.05	
8838	5.37 ^{+0.11} _{-0.10}	5.41 ^{+0.19} _{-0.15}	5.48 ^{+0.08} _{-0.07}	-	5.34 ^{+0.09} _{-0.08}	5.47 ^{+0.11} _{-0.09}	5.34 ^{+0.09} _{-0.08}	5.34 ^{+0.09} _{-0.08}	
Weighted Average	5.52 ± 0.03	5.62 ± 0.07	5.57 ± 0.02	5.40 ± 0.06	5.52 ± 0.04	5.48 ± 0.03	5.53 ± 0.04	5.53 ± 0.04	

Table D9. Fe²⁺/H⁺ abundances based on T_e (high).

λ	Cut 1		Cut 2		Cut 3		Cut 4		Combined cuts
	Nebula	HH 529 II	Nebula	HH 529 III	Nebula	HH 529 III	Nebula	HH 529 III	
4658	5.77 ^{+0.05} _{-0.04}	5.92 ^{+0.03} _{-0.02}	5.81 ± 0.03	5.72 ± 0.03	5.78 ± 0.03	5.75 ± 0.03	5.79 ± 0.03	5.79 ± 0.03	
4702	5.76 ^{+0.05} _{-0.04}	5.92 ± 0.03	5.80 ± 0.03	5.75 ± 0.04	5.78 ± 0.03	5.74 ± 0.03	5.79 ^{+0.04} _{-0.03}	5.79 ^{+0.04} _{-0.03}	
4734	5.74 ^{+0.05} _{-0.04}	5.91 ^{+0.04} _{-0.03}	5.81 ^{+0.04} _{-0.03}	5.73 ± 0.06	5.77 ^{+0.04} _{-0.03}	5.75 ^{+0.04} _{-0.03}	5.79 ± 0.04	5.79 ± 0.04	
4755	5.76 ^{+0.05} _{-0.04}	5.94 ± 0.03	5.83 ± 0.03	5.79 ± 0.05	5.79 ± 0.03	5.76 ± 0.03	5.81 ± 0.03	5.81 ± 0.03	
4770	5.76 ^{+0.05} _{-0.04}	5.96 ± 0.03	5.84 ± 0.03	5.87 ± 0.05	5.81 ^{+0.04} _{-0.03}	5.75 ^{+0.04} _{-0.03}	5.82 ^{+0.04} _{-0.03}	5.82 ^{+0.04} _{-0.03}	
4778	5.76 ^{+0.06} _{-0.05}	6.08 ± 0.04	5.84 ^{+0.04} _{-0.03}	5.74 ± 0.10	5.78 ^{+0.04} _{-0.03}	5.70 ^{+0.05} _{-0.04}	5.82 ± 0.04	5.82 ± 0.04	
4881	5.79 ± 0.04	5.94 ± 0.03	5.83 ± 0.03	5.76 ± 0.04	5.79 ± 0.03	5.76 ± 0.03	5.80 ± 0.03	5.80 ± 0.03	
5011	5.76 ^{+0.06} _{-0.05}	6.09 ± 0.04	5.79 ± 0.03	5.90 ^{+0.07} _{-0.06}	5.76 ± 0.03	5.77 ^{+0.05} _{-0.04}	5.82 ± 0.04	5.82 ± 0.04	
5271	5.77 ± 0.04	5.91 ± 0.03	5.81 ± 0.03	5.74 ± 0.04	5.79 ± 0.03	5.77 ± 0.03	5.77 ± 0.03	5.79 ± 0.03	
5412	5.80 ^{+0.07} _{-0.06}	5.97 ^{+0.07} _{-0.06}	5.83 ± 0.04	-	5.81 ± 0.04	5.83 ± 0.06	5.80 ± 0.05	5.80 ± 0.05	
8838	5.73 ^{+0.12} _{-0.11}	5.87 ± 0.13	5.83 ^{+0.07} _{-0.06}	-	5.72 ^{+0.08} _{-0.07}	5.86 ± 0.09	5.72 ^{+0.09} _{-0.08}	5.72 ^{+0.09} _{-0.08}	
Weighted Average	5.77 ± 0.02	5.94 ± 0.05	5.82 ± 0.02	5.75 ± 0.05	5.78 ± 0.02	5.76 ± 0.03	5.80 ± 0.02	5.80 ± 0.02	

Table D10. Cl²⁺/H⁺, Cl/H and log(Cl/O) abundances using T_e (low), T_e ([S III]) and T_e (high).

Cut	Component	O ²⁺ /O	Cl ²⁺ /H ⁺	T _e (low)		T _e ([S III])		T _e (high)			
				Cl/H	log(Cl/O)	Cl/H	log(Cl/O)	Cl/H	log(Cl/O)		
1	Nebular	0.73 ± 0.04	4.78 ± 0.02	4.83 ± 0.02	-3.63 ± 0.03	4.88 ^{+0.06} _{-0.05}	4.92 ± 0.06	-3.53 ± 0.07	5.01 ± 0.03	5.04 ± 0.03	-3.42 ± 0.05
2	HH 529 II	0.94 ± 0.04	4.80 ^{+0.08} _{-0.06}	4.83 ± 0.07	-3.74 ± 0.07	5.01 ^{+0.06} _{-0.05}	5.03 ± 0.05	-3.54 ± 0.05	5.08 ± 0.03	5.10 ± 0.03	-3.47 ± 0.04
2	Nebular	0.77 ± 0.05	4.81 ^{+0.04} _{-0.03}	4.86 ± 0.04	-3.61 ± 0.06	4.93 ^{+0.06} _{-0.05}	4.97 ± 0.06	-3.49 ± 0.07	5.03 ± 0.03	5.06 ± 0.03	-3.41 ± 0.05
3	HH 529 III	0.90 ± 0.05	4.777 ^{+0.13} _{-0.09}	4.80 ± 0.12	-3.72 ± 0.13	5.03 ^{+0.08} _{-0.07}	5.05 ± 0.08	-3.48 ± 0.09	5.09 ^{+0.05} _{-0.04}	5.11 ± 0.05	-3.42 ± 0.06
3	Nebular	0.79 ± 0.05	4.80 ^{+0.09} _{-0.03}	4.85 ± 0.04	-3.60 ± 0.06	4.96 ^{+0.06} _{-0.05}	4.99 ± 0.06	-3.46 ± 0.07	5.03 ^{+0.04} _{-0.02}	5.06 ± 0.03	-3.39 ± 0.05
4	Nebular	0.78 ± 0.05	4.79 ± 0.04	4.85 ± 0.04	-3.62 ± 0.06	4.95 ^{+0.06} _{-0.05}	4.99 ± 0.06	-3.48 ± 0.07	5.03 ± 0.03	5.06 ± 0.03	-3.41 ± 0.05
-	Combined cuts	0.81 ± 0.05	4.79 ± 0.03	4.84 ± 0.03	-3.62 ± 0.05	4.94 ^{+0.05} _{-0.04}	4.97 ± 0.05	-3.50 ± 0.06	5.02 ± 0.03	5.05 ± 0.03	-3.41 ± 0.05

Table D11. Comparison of the observed [Ni III] intensity ratios and theoretical ones predicted by the transition probabilities adopted in Table D3

Ratio	Mesa-Delgado et al. (2009)		Delgado-Ingla et al. (2016)		This work		
	Esteban et al. (2004)	HH 202 S	Orion Bar	Nebular	HH 529 II	Prediction	
6534/6000	2.09 ± 0.94	1.58 ± 0.38	1.46 ± 0.40	1.54 ± 0.39	3.35 ± 1.40	2.19	
6946/6000	-	0.28 ± 0.09	-	0.31 ± 0.11	0.82 ± 0.52	0.39	

Table D12. Ni²⁺/H⁺ abundances per line.

λ	Cut 1		Cut 2		Cut 3		Cut 4		Combined cuts
	Nebula	HH 529 II	Nebula	HH 529 III	Nebula	HH 529 III	Nebula	HH 529 III	
6000	4.52 ± 0.08	4.42 ^{+0.13} _{-0.11}	4.34 ^{+0.07} _{-0.06}	-	4.40 ± 0.07	4.42 ^{+0.10} _{-0.09}	4.35 ± 0.08	4.35 ± 0.08	
6534	4.22 ^{+0.10} _{-0.11}	4.61:	4.19 ± 0.06	4.32:	4.16 ± 0.07	4.18 ± 0.11	4.26 ± 0.07	4.26 ± 0.07	
6682	4.76 ^{+0.14} _{-0.13}	-	4.70 ^{+0.14} _{-0.13}	-	4.44 ^{+0.14} _{-0.13}	-	-	-	
6797	4.50 ^{+0.23} _{-0.22}	4.94:	4.79 ± 0.08	-	4.77 ± 0.10	4.81:	4.77 ± 0.14	4.77 ± 0.14	
6946	3.94 ^{+0.26} _{-0.23}	4.75 ^{+0.19} _{-0.17}	4.23 ± 0.11	4.37:	4.21 ± 0.11	4.23 ^{+0.15} _{-0.14}	4.31:	4.31:	
7890	4.42 ± 0.04	4.52 ^{+0.08} _{-0.06}	4.49 ± 0.04	4.28 ^{+0.15} _{-0.11}	4.45 ^{+0.05} _{-0.04}	4.45 ^{+0.05} _{-0.04}	4.46 ± 0.04	4.46 ± 0.04	
Weighted Average	4.37 ± 0.14	4.50 ± 0.08	4.33 ± 0.17	4.28^{+0.15}_{-0.11}	4.32 ± 0.16	4.36 ± 0.12	4.38 ± 0.10	4.38 ± 0.10	

Table D13. He⁺/H⁺ abundances determined using He I triplet lines highly affected by self-absorption. The row of “sum” is the result of adding the measured intensity of the triplets presented and redistributing it assuming negligible self-absorption effects ($\tau = 0$).

λ_0 (Å)	Cut 1		Cut 2		Cut 3		Cut 4	
	Nebula	HH 529 II	Nebula	HH 529 III	Nebula	Nebula	Combined Cuts	
3188	10.67 ± 0.02	10.92 ± 0.02	10.63 ± 0.02	10.97 ± 0.05	10.62 ± 0.02	10.68 ± 0.02	10.71 ± 0.02	
3889	10.60 ± 0.02	10.93 ± 0.02	10.52 ± 0.02	10.75 ± 0.02	10.42 ± 0.02	10.55 ± 0.02	10.61 ± 0.02	
4713	11.01 ± 0.03	11.10 ± 0.03	11.04 ± 0.03	11.02 ^{+0.03} _{-0.04}	11.07 ± 0.02	11.11 ± 0.02	11.07 ± 0.02	
5876	10.96 ± 0.01	10.95 ± 0.01	10.97 ± 0.01	10.92 ± 0.01	10.98 ± 0.01	10.96 ± 0.01	10.97 ± 0.01	
7065	11.34 ± 0.04	11.22 ^{+0.05} _{-0.04}	11.35 ± 0.04	11.18 ± 0.06	11.34 ± 0.04	11.37 ± 0.04	11.34 ± 0.04	
Sum	10.91 ± 0.02	10.97 ± 0.02	10.90 ± 0.02	10.93 ± 0.03	10.89 ± 0.02	10.90 ± 0.02	10.91 ± 0.02	

Table D14. He⁺/H⁺ abundances determined with He I singlet lines and triplet lines less affected by self-absorption effects.

λ_0 (Å)	Cut 1		Cut 2		Cut 3		Cut 4	
	Nebula	HH 529 II	Nebula	HH 529 III	Nebula	Nebula	Combined Cuts	
3614	10.93 ± 0.02	10.85 ± 0.04	10.89 ± 0.02	11.09 ± 0.05	10.86 ± 0.02	10.85 ± 0.02	10.89 ± 0.02	
3965	10.88 ± 0.01	10.86 ± 0.02	10.89 ± 0.01	10.93 ± 0.02	10.87 ± 0.01	10.88 ± 0.01	10.89 ± 0.01	
4026	10.89 ± 0.01	10.97 ± 0.01	10.90 ± 0.01	11.00 ± 0.01	10.93 ± 0.01	10.93 ± 0.01	10.93 ± 0.01	
4388	10.90 ± 0.01	10.96 ± 0.01	10.92 ± 0.01	10.97 ± 0.01	10.91 ± 0.01	10.91 ± 0.01	10.92 ± 0.01	
4438	10.95 ± 0.03	10.88 ± 0.04	10.92 ± 0.02	11.08 ± 0.07	10.92 ± 0.02	10.91 ± 0.03	10.94 ± 0.03	
4471	10.87 ± 0.01	10.96 ± 0.01	10.90 ± 0.01	10.93 ± 0.01	10.91 ± 0.01	10.93 ± 0.01	10.91 ± 0.01	
4922	10.90 ± 0.01	10.94 ± 0.01	10.92 ± 0.01	10.94 ± 0.01	10.92 ± 0.01	10.92 ± 0.01	10.92 ± 0.01	
5016	10.87 ± 0.01	10.78 ± 0.02	10.88 ± 0.01	10.84 ± 0.02	10.88 ± 0.01	10.88 ± 0.01	10.87 ± 0.01	
6678	10.90 ± 0.02	10.94 ± 0.02	10.91 ± 0.01	10.93 ± 0.02	10.92 ± 0.02	10.90 ± 0.01	10.92 ± 0.02	
7281	10.90 ± 0.03	10.95 ± 0.03	10.92 ± 0.03	10.93 ± 0.04	10.92 ± 0.03	10.91 ± 0.03	10.93 ± 0.03	
Average	10.89 ± 0.02	10.95 ± 0.03	10.90 ± 0.01	10.95 ± 0.03	10.90 ± 0.02	10.91 ± 0.02	10.91 ± 0.02	

Table D15: O²⁺ abundances based on RLs.

Mult.	Transition	λ_0	Cut 1	Cut 2	Cut 3	Cut 4
1	$3s^4P - 3p^4D^0$	4638.86	8.547 ± 0.038	8.938 ± 0.027	8.546 ± 0.019	$8.742^{+0.113}_{-0.117}$
	4641.81	$8.433^{+0.017}_{-0.018}$	$8.809^{+0.017}_{-0.018}$	$8.516^{+0.014}_{-0.013}$	$8.824^{+0.014}_{-0.013}$	$8.502^{+0.014}_{-0.013}$
	4649.13	$8.473^{+0.024}_{-0.024}$	8.793 ± 0.014	8.520 ± 0.011	$8.782^{+0.026}_{-0.026}$	8.536 ± 0.015
	4650.84	$8.469^{+0.032}_{-0.031}$	8.912 ± 0.027	8.509 ± 0.019	$9.016^{+0.074}_{-0.074}$	8.521 ± 0.023
	4661.63	$8.534:$	$9.021^{+0.027}_{-0.026}$	$8.550:$	$8.974^{+0.032}_{-0.032}$	$8.602:$
	4673.73	$8.579^{+0.152}_{-0.149}$	9.041 ± 0.120	$8.478^{+0.070}_{-0.069}$	$8.960:$	$8.609:$
	4676.23	$8.400^{+0.052}_{-0.053}$	$8.748^{+0.047}_{-0.049}$	8.475 ± 0.022	$8.926^{+0.068}_{-0.069}$	8.497 ± 0.026
Average	8.465 ± 0.043	8.830 ± 0.073	8.515 ± 0.018	8.843 ± 0.085	8.517 ± 0.033	8.525 ± 0.026
2	$3s^4P - 3p^4P^0$	4317.14	$8.498^{+0.052}_{-0.054}$	$9.099^{+0.030}_{-0.031}$	8.671 ± 0.022	$8.644^{+0.047}_{-0.048}$
	4345.56	8.582 ± 0.057	$9.194^{+0.035}_{-0.035}$	8.714 ± 0.026	$9.139^{+0.072}_{-0.072}$	8.656 ± 0.035
	4349.43	8.659 ± 0.040	$9.015^{+0.024}_{-0.024}$	8.678 ± 0.013	$8.996^{+0.021}_{-0.021}$	8.726 ± 0.030
	4366.89	$8.631^{+0.041}_{-0.040}$	$9.237^{+0.026}_{-0.025}$	8.710 ± 0.022	$9.210^{+0.052}_{-0.052}$	$8.715^{+0.026}_{-0.025}$
Average	8.595 ± 0.040	9.085 ± 0.091	8.686 ± 0.016	9.074 ± 0.097	$8.672^{+0.031}_{-0.031}$	8.767 ± 0.030
5	$3s^2P - 3p^2D^0$	4414.90	$8.807^{+0.053}_{-0.051}$	$8.939^{+0.046}_{-0.047}$	8.754 ± 0.025	$8.772^{+0.026}_{-0.027}$
	4416.97	$8.622^{+0.069}_{-0.063}$	-	$8.769^{+0.031}_{-0.030}$	-	8.734 ± 0.039
Average	8.710 ± 0.093	$8.939^{+0.046}_{-0.047}$	8.760 ± 0.007	-	8.759 ± 0.018	8.702 ± 0.011
10	$3p^4D^0 - 3d^4F$	4069.62	$8.459^{+0.064}_{-0.060}$	-	$8.246:$	$8.352:$
	4069.88	$8.352^{+0.050}_{-0.049}$	$8.431:$	$8.297:$	$8.341:$	$8.386:$
	4072.15	8.449 ± 0.026	$8.608^{+0.035}_{-0.034}$	$8.421^{+0.017}_{-0.018}$	8.758 ± 0.064	$8.423^{+0.021}_{-0.022}$
Average	$8.436:$	$8.757:$	-	-	-	$8.407^{+0.026}_{-0.026}$
	4078.84	$8.299^{+0.166}_{-0.159}$	$8.998^{+0.093}_{-0.092}$	$8.503^{+0.040}_{-0.039}$	$8.385:$	$8.787:$
	4085.11	8.212 ± 0.150	$9.385:$	8.509 ± 0.035	$9.385:$	8.408 ± 0.065
	4092.93	-	$8.550:$	$8.598^{+0.049}_{-0.047}$	$8.553:$	$8.453^{+0.073}_{-0.071}$
Average	8.421 ± 0.048	8.6223 ± 0.093	8.450 ± 0.052	8.758 ± 0.064	8.423 ± 0.009	8.413 ± 0.099
15	$3s^2D - 3p^2F^0$	4590.97	$8.414^{+0.062}_{-0.060}$	$8.595^{+0.062}_{-0.061}$	$8.385^{+0.034}_{-0.033}$	$8.681^{+0.073}_{-0.072}$
19	$3p^4P^0 - 3d^4P$	4121.46	$8.791:$	-	8.865 ± 0.030	$8.806:$
Average	$8.451^{+0.069}_{-0.069}$	9.029 ± 0.056	$8.565^{+0.027}_{-0.026}$	$9.023^{+0.154}_{-0.158}$	8.512 ± 0.035	8.579 ± 0.044
	4132.80	$8.622^{+0.038}_{-0.037}$	9.059 ± 0.031	8.605 ± 0.019	$8.976^{+0.023}_{-0.023}$	$8.603^{+0.023}_{-0.024}$
	4153.30	8.616 ± 0.013	8.616 ± 0.093	8.812 ± 0.153	8.568 ± 0.044	8.603 ± 0.022
Average	8.565 ± 0.079	9.051 ± 0.013	$8.363^{+0.126}_{-0.123}$	-	$8.458^{+0.102}_{-0.098}$	8.494 ± 0.097
20	$3p^4P^0 - 3d^4D$	4104.99	-	$8.761:$	$8.761:$	$8.766:$
	4110.79	$8.811:$	$9.584:$	$8.805:$	$9.167:$	$8.766:$
	4119.22	$8.563^{+0.049}_{-0.048}$	$8.842^{+0.061}_{-0.061}$	$8.626^{+0.023}_{-0.022}$	-	$8.475^{+0.072}_{-0.074}$
Average	$8.563^{+0.049}_{-0.048}$	$8.842^{+0.061}_{-0.061}$	8.626 ± 0.087	$9.167:$	8.469 ± 0.008	8.674 ± 0.087
36	$3p^2F^0 - 3d^2G$	4185.44	$8.095^{+0.062}_{-0.062}$	8.034 ± 0.112	$7.971^{+0.045}_{-0.045}$	$8.425:$
	4189.79	$8.344^{+0.044}_{-0.044}$	8.638 ± 0.048	$8.307^{+0.033}_{-0.029}$	8.808 ± 0.120	$8.329^{+0.096}_{-0.096}$
Average	8.200 ± 0.128	8.279 ± 0.323	8.107 ± 0.172	8.808 ± 0.120	8.146 ± 0.119	8.217 ± 0.138
3d-4f	$3d^4F - 4fG^2 [3]^0$	4087.15	8.588 ± 0.092	$8.868^{+0.117}_{-0.119}$	$8.644^{+0.065}_{-0.065}$	8.142 ± 0.099
	4089.29	$8.451^{+0.058}_{-0.057}$	$8.939:$	$8.518^{+0.062}_{-0.062}$	$8.752:$	$8.422^{+0.056}_{-0.056}$
	4095.64	-	8.824 ± 0.100	$8.499^{+0.054}_{-0.053}$	$9.385:$	$8.545:$
	4097.26	$8.547^{+0.059}_{-0.059}$	-	$8.551^{+0.053}_{-0.053}$	-	8.577 ± 0.031
	4275.55	$8.464^{+0.056}_{-0.056}$	$8.680^{+0.106}_{-0.110}$	$8.520^{+0.046}_{-0.047}$	-	$8.475^{+0.053}_{-0.052}$
Average	8.494 ± 0.052	8.767 ± 0.082	8.534 ± 0.032	9.142 ± 0.099	8.468 ± 0.067	8.507 ± 0.081
Mult. 1, 2, 10, 20 and 3d-4f transitions	Average	8.465 ± 0.072	8.838 ± 0.143	8.539 ± 0.084	8.857 ± 0.115	8.512 ± 0.075
						8.523 ± 0.108

Table D16. O⁺, C²⁺ and Ne²⁺ abundances based on RLs.

Mult.	Transition	λ_0	Cut 1 Nebula	Cut 1 HH 529 II	Cut 2 Nebula	Cut 2 HH 529 III	Cut 3 Nebula	Cut 4 Nebula	Combined Cuts
O⁺									
1	3s ⁵ S ⁰ -3p ⁵ P	7771.94 7774.17 7775.39	8.344 ± 0.100	<7.91	8.250 ± 0.064	<7.95	8.275 ± 0.073	8.274 ^{+0.068} _{-0.069}	8.187 ± 0.073
C²⁺									
6	3d ² D-4f ² F ⁰	4267.00 4267.18 4267.26	8.349 ^{+0.030} _{-0.031}	8.457 ± 0.017	8.347 ± 0.017	8.557 ± 0.026	8.339 ± 0.013	8.328 ^{+0.021} _{-0.022}	8.371 ± 0.026
16.04	4d ² D-6f ² F ⁰	6151.27 6151.53	-	9.054:	8.376:	-	8.441 ± 0.120	-	-
17.02	4f ² F ⁰ -5g ² G	9903.46 9903.89	8.326 ^{+0.043} _{-0.045}	8.465 ^{+0.066} _{-0.063}	8.363 ± 0.035	8.622 ^{+0.138} _{-0.136}	8.301 ^{+0.057} _{-0.056}	8.353 ^{+0.043} _{-0.042}	8.377 ^{+0.057} _{-0.056}
17.04	4f ² F ⁰ -6g ² G	6461.95 6462.13	8.354 ± 0.091	8.704:	8.298 ± 0.065	-	8.318 ± 0.060	8.351 ± 0.071	8.353 ^{+0.118} _{-0.116}
17.06	4f ² F ⁰ -7g ² G	5342.38 5342.50	8.619:	-	8.449 ^{+0.059} _{-0.060}	-	8.502 ^{+0.064} _{-0.065}	-	-
	Adopted	8.342 ± 0.030	8.458 ± 0.021	8.351 ± 0.025	8.560 ± 0.026	8.340 ± 0.029	8.334 ± 0.022	8.371 ± 0.026	
Ne²⁺									
1	3s ⁴ P-3p ⁴ P ⁰	3694.21 3766.26	-	8.643 ^{+0.072} _{-0.073}	8.095 ^{+0.063} _{-0.065}	-	8.315:	-	-
	Adopted	-	8.603 ± 0.057	8.072 ± 0.029	-	8.036 ± 0.150	-	-	-

Table D17. Values of t^2 estimated for each component, based on the combination of Eq. (12) with Eq. (13), Eq. (14) and Eq. (15).

Cut	Component	$t^2(O^{2+})$	$t^2(S^{2+})$	$t^2(N^+)$
1	Nebular	0.004 ± 0.012	0.040 ± 0.026	0.053 ± 0.018
2	HH 529 II	0.025 ± 0.013	0.062 ± 0.026	0.095 ± 0.024
2	Nebular	0.008 ± 0.012	0.039 ± 0.025	0.058 ± 0.018
3	HH 529 III	0.030 ± 0.017	0.072 ± 0.034	0.120 ± 0.038
3	Nebular	0.010 ± 0.013	0.036 ± 0.026	0.064 ± 0.019
4	Nebular	0.022 ± 0.014	0.062 ± 0.027	0.079 ± 0.020

Table D18. Average velocities and FWHM for the observed ions in each component. The number of lines used in the average are shown in parentheses.

Ion	I.P. (eV)	Nebular Cut 2		HH 529 II		HH 529 III	
		$\langle V \rangle$ (Km s $^{-1}$)	$\langle \text{FWHM} \rangle$ (Km s $^{-1}$)	$\langle V \rangle$ (Km s $^{-1}$)	$\langle \text{FWHM} \rangle$ (Km s $^{-1}$)	$\langle V \rangle$ (Km s $^{-1}$)	$\langle \text{FWHM} \rangle$ (Km s $^{-1}$)
[O I]	0.00	28.80 ± 0.03 (2)	11.80 ± 0.02 (2)	-	-	-	-
[C I]	0.00	28.70 ± 0.03 (3)	9.49 ± 0.10 (3)	-	-	-	-
[N I]	0.00	30.25 ± 0.64 (3)	9.51 ± 0.60 (3)	-	-	-	-
[Cr II]	6.77	28.28 ± 2.66 (5)	9.71 ± 1.19 (5)	-26.50 ± 1.00 (1)	25.60 ± 1.00 (1)	-27.20 ± 1.00 (1)	39.40 ± 1.00 (1)
[Ni II]	7.64	30.20 ± 0.08 (10)	11.75 ± 0.63 (10)	-30.20 ± 6.09 (3)	15.81 ± 2.83 (3)	-	-
[Fe II]	7.90	27.33 ± 1.36 (34)	11.84 ± 2.29 (34)	-28.76 ± 1.21 (2)	13.66 ± 0.97 (2)	-	-
[S II]	10.36	23.10 ± 0.86 (4)	21.52 ± 0.90 (4)	-27.80 ± 0.03 (4)	16.29 ± 0.45 (4)	-21.94 ± 1.46 (6)	22.92 ± 1.00 (6)
[Cl II]	12.97	24.80 ± 1.00 (1)	20.40 ± 1.00 (1)	-23.80 ± 1.00 (1)	18.90 ± 1.00 (1)	-	-
H I	13.60	16.39 ± 0.78 (51)	24.95 ± 0.16 (51)	-29.08 ± 0.36 (51)	27.20 ± 0.01 (51)	-23.90 ± 0.89 (45)	33.12 ± 0.44 (45)
[O II]	13.62	17.85 ± 1.65 (2)	18.69 ± 0.69 (2)	-28.40 ± 1.20 (2)	20.04 ± 1.10 (2)	-21.60 ± 0.03 (2)	25.27 ± 0.53 (2)
O I	13.62	18.73 ± 0.50 (3)	23.29 ± 0.86 (3)	-	-	-	-
[N II]	14.53	20.67 ± 0.95 (4)	19.45 ± 0.05 (4)	-28.70 ± 0.80 (4)	18.13 ± 0.45 (4)	-19.75 ± 1.05 (3)	25.98 ± 0.19 (3)
[Fe III]	16.19	13.83 ± 1.09 (21)	12.10 ± 0.32 (21)	-31.90 ± 0.02 (17)	13.56 ± 0.34 (17)	-26.43 ± 1.07 (13)	25.11 ± 2.47 (13)
[Cr III]	16.49	12.40 ± 2.02 (4)	16.98 ± 4.86 (4)	-34.54 ± 1.56 (3)	20.24 ± 1.56 (3)	-23.60 ± 1.00 (1)	10.80 ± 1.00 (1)
[Ni III]	18.17	20.28 ± 0.15 (2)	15.36 ± 0.87 (2)	-24.54 ± 0.24 (2)	12.80 ± 1.57 (2)	-19.20 ± 1.00 (1)	25.70 ± 1.00 (1)
[S III]	23.34	15.00 ± 1.00 (1)	12.70 ± 1.00 (1)	-30.60 ± 1.00 (1)	15.10 ± 1.00 (1)	-25.90 ± 1.00 (1)	25.10 ± 1.00 (1)
[Cl III]	23.81	14.20 ± 0.30 (4)	12.44 ± 0.29 (4)	-30.98 ± 1.91 (3)	16.16 ± 1.06 (3)	-27.24 ± 0.08 (2)	25.81 ± 1.08 (2)
C II	24.38	18.63 ± 1.95 (6)	13.71 ± 0.69 (6)	-26.00 ± 2.18 (5)	21.61 ± 1.82 (5)	-23.39 ± 1.93 (2)	46.05 ± 4.30 (2)
He I	24.59	15.87 ± 0.53 (75)	15.81 ± 0.33 (75)	-29.08 ± 0.90 (66)	21.52 ± 1.23 (66)	-24.42 ± 0.60 (42)	26.51 ± 0.63 (42)
[Ar III]	27.63	15.40 ± 0.04 (2)	11.10 ± 0.04 (2)	-30.40 ± 0.04 (2)	16.10 ± 0.04 (2)	-25.00 ± 1.00 (1)	25.10 ± 1.00 (1)
[Fe IV]	30.65	21.20 ± 1.00 (1)	12.30 ± 1.00 (1)	-23.70 ± 1.00 (1)	19.40 ± 1.00 (1)	-	-
[Cr IV]	30.96	18.40 ± 1.00 (1)	12.10 ± 1.00 (1)	-25.70 ± 1.00 (1)	21.90 ± 1.00 (1)	-30.20 ± 1.00 (1)	39.40 ± 1.00 (1)
[O III]	35.12	16.13 ± 1.37 (3)	11.75 ± 0.45 (3)	-29.07 ± 1.03 (3)	17.60 ± 0.01 (3)	-25.03 ± 0.42 (3)	25.02 ± 0.70 (3)
O II	35.12	15.80 ± 0.03 (6)	12.64 ± 0.44 (6)	-29.38 ± 0.12 (6)	18.89 ± 0.43 (6)	-25.23 ± 0.68 (6)	31.78 ± 3.46 (6)
[Cl IV]	39.61	17.80 ± 1.00 (1)	10.50 ± 1.00 (1)	-27.60 ± 1.00 (1)	21.90 ± 1.00 (1)	-20.50 ± 1.00 (1)	33.10 ± 1.00 (1)
[Ar IV]	40.74	15.35 ± 1.55 (2)	11.69 ± 0.69 (2)	-29.45 ± 2.65 (2)	21.20 ± 2.20 (2)	-26.83 ± 0.07 (2)	27.88 ± 2.92 (2)
[Ne III]	40.96	15.80 ± 0.10 (2)	12.35 ± 0.05 (2)	-28.95 ± 0.05 (2)	16.22 ± 0.04 (2)	-25.90 ± 0.03 (2)	25.50 ± 0.03 (2)
Ne II	40.96	14.92 ± 0.33 (2)	14.44 ± 1.49 (2)	-26.89 ± 0.37 (2)	22.28 ± 0.14 (2)	-	-
N I	14.53	29.82 ± 0.25 (16)	9.47 ± 0.20 (16)	-29.80 ± 1.00 (1)	36.00 ± 1.00 (1)	-25.40 ± 1.00 (1)	29.40 ± 1.00 (1)
Si II	16.35	19.25 ± 2.45 (10)	19.42 ± 1.35 (10)	-29.18 ± 1.06 (8)	17.35 ± 1.78 (8)	-26.90 ± 1.16 (7)	23.89 ± 2.25 (7)
Si III	33.49	12.91 ± 1.00 (1)	13.23 ± 2.79 (1)	-31.80 ± 1.00 (1)	10.80 ± 1.00 (1)	-	-
Ne I	21.57	16.66 ± 2.38 (6)	15.66 ± 0.65 (6)	-31.78 ± 5.50 (3)	23.81 ± 2.20 (3)	-	-
S II	23.34	16.50 ± 0.69 (5)	16.69 ± 4.21 (5)	-26.88 ± 0.44 (3)	25.49 ± 3.34 (3)	-34.90 ± 1.00 (1)	33.10 ± 1.00 (1)
N II	29.60	15.07 ± 2.57 (25)	13.65 ± 1.94 (25)	-29.93 ± 1.10 (10)	18.33 ± 2.29 (10)	-25.31 ± 3.86 (7)	24.49 ± 7.94 (7)
S III	34.79	16.06 ± 0.80 (4)	13.83 ± 2.61 (4)	-29.04 ± 1.87 (4)	25.21 ± 3.48 (4)	-38.86 ± 4.34 (3)	15.85 ± 4.12 (3)
N III	47.45	11.52 ± 0.81 (2)	11.94 ± 0.16 (2)	-36.50 ± 1.00 (1)	22.70 ± 1.00 (1)	-	-